Leading to the world of tomorrow

KIST Today

December 2016

Vol. 9 No. 2
ISSN 2005-9043

Technical Reviews

Bio / Medical

Insights on Stem Cell Preconditioning and Instructive Biomaterials to Enhance Cell Adhesion, Retention, and Engraftment for Tissue Repair

Materials / Systems

Direct Electron Transfer of Enzymes in a Biologically Assembled Conductive Nanomesh Enzyme Platform

Energy / Environment

High-Performance Thermoelectric Paper Based on Double Carrier-Filtering Processes at Nanowire Heterojunctions

Korea Institute of Science and Technology

Contents

Foreword

2016 was a year of exciting scientific discoveries, such as gravity waves that verify Einstein's theories, advancements in artificial intelligence (AI), augmented reality, and CRISPR technology for genome editing. Perhaps most newsworthy, however, was the outcome of the Go competition between the most talented master of the game, Se Dol LEE, and Google DeepMind's artificial intelligence program, AlphaGo. AlphaGo's victory in four out of five Go matches added to public fears that AI represents a threat to humanity, a scenario portrayed effectively in the *Terminator* movies. While many of the concerns related to AI are generated from a lack of understanding of the technology, it is important to consider all the aspects and implications of the developing field. Here at KIST we are thoroughly committed to moving ahead in AI research in a responsible manner.

According to Dr. Dong Jin KIM, Director of KIST's Brain Science Institute, there are currently two main avenues of brain science research: treating cerebropathia and developing AI. Advanced countries have long been accelerating their research in this field. In 2013, the U.S. launched a program entitled "Brain Research through Advancing Innovative Neurotechnologies" around the same time that the EU began its "Human Brain Project." In 2015, China launched its own brain project, and South Korea is now making its own investments in brain science, especially AI, in hopes of becoming a leader in the field.

It is important to note that the development of AI requires collaboration on a massive scale. Each of KIST's seven core areas of strategic research: materials, information, robotics, agriculture, carbon, life, and the environment will need to work together in generating important breakthroughs and developing commercially viable products.

As always, we depend on you—our friends and supporters—to help us succeed in our endeavors.

Dr. Byung Gwon LEE
President of KIST

Technical Review

Insights on Stem Cell Preconditioning and Instructive Biomaterials to Enhance Cell Adhesion, Retention, and Engraftment for Tissue Repair

Soo Hyun KIM
Center for Biomaterials, Biomedical Research Institute
soohkim@kist.re.kr

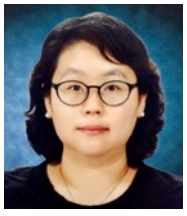

Young Mee JUNG
Center for Biomaterials, Biomedical Research Institute
ymjeong@kist.re.kr

Muhammad SHAFIQ
Center for Biomaterials, Biomedical Research Institute, KIST
m.shafiq44@gmail.com

Introduction

Cell-based therapies are showing considerable promise in the search to find cures for various types of tissue damage. These therapies, which employ a variety of cell populations including stem cells, embryonic stem cells (ESCs), and induced pluripotent stem cells (iPSCs), have been particularly beneficial in applications associated with regenerative medicine and tissue engineering (TE) [1, 2]. Cells are transplanted into the body in different ways and participate in the repair of damaged tissues either directly or via paracrine mechanisms (Figure 1) [3, 4]. However, the success of cell therapy has been limited due to marginal cell survival and retention after transplantation as well as limited engraftment (typically < 3% cells engraft) in hostile ischemic environments [5]. Therefore, the latest strategies are focusing on making cells less vulnerable to these effects, thereby improving the efficacy of cell therapy.

Enhancing transplantation outcomes by creating a permissive microenvironment

To enhance stem cell survival and retention after transplantation, two approaches are generally adopted: 1) manipulation of cells before transplantation and 2) the development of suitable biomaterials to enhance

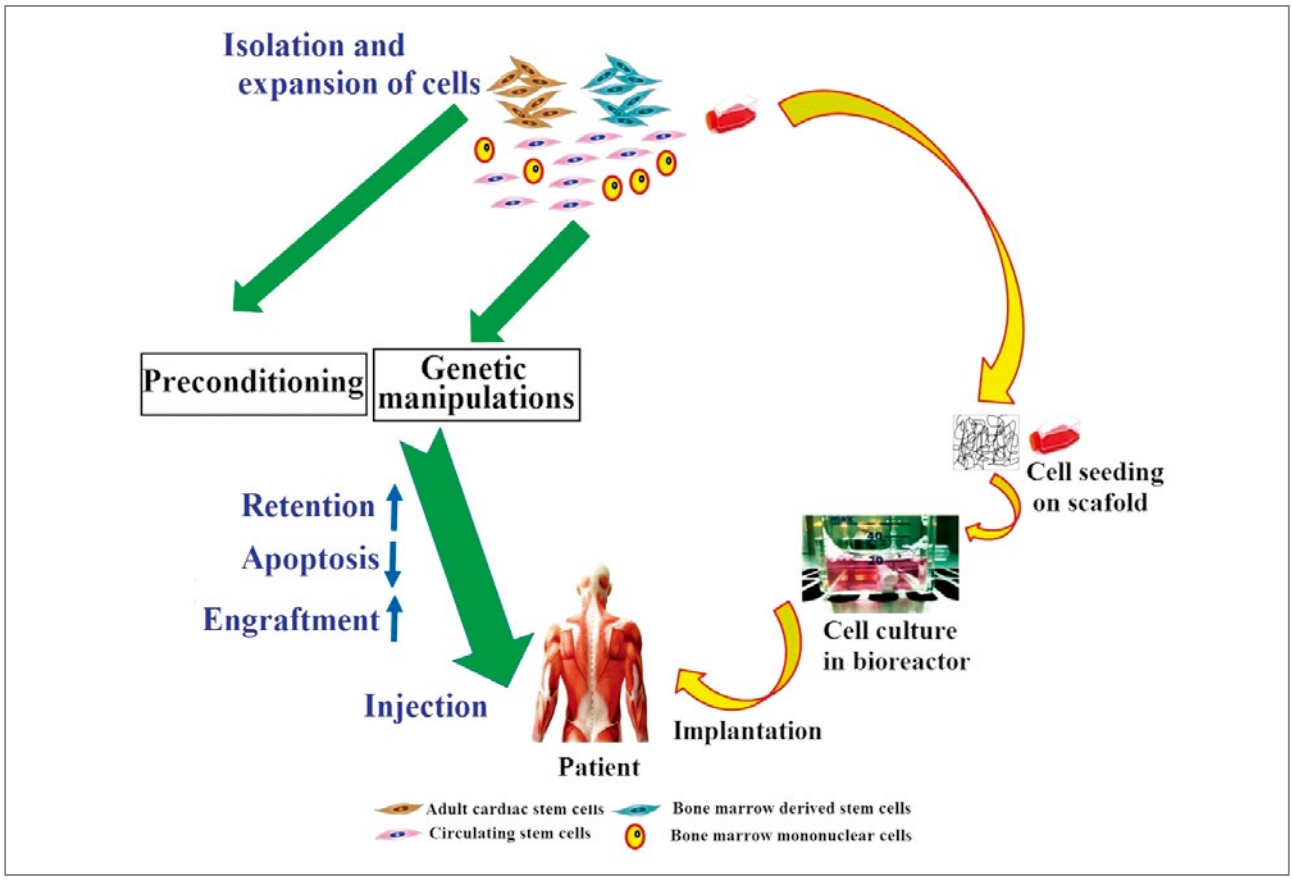

Figure 1. Schematic representation of approaches used for stem cell therapy for tissue engineering applications. Cells are isolated and expanded *in vitro* before implantation. In the first approach, untreated, preconditioned, or genetically manipulated cells are delivered into implantation site. Preconditioning or genetic manipulations reduce apoptosis and enhance the engraftment of transplanted cells. In the second strategy, cells are seeded on biodegradable scaffold, grown *in vitro* in bioreactor, and then transplanted into implantation site. Scaffolds can be functionalized with bioactive molecules, such as adhesive cues or differentiation cues.

cell adhesion, retention, and differentiation. Moreover, the delivery of differentiation and maturation signals along with stem cell transplantation may enhance cell therapy. In this article, we provide insight on how instructive biomaterials enhance stem cell function for effective tissue repair and discuss methods to enhance survival, retention, and engraftment of stem cells.

Strategies to enhance stem cell survival after transplantation

In cell therapy, two types of approaches are used before transplantation. Cells are isolated and processed *in vitro* using minimal or extensive manipulations and subsequently transplanted back into the patient's heart or brain to accelerate healing. There are various strategies currently available for *in vitro* stem cell manipulation or modification, including physical or chemical manipulation, expansion and culture under prescribed conditions, genetic manipulation, and differentiation before transplantation (Figure 2) [6]. With the correct combination of techniques, stem cell use may be optimized to reduce infarct scarring, promote cell growth and healing, and augment angiogenesis and neovascularization to improve functional outcomes.

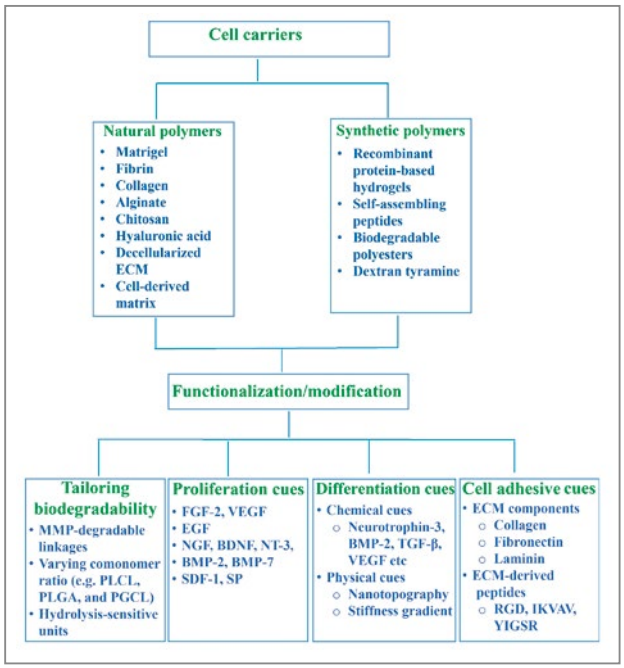

Figure 2. Many cell types have been proposed for stem cell therapy. Stem cells or progenitor cells can be isolated from bone marrow, myocardium, circulation, adipose tissues, or brain. Moreover, adult cells can be reprogrammed to induced pluripotent stem cells and used for cell therapy applications. These cell types can be either injected into the defective tissue or placed in circulation without manipulation. Alternatively, cells can be preconditioned with prescribed medium or can be genetically manipulated. Preconditioning or genetic manipulation may enhance retention at the target site and/or augment cell engraftment.

Readers are referred to a comprehensive review regarding stem cell preconditioning and genetic manipulation for effective tissue repair in reference [7].

Use of biomaterials to enhance stem cell retention after transplantation

To date, different types of cell carriers have been designed for cell transplantation. These include injectable hydrogels, macro-sized constructs, microcarriers, and microspheres (Figure 3) [8]. Injectable hydrogels and microspheres are excellent cell delivery methods because they are easily introduced into the body and localize to the desired site, which is not the case with a cell suspension (Figure 3, Tables 1–3). A variety of naturally-derived ECM molecules (e.g., collagen, laminin, and fibronectin) are currently being used as cell vehicles due to their intrinsic cell-binding capabilities and their ability to manipulate the fate of transplanted cells over both short and long time frames [9, 10]. In addition, suitable biological cues have been identified and employed to fabricate molecularly designed biomaterials that can deliver neurotrophic factors and growth factors, control the microenvironment of transplanted cells, instruct the fate of transplanted cells, and control the host response [8, 11]. In this section, we review biomaterials used to enhance cell survival and retention for tissue regeneration applications.

Natural biomaterials as cell vehicles

Naturally-derived biomaterials are conducive to *in vivo* microenvironments and are abundant. Various natural biomaterials such as collagen, fibrin, alginate, and chitosan have been investigated as cell carriers.

Matrigel has been used to enhance cell survival and retention in damaged tissues. Matrigel enhanced the survival of neural progenitor cells and reduced infarct size in a middle cerebral artery occlusion (MCAO) model in rats [12]. Matrigel has also been shown to enhance cardiac function and the retention of ESCs when injected after MI [13]. However, Matrigel has several limitations which impede its commercialization for cell therapy.

Fibrin matrix has also been frequently used as a cell carrier in various injured tissues. Xiong et al. [14] showed that fibrin patches enhanced the survival and engraftment of human ESC-derived ECs and SMCs. Habib et al. developed an *in situ* polymerizable PEGylated fibrinogen (PF) matrix to enhance the survival and retention of neonatal rat CMCs (NRVCMs) or human ESC-derived CMCs (hESC-CMs) for the treatment of infarcted rat

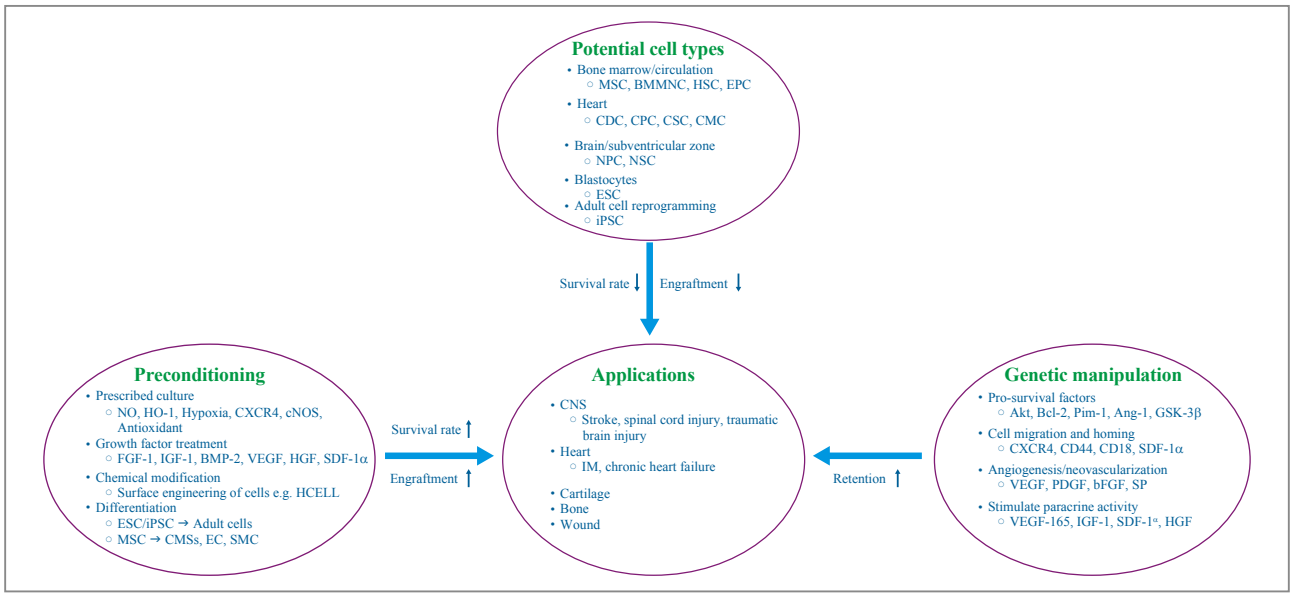

Figure 3. Biomaterials used to enhance stem cell survival and engraftment. Biomaterials may serve as templates to guide tissue formation and can be designed to degrade *in vivo*. Both natural and synthetic biomaterials can be used as cell vehicles. In addition, biomaterials can be functionalized with different moieties to tailor degradability, enhance cell adhesion, or stimulate tissue specific lineages of cells. These cell vehicles can be fabricated into different shapes using a variety of processing techniques, such as 3D printing, electrospinning, extrusion, or molding.

Table 1. Natural polymeric biomaterials as cell carriers for enhancement of cell retention and engraftment for *in vivo* tissue regeneration.

Injury	Cell Type	Biomaterial	Stem cell Survival	Functional improvement	Ref
SCI	BMSCs	Fibrin	Cell survival ↑	Functional improvement ↑	[16]
Stroke	NPCs	HA–Hep–Col	Cell survival ↑ in hydrogel group	Inflammatory response ↓	[24]
MI	ECs, SMCs	Fibrin	Cell survival ↑ in fibrin group	Engraftment ↑ cardiac function ↑	[14]
MI	CMC, ESC	PEG-FN	Cell engraftment ↑	Survival rate ↑ cardiac function ↑	[15]
MI	ADSCs	Chitosan	Cell retention ↑ at 4 weeks	Engraftment ↑ CMCs ↑ADSCs ↑	[20]
MI	CDCs	Collagen + HA	Cell retention ↑in hydrogel group	ECs and CMCs formed	[23]
SC	GFP-MSCs	Supramolecular HA hydrogels	Cells survived for up to 60 days after SC implantation	N.R.	[25]
SC, HI	CPCs	HA hydrogel	Cell survival ↑	Neovascularization ↑, Anastomosis, transplanted cells differentiated into ECs	[22]

Abbreviations: N.R., not reported; MI, myocardial infarction; HA, hyaluronan; Hep, heparin; IM, infracted myocardium; SCI, spinal cord injury; TBI, traumatic brain injury; CCI, cortical impact injury; NPCs, neural progenitor cells; BMSCs, bone marrow mesenchymal stem cells; hMSCs, human mesenchymal stem cells; NSCs, neural stem cells; NSPCs, neural stem progenitor cells; CPCs, cardiac progenitor cells; CDCs, cardiosphere-derived cells; GFP-MSCs, green fluorescent protein expressing mesenchymal stem cells; ECs, endothelial cells; CMCs, cardiomyocytes; SMCs, smooth muscle cells; HA, hyaluronic acid; and MCAO, middle cerebral artery occlusion. GBM, glioblastoma.

hearts using LAD ligation [15]. Groups receiving a combined delivery of PF matrix and CMs showed higher cell survival and cardiac regeneration. Similarly, fibrin has been used as a cell carrier for the regeneration of CNS tissues. Fibrin encapsulated GFP-positive BM-MSCs (3×10^5 cells) were transplanted into the lesion cavity formed after a hemisection SCI model in rats [16]. A large number of GFP-positive cells were found in the gray matter of injured spinal cords in the cell/matrix treated group. However, fibrin also has certain limitations

Table 2. Synthetic polymeric biomaterials used as cell carriers to enhance cell survival, retention, and engraftment for effective tissue regeneration.

Animal model	Cell type	Biomaterials	Cell survival	Functional benefit	Ref
MI	BMSCs	PAs	Cell retention ↑	SMCs, ECs formed, cardiac function ↑	[27]
MI	ADSCs	PAs + PCLMA	Cell retention ↑	Cells differentiated into cardiac lineage	[28]
MI	FBC	PLGA microspheres	Cell viability ↑	N.R	[30]
MI	BMSCs	MPEG–PCL–MPEG	Cell retention ↑	Vascularization ↑ Cardiac function ↑	[34]
Brain surgery	NSCs	RADA16-IKVAV	Cell survival ↑	Formation of glial astrocytes, neuronal differentiation, brain regeneration	[29]
SC	ADSCs	MITCH	Cell retention ↑	N.R	[26]

Abbreviations: PAs, self-assembling peptides; HI, hypoxic-ischemic; PD, Parkinson's disease; MITCH, PCLMA, Poly(caprolactone 2-(methacryloyloxy) ethyl ester); Recombinant protein based hydrogels; PLGA, poly(L-lactide-co-glycolide); Glycosaminoglycans, GAGs; NGF, nerve growth factor; PCL, poly(caprolactone); FN, fibronectin; NT-3, neurotrophin-3; PLLA, poly(L-lactide), ADSCs, adipose-derived stem cells; BMSCs, bone marrow derived stem cells, NSCs, neural stem cells, NSPCs, neural stem progenitor cells; MSCs, mesenchymal stem cells; FBC, fetal brain cells; SC, subcutaneous implantation; MI, myocardial infarction; N.R, not reported; ECs, endothelial cells; and SMCs, smooth muscle cells; DCM, decellularized cartilage matrix; DBM, decellularized bone matrix.

when used as a cell delivery vehicle.

Similarly, previous works have demonstrated that tissue-engineered collagen-based scaffolds can provide a suitable microenvironment to support cell attachment and proliferation for the regeneration of infarcted myocardium (IM) [17]. For instance, cardiac patches developed from collagen and hMSCs (1×10^6 cells) enhanced cell engraftment in a coronary artery ligation model in rats [17]. Collagen-based biomaterials have also been used to enhance the survival and promote the differentiation of stem cells for the treatment of CNS disorders including TBI, SCI, Parkinson's disease, and ischemia. Guan et al. [18] confirmed that three-dimensional gelatinous collagen type I scaffolds enhanced the short-term retention and long-term survival of hMSCs in a TBI model in rats. By contrast, hMSCs without collagen showed a high tendency to diffuse away from the lesion site and only a few cells survived four weeks after transplantation. These findings indicate that collagen scaffolds not only hold hMSCs in the lesion site over time, but also influence the

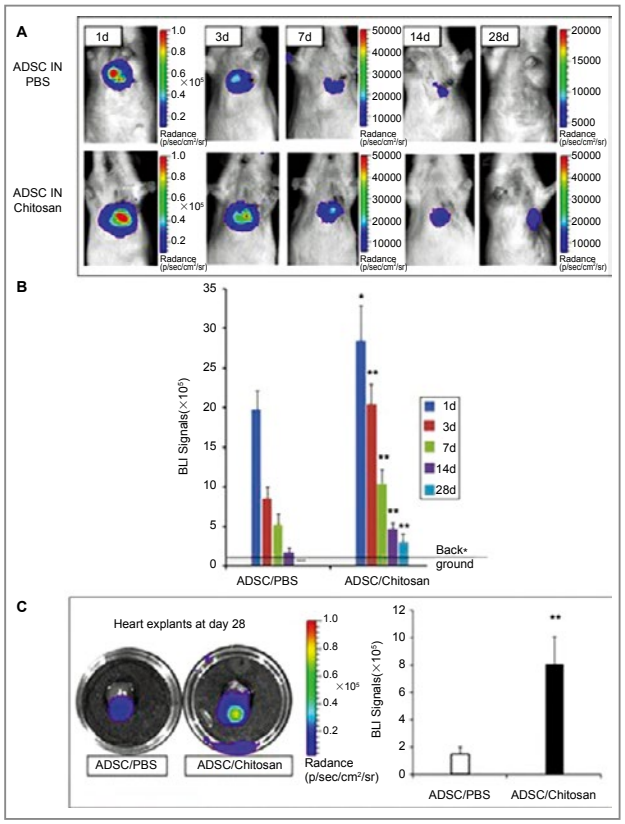

Figure 4. Transplantation of reporter-expressing ADSCs and molecular imaging with BLI. (A) Representative images of *in vivo* bioluminescence at days 1, 3, 7, 14 and 28 after ADSC transplantation. (B) Bioluminescence signals at different checkpoints were quantified and compared between ADSC/PBS and ADSC/chitosan groups. (C) To further determine survived ADSCs in ischemic hearts at day 28 after transplantation, BLI was performed on explanted hearts at day 28 as no signals could be detected in living animals of ADSC/PBS group. *p < 0.05; **p < 0.01. Image taken from [20] with permission.

differentiation and integration of transplanted hMSCs.

Alginate has also been employed as an injectable hydrogel for cell transplantation in several studies and has been shown to enhance cell survival and support vasculogenesis. In an attempt to enhance the retention of hMSCs in IM and to augment paracrine effects for cardiac regeneration, Patel et al. encapsulated hMSCs in alginate [19]. *In vivo* bioluminescent imaging (BLI) showed a greater retention of cells in animals treated with encapsulated hMSCs as compared to delivery by direct injection at all the time points tested. Despite the many advantages of alginate hydrogels, its degradation rate is an issue, since alginate is not naturally, enzymatically degraded in mammals. Therefore, it takes a long time for alginate hydrogels to completely degrade from an implantation site.

Similarly, chitosan hydrogels were reported to enhance stem cell survival, retention, and engraftment by rescuing ischemia-induced ROS *in vitro* and ameliorating the impaired adhesion of transplanted cells in IM [20]. Liu et al. transplanted ADSCs (4×10^6) in IM either using PBS (ADSCs/PBS) or chitosan hydrogels (ADSCs/chitosan) and assessed stem cell retention and therapeutic outcome for up to four weeks. It was demonstrated that chitosan could enhance the expression of integrins (α_v, β_1), adhesion molecules (intercellular adhesion molecule 1 and vascular cell adhesion molecule 1), and chemokines (SDF-1) in IM. ADSCs/chitosan treatment enabled higher retention of stem cells, as assessed by *in vivo* and *ex vivo* BLI (Figure 4). Similarly, Roche et al. studied the ability of a panel of biomaterials to enhance the initial cell retention at an infarct site [5].

Chitosan and chitin films have also been investigated for their ability to promote survival of transplanted NSPCs in injured spinal cord. GFP^+ NSPCs (1.5×10^6 cells) were seeded in chitosan tubes coated with LN and implanted in an injured rat spinal cord after transaction of the cord [21]. Stereological analysis showed excellent survival of transplanted cells (2.09 ± 0.35 GFP^+ cells) in the tissue bridges within the chitosan tubes five weeks after transplantation. Further analysis showed that $23.2 \pm 6.0\%$ of GFP^+ cells were CC1-positive oligodendrocytes, $9.9 \pm 1.2\%$ were GFAP-positive astrocytes, and $18.3 \pm 3.6\%$ were GFAP-positive nestin-expressing cells. However, none of the GFP-positive cells co-localized with the neuronal markers MAP-2 and NeuN, indicating that these cells may be in the preliminary stages of differentiation. These findings demonstrate that chitosan provided a conducive environment for the long-term survival of transplanted NSPCs, and the transplanted cells within the tubular constructs were able to enhance axon elongation through the lesion. However, since chitosan also aggravates the inflammatory response, it is not ideal for use in CNS tissue regeneration.

Healy and colleagues developed tunable HA hydrogels for cell transplantation and evaluated their potential for promoting cell survival *in vitro* and *in vivo* [22]. Heparin, RGD, TGF-β, and matrix metalloproteinase (MMP)-sensitive linkages were incorporated into these hydrogels. Bioactive HA hydrogels significantly enhanced the survival of CPCs *in vivo* for up to 32 days as shown by BLI imaging (Figure 5).

Similarly, using collagen-incorporated hyaluronan (Hystem–C™), Smith et al. showed better retention of CDCs *in vitro* and *in vivo* [23]. When delivered intramyocardially, these *in situ* polymerizable hydrogels showed more than a seven-fold increase in cell retention (~ 35% of the total cells delivered) in the IM after 24 hours as compared to both saline and collagen-free hyaluronan (Hystem™). Furthermore, quantitative PCR analysis of the cell engraftment rate showed significantly greater engraftment of cells in the Hystem–C™ group as compared with the saline group three weeks post-transplantation.

To enhance the survival and retention of GFP^+ NPCs (1×10^5) and GFP^+ ESC-derived NSCs (1×10^5) in a cortical photothrombotic stroke model, Zhong et al. used *in situ* gelling hyaluronan–heparin–collagen hydrogels [24]. Hydrogels enhanced the survival of transplanted cells (8,000 GFP^+ cells) two-fold as compared to the cells

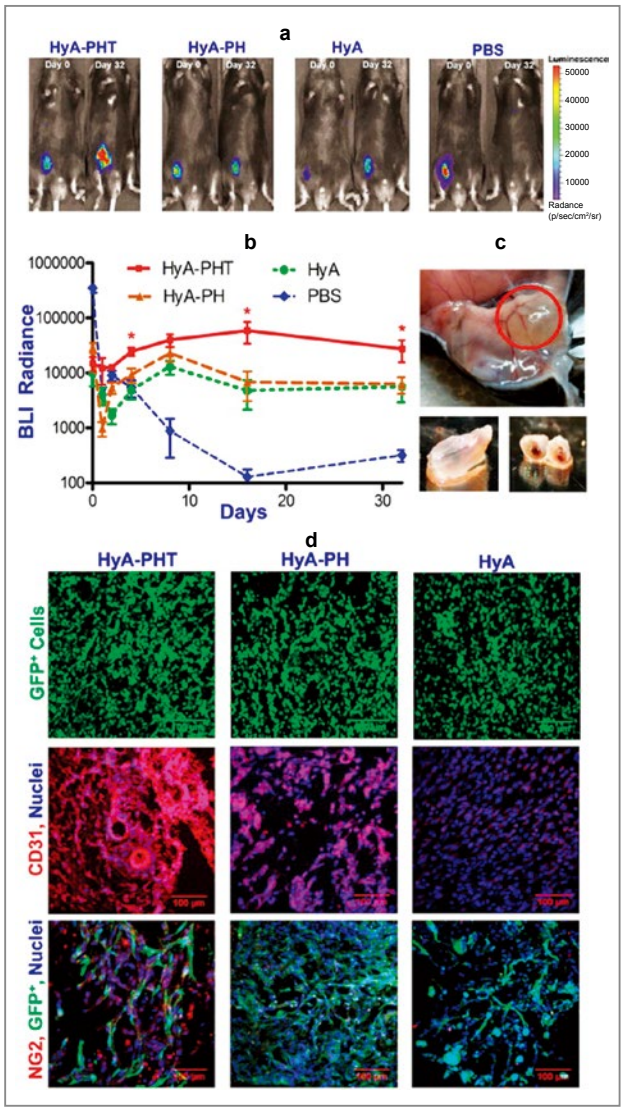

Figure 5. HyA-PHT hydrogels promoted CPC survival and endothelial differentiation *in vivo*. a) Bioluminescence post-implantation of GFP-fLuc-mCPCs (~500,000 cells in 100 mL gel) in syngeneic mouse hind limbs. b) Radiance generated by the transplanted CPCs over 32 days (n = 5) demonstrated that the hydrogels promoted cell survival and limited cell diffusion away from the implantation site *in vivo*. c) The transplanted HyA-PHT hydrogels recruited host vessels to the exterior of the implant and a competent vasculature was evident throughout the cross section of the implants. d) Verification of the persistence of donor CPCs with GFP expression and differentiation of CPCs into endothelial cells was confirmed by expression of CD31. HyA-PHT gels fostered significant and mature blood vessel formation, and infiltration of $NG2^+$ pericytes was observed with the donor GFP^+ cells. Scale bars = 100 mm. Image taken from [22] with permission.

transplanted without hydrogels (4,000 GFP^+ cells) 14 days after implantation. Hydrogels formed by covalent crosslinking are potentially susceptible to causing cytotoxic effects from reagents or reaction conditions, but the hydrogels formed by physical crosslinking suffer from weak mechanical properties and instability. With this in mind, Yeom and coworkers [25] designed supramolecular HA hydrogels using the strong and selective host–guest interaction between cucurbit [6] and 1,6-diaminohexane. GFP-transduced MSCs were encapsulated into these hydrogels and shown to express GFP for up to 60 days after subcutaneous implantation in mice. These hydrogels, which support the long-term survival of encapsulated cells, hold great promise for the treatment of cancer and other intractable diseases, such as ischemia, stroke, and spinal cord injury.

Synthetic biomaterials as cell vehicles

Naturally-derived biomaterials are conducive to *in vivo* microenvironments and are abundant; however, batch-to-batch variations tend to limit their therapeutic utility. Alternatively, synthetic polymers can be precisely designed with the required biodegradability and mechanical properties. Accordingly, various synthetic biomaterials have been used as cell carriers in various injury models. Heilshorn's group developed recombinant protein polymers that formed mixing-induced two-component hydrogel (MITCH) [26]. Additionally, hydrophilic spacers and tripeptide RGD were introduced to impart chain flexibility and cell-binding characteristics. MITCHs showed a several fold increase in cell retention and viability after subcutaneous implantation as compared to alginate, collagen, or saline treated groups as assessed by *in vivo* BLI (Figure 6) [26].

Self-assembling peptides (SAPs) are also attractive candidates as cell carriers and have been reported to enhance the survival and differentiation of transplanted

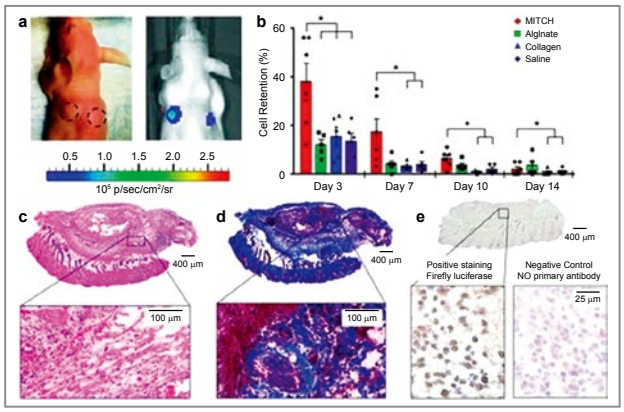

Figure 6. mASCs^{Fluc+} transplantation into nude mice. a) Representative mouse with injection sites demarcated with dotted lines (day 0, left) and with BLI total flux overlay (day 3, right). b) BLI measurements of cell retention. Data normalized to day 1 and reported as mean ± SEM; n = 5 or 6; *p < 0.0001. c) Hematoxylin and eosin staining of day 3 MITCH-ASC explant (cell nuclei, blue; red blood cells, red; protein and cytoplasm, pink). d) Trichrome staining of day 3 MITCH-ASC explant (cell nuclei, black; muscle and erythrocytes, red; fibrin, pink; collagen, blue). e) Immunohistochemical staining of injected mASCs^{Fluc+} in day 3 MITCH-ASC explant. Positive staining with firefly luciferase antibody (positive cells, brown, left) and negative control staining with no primary antibody (right). All cell nuclei counterstained with hematoxylin (blue). Image taken from [26] with permission.

cells. Lin et al. used SAPs to enhance cell retention and improve cardiac function after MI [27]. The combination of BMMNCs and SAPs synergistically improved cardiac function. Interestingly, SAPs improved the retention (29.3 ± 3.5 cells/mm^2 in the MI + BMMNCs treated group and 229.4 ± 41.4 cells/mm^2 in the MI + SAPs + BMMNCs treated group) and the differentiation ratio of transplanted cells into ECs and SMCs as assessed four weeks after transplantation.

Similarly, bioimplants consisting of RADA16-I (PuraMatrix™) and polycaprolactone methacryloyloxyethyl ester enhanced the survival of subcutaneous adipose tissue-derived progenitor cells (subATDPCs) for up to three weeks after subcutaneous implantation [28]. Cheng et al. designed SAP hydrogels containing LN-derived peptide sequence, Isoleucine-Lysine-Valine-Alanine-Valine (IKVAV) to enhance the survival and induce the differentiation of NSCs into neuronal lineages [29]. Animals receiving bioactive RADA and NSCs promoted neuronal differentiation of encapsulated NSCs. Therefore, it is apparent that SAPs can be tailored with bioactive factors to enhance cell survival and differentiation at an injury site. These findings underscore the potential of SAPs to enhance cell retention rate and induce myocardial regeneration.

A variety of synthetic biodegradable polyesters have been investigated as cell carriers. Mahoney and Saltzman used PLGA microparticles (0.5-5 mm in diameter) to encapsulate nerve growth factor (NGF) to deliver fetal brain cells [30]. The transplanted cells survived and remained at the site of injection throughout the 28-day period of study, suggesting that the NGF-enriched microparticles improved cell viability as compared to controls with BSA [30].

Enhancing the survival of transplanted cells using biological cues

Most synthetic polymers lack the adhesive sequences required for the survival of cells. This limitation can be overcome by introducing cell adhesive moieties, either whole or partial ECM proteins or cell-adhesive sequences onto polymers (Figure 7, Table 3) [31, 32]. For this purpose, ECM-derived peptides such as RGD, IKVAV, Tyr-Ile-Gly-Ser-Arg (YIGSR), Arg-Glu-Asp-Val (REDV), and Gly-Phe-Hyp-Gly-Glu-Arg (GFOGER) have been intensively investigated and shown to augment cell adhesion through integrin signaling [33, 34].

Adhesive cues may control the environment of transplanted cells, impact their survival, and enhance their ability to form new tissue structures. Photocrosslinkable chitosan hydrogels were endowed with an Ang-1-derived peptide (Gln-His-Arg-Glu-Asp-Gly-Ser, QHREDGS) to enhance the survival and retention of neonatal rat CMs *in vitro* and *in vivo* [35]. Bioactive hydrogels enhanced cell survival after subcutaneous implantation and CMs expressing cardiac-specific markers, sarcomeric α-actinin

Table 3. Design of biologically inspired biomaterials to enhance stem cell survival, retention, and engraftment for effective tissue regeneration.

Animal model	Cell Type	Biomaterials	Cell survival	Functional benefit	Ref
MI	MSCs	SAPs-RGDSP	Cell survival ↑, cell apoptosis ↓	Cardiac function ↑	[37]
MI	ESC-derived CMCs	MMPs cleavable SAPs-RGD	Cell survival ↑	Cells integrated with host myocardium	[39]
Infracted brain	iPSC-derived NPCs	RGD-immobilized HA matrix	Cell survival ↑ in RGD group	Cells differentiated into neurblasts	[32]
Brain surgery	NSCs	RADA16-IKVAV	Cell survival ↑	Glial astrocytes ↓ brain regeneration ↑	[29]
Brain injury	Fetal brain cells	PLGA microparticles NGF encapsulation	Cell viability ↑	N.R.	[30]
HI	BMPACs	SAPs-RGD	Cell retention ↑	Capillary density ↑, Limb perfusion ↑, Necrosis ↓	[38]

Abbreviations: N.R., Not reported, RGD, arginine-glycine-aspartic acid; Laminin, LN; SAPs, self-assembling peptide; PLGA, poly(L-lactide-co-glycolide); OD, osteo-chondral defect; NGF, nerve growth factor; PD, Parkinson's disease; BMP-2, bone morphogenetic protein-2; NT-3, neurotrophin-3; PD, Parkinson's disease; MSCs, mesenchymal stem cells; CMCs, cardiomyocytes; iPSCs, induced pluripotent stem cells; ESCs, embryonic stem cells; ODCs, oligodendrocytes; NSCs, neural stem cells; NPCs, neural progenitor cells; GCs, granule cells; PCs, purkinje cells; MCSCs, marrow derived cardiac stem cells; BMPACs, bone marrow derived pro-angiogenic cells; pMNs, progenitor motor neurons; HAP, hydroxyapatite; BMP-2, bone morphogenetic protein-2; SC, subcutaneous implantation; MI, myocardial infarction; HI, hind limb ischemia; and SCI, spinal cord injury.

and cardiac troponin, were identified seven days after implantation. Similarly, RGD-conjugated polymeric

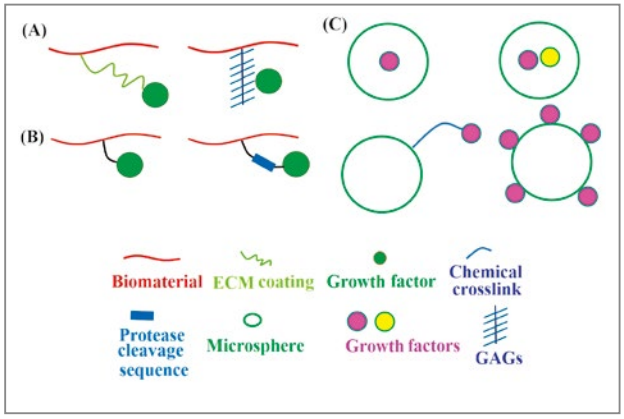

Figure 7. Strategies for attachment of bioactive molecules to biomaterials. (A) Strategies to non-covalently attach bioactive molecules to biomaterials using physical tools. Bioactive molecules can be absorbed on the surface of the biomaterial through coating of ECM protein or can be electrostatically associated with biomaterials via heparin linkage. (B) Strategies to covalently attach bioactive molecules using chemical tools. Protease-degradable amino acids sequences can be introduced into crosslinks to instruct release of signaling cues. (C) Methodologies for incorporation of bioactive molecules to microspheres. Bioactive molecules can be encapsulated, adsorbed on the surface, or chemically linked to the microspheres.

biomaterials were reported to enhance cell adhesion and retention and play a vital role in effective tissue regeneration [36].

Similarly, designer SAPs scaffolds have been modified with short functional sequences [37, 38]. Incorporation of RGDSP in RADA16 enhanced the survival of marrow-derived cardiac stem cells (MCSCs) after transplantation into IM in rats [38]. Interestingly, administration of MCSCs along with RGDSP-RADA16 significantly enhanced cardiac function, reduced fibrosis, and promoted survival and differentiation of transplanted cells into CMCs compared with cells alone, cells + RADA16, RGDSP-RADA16 alone, and RADA16 alone treated groups 28 days after implantation. This is attributed to the RGD motif, which not only promotes cell survival but also stimulates integrins necessary for cardiac development. Tongers et al. developed peptide amphiphiles (PA) presenting RGDS and assessed the efficacy of these engineered biomaterials for bone marrow-derived pro-angiogenic cells (BMPACs) and $CD34^{+}$ cell transplantation [38]. PA-RGDS hydrogels enhanced *in vitro* cell survival and proliferation, reduced

cell apoptosis through expression of pro-survival and pro-angiogenic pathways, and inhibited pro-apoptotic pathways. Delivery of BMPACs (1×10^5 cells) in concert with PA-RGDS three days after HLI revealed enhanced cell viability and retention in ischemic limbs in the PA-RGDS treated group for up to seven days as compared to BMPACs (1×10^5 cells) alone.

Similarly, Ban et al. designed MMP-degradable cell-adhesive PAs (PA-RGDS) and demonstrated their potential as vehicles for the transplantation of neonatal rat cardiomyocytes (NRCMs) and ESC-derived CMCs in a myocardial infarction model [39]. PA-RGDS enhanced retention and engraftment of NRCMs in an intact myocardium. Similarly, administration of ESC-CMs along with PA-RGDS showed higher cell retention in IM both in the short-term (four weeks) and the long-term (14 weeks). By contrast, in the cells-alone treated group only a few ESC-CMs survived at four weeks, whereas cells were hardly detectable 14 weeks after implantation. These results suggest that PA-RGDS provides the cells with a protective environment during the early stage of transplantation, which is critical for cell engraftment and survival, leading to improved retention and interaction with the host myocardium. Finally, new bioactive motifs (Lys-Leu–Pro–Gly-Trp-Ser-Gly, KLPGWSG; Phe-Ala-Gln-Arg-Val-Pro-Pro, FAQRVPP; and Gln-His-Leu-Pro-Arg-Asp-His, QHLPRDH) have been screened through phage display technology to enhance survival, differentiation, and engraftment of NSCs *in vivo* and conjugated with PAs [9, 40].

Influencing stem cell differentiation

Another therapeutic strategy is the delivery of pro-regenerative factors, such as Wnt, FGF, BMP, Hedgehog, and Notch that are normally secreted by the ECM and are vital to healthy tissues. Cytokines, chemokines, morphogens, and growth factors that regulate survival, proliferation, and/or differentiation may be incorporated in cell vehicles [41]. These bioactive cues may be encapsulated, conjugated, or physically absorbed with cell vehicles and can be spatially and temporally released depending upon the dose required or target tissue [42, 43]. Weissman's group evaluated the potential of osteogenic microniches consisting of a hydroxyapatite (HAP)-coated BMP-2-releasing scaffold to instruct the *in vivo* differentiation of transplanted ESCs and iPSCs in large 4-mm critical-sized calvarial defects [44]. It was demonstrated that scaffolds releasing BMP-2 induced osteogenic differentiation of transplanted cells and showed considerably higher expression of osteogenic markers such as runt-related transcription factor 2 (RUNX2) and osteocalcin (OCN) as well as bone formation (96% bone regeneration after eight weeks as revealed by MicroCT imaging) compared with the standard PLGA-HAP scaffolds. These findings suggest that the local cues from both the implanted scaffold/cell micro-niche and surrounding macro-niche may act in concert to promote cellular survival and the *in vivo* acquisition of a terminal cell fate, thereby allowing for functional engraftment of iPSCs into regenerating tissue.

Enhancing functional integration and repair

Engraftment of transplanted cells with host cells and/or organs holds great potential for tissue repair. Moreover, engraftment of transplanted cells with a vascular system may enhance cell viability, especially in the case of thick tissue constructs. One strategy for augmenting integration between transplanted cells and host cells may be the use of angiogenic growth factors along with transplanted cells to promote vascularization. Alternatively, transplantation of cells or progenitors in concert with bioactive molecules may also contribute to the formation of new blood vessels that enhance cell survival and tissue repair [45].

Future directions and conclusions

As summarized above, stem cell manipulations and various approaches to biomaterial development have been used to enhance the efficacy of cell therapy. Both naturally-derived and synthetic biomaterials have been used as cell carriers, but each type of biomaterial tested to date has had its own set of shortcomings to offset its distinct benefits.

It is hoped that the discovery of new materials that combine variable cues (e.g., biological molecules, adhesion ligands, adjustable ligand densities, cytokines, and growth factors), the screening of suitable biomaterials depending upon the intended application, and the precise design of biomaterials may alleviate these shortcomings and enhance cell transplantation efficiency and associated therapeutic benefits [86]. Smart biomaterials can be designed as cell vehicles that can extend the viability of transplanted cells *in vivo*, control the differentiation of those cells into particular lineages, and allow for the precise release of cells [43, 46]. Moreover, delivery of signaling molecules that can enhance cell retention or promote differentiation and engraftment *in vivo* along with stem/progenitor cells is a promising, albeit challenging approach.

Precise qualitative and quantitative modification, functionalization, or decoration of natural and synthetic polymeric biomaterials, keeping the *in vivo* microenvironment in mind, may further enhance our understanding of cell-enhancement mechanisms. New technologies have to be developed that allow for local drug/growth factor delivery together with transplanted stem/progenitor cells as well as tighter control of the microenvironment of transplanted cells.

Many studies have focused on short-term cell retention (< two weeks) and only a few groups have investigated the long-term retention of transplanted cells. The long-term survival of stem cells is another important goal of stem cell therapy but is more challenging to improve on than short-term cell retention. The ischemic environment is an inflammatory one that is hostile to transplanted cells. Thus, biomaterials with anti-inflammatory and angiogenic properties can enhance the survival and engraftment of cells [47]. Since several tissues, including cardiac and neural tissues, need electromechanical stability and electromechanical integration between transplanted cells and host cells, long-term *in vivo* follow-up or imaging of transplanted cells may unveil the mechanisms associated with their therapeutic benefits.

Acknowledgment

This work was supported by the Ministry of Trade, Industry and Energy, Republic of Korea (Project Number 10052732).

References

[1] Song H et al. *Proc. Natl. Acad. Sci. U.S.A.* 2010; 107: 3329–3334.
[2] Nori S et al. *Proc. Natl. Acad. Sci. U.S.A.* 2011; 108: 16825–16830.
[3] Mangi AA et al. *Nat. Med.* 2003; 9: 1195–1201.
[4] Miyahara Y et al. *Nat. Med.* 2006; 12: 459-465.
[5] Roche ET et al. *Biomaterials* 2014; 35: 6850–6858.
[6] Khatiwala R et al. *Stem Cell Rev. Rep.* 2016; 12: 214-223.
[7] Shafiq M et al. *Biomaterials* 2016; 90: 85-115.
[8] Segers VFM. *Circ. Res.* 2011; 109: 910–922.
[9] Caprini A et al. *Nat. Biotechnol.* 2013; 30: 552–562.
[10] Kim JH et al. *Biomaterials* 2013; 34: 1657-1668.
[11] Lutolf MP et al. *Nat. Biotechnol.* 2005; 23: 47–55.
[12] Jin K et al. *J. Cereb. Blood Flow Metab.* 2010; 30: 534–544.
[13] Kofidis T et al. *Circulation* 2005; 112: I173-1177.
[14] Xiong Q et al. *Stem Cells* 2011; 29: 367–375.
[15] Habib M et al. *Biomaterials* 2011; 32: 7514–7523.

[16] Itosaka H et al. *Neuropathology* 2009; 29: 248-257.
[17] Simpson D et al. *Stem Cells* 2007; 25: 2350–2357.
[18] Guan J et al. *Biomaterials* 2013; 34: 5937–5946.
[19] Levit RD et al. *J. Am. Heart Assoc.* 2013; 2: e000367.
[20] Liu Z et al. *Biomaterials* 2012; 33: 3093–3106.
[21] Parr AM et al. *J. Neurotrauma* 2007; 24: 835-845.
[22] Jha AK et al. *Biomaterials* 2015; 47: 1–12.
[23] Smith RR, Marbán E, Marbán L. *Biomatter* 2013; *3*: pii: e24490.
[24] Zhong J et al. *Neurorehabil. Neural Repair* 2010; 24: 636-644.
[25] Yeom J et al. *Adv. Healthc. Mater.* 2015; 4: 237-244.
[26] Parisi-Amon A et al. *Adv. Healthc. Mater.* 2013; 2: 428–432.
[27] Lin Y-D et al. *Circulation* 2010; 122: S132–S141.
[28] Soler-Botija C et al. *Am. J. Transl. Res.* 2014; 6: 291–301.
[29] Cheng T-Y et al. *Biomaterials* 2013; 34: 2005–2016.
[30] Mahoney MJ. *Nat. Biotechnol.* 2001; 19: 934–939.
[31] Kim IG et al. *Biomaterials* 2015; 50: 75–86.
[32] Lam J et al. *Adv. Funct. Mater.* 2014; 24: 7053-7062.
[33] Hubbell JA et al. *Nat. Biotechnol.* 1991; 9: 568–572.
[34] Martino MM et al. *Sci. Transl. Med.* 2011; 3: 100ra89.
[35] Rask F et al. *Soft Matter* 2010; 6: 5089–5099.
[36] Lee SH et al. *Key Eng. Mater.* 2007; 342-343: 157–160.
[37] Guo H-D et al. *Biochem. Biophys. Res. Commun.* 2010; 399: 42–48.
[38] Tongers J et al. *J. Mol. Cell Cardiol.* 2014; 74: 231–239.
[39] Ban K et al. *ACS Nano* 2014; 8: 10815–10825.
[40] Gelain F et al. *Nanoscale* 2012; 4: 2946–2957.
[41] Leong W et al. *Trends Biotechnol.* 2015; 33: 653–665.
[42] Tessmar JK et al. *Adv. Drug Deliv. Rev.* 2007; 59: 274–291.
[43] Mooney DJ et al. *Cell Stem Cell* 2008; 2: 205-213.
[44] Levi B et al. *Proc. Natl. Acad. Sci. U.S.A.* 2012; 109: 20379–20384.
[45] Yu J et al. *Biomaterials* 2012; 33: 8062–8074.
[46] Vegas AJ et al. *Nat. Med.* 2016; 22: 306–311.
[47] Su J et al. *Biomaterials* 2010; 31: 308–314.

Feature Articles

Spatiotemporally Defining Biomolecule Preconcentration by Merging Ion Concentration Polarization

Rho Kyun KWAK
Center for BioMicrosystems
Brain Science Institute
rhokyun@kist.re.kr

Introduction

Microfluidic devices for molecular detection have been extensively pursued due to the many well-documented advantages of such systems including rapid analysis, less consumption of samples and reagents, and the potential for massive parallelization and automation. However, efficient world-to-chip interfacing, sample preparation, and concentration of low-abundance analytes remain as challenges, especially for non-nucleotide targets. The focus of this article is on KIST's efforts in developing a novel preconcentration system for integration into commercial analysis equipment.

Ion concentration polarization (ICP) has been frequently observed in various electrochemical systems (e.g., electrodialysis, fuel cells, and batteries) with ion exchange membranes [1, 2]. As the membrane transfers only cations or anions, the ion concentration at one side of the membrane decreases (ion depletion), whereas it increases at the other side (ion enrichment). This polarization effect reduces the system's efficiency because it induces an additional voltage drop (a.k.a. concentration overpotential) [1, 3]. Additionally, ion transport is limited when the lowest ion concentration in the ion depletion zone reaches zero (diffusion-limited transport). Indeed, ICP is not desirable in conventional applications; however, researchers have found a way to use this phenomenon for sample pretreatment in microfluidics through filtration [4-7] and preconcentration [8-10] applications. In particular, ICP preconcentrators show very robust and high

performance for any charged target sample. Therefore, enormous modulations of the membrane material (e.g., Nafion, charged hydrogel, and nanochannels) [8, 9, 11-13], geometry (batch-types with single/dual channels [14-17], continuous-flow types [4, 18], and multiplexed systems [19, 20]), and integration (droplet microfluidics [18, 21] and sensors [22]) of ICP preconcentrators have been possible.

Despite extensive research in the use of ICP preconcentrators, there are no clear operating conditions for the development of stationary preconcentrated plugs. Conventionally, to preconcentrate targets, electro-osmotic flow (EOF) or pressure-driven flow toward the ion depletion zone is required [23]. This flow prevents the propagation of the depletion zone and delivers the targets to be condensed [4, 9]. Zangle et al. [24] clarified the conditions of non-propagating ICP and propagating ICP, but they depend on all of the given parameters (channel geometry, sample mobility, and ionic strength). Because of this, determining operating conditions is almost impossible in real experiments. Even if the operating conditions were designated, they would be valid only for one target in one solution. Yossifon et al. [25] successfully demonstrated that propagation of the depletion zone was slowed by focusing the electric field geometrically; however, this method cannot suppress the propagation perfectly (the length of the depletion zone increases as a higher voltage is applied). To overcome this issue of a transient depletion zone, Senapati et al. and Slouka et al. developed ion selective membrane sensors by using ion enrichment and the membrane itself as a sensor [26, 27]. Although the preconcentration of nucleic acids was clearly demonstrated, this method should hold the membrane materials and the sensing point on the membrane. Accordingly, there are geometric / material limits to the enormous modulations listed above.

In this article, we demonstrate a novel ICP preconcentrator that can condense targets in a spatiotemporally defined region using various samples and under various operating conditions. Departing from a previous strategy (pushing flows), the ion enrichment zone is merged to stop the propagation of the ion depletion zone between two identical cation exchange membranes. We characterize the merging dynamics of the ICP and prove that the overlapping ICP zone is stabilized and stationary. The preconcentration plug is always in a predicted location, i.e., between the membranes, even when the operating conditions (voltage and time), samples (dye and protein), and solutions (ionic strength and pH) are changed. This system successfully maintains the plug's location until a protein is condensed up to 10,000-fold (within ~10 min).

Theoretical concept

When a relatively low voltage or current is applied, ion enrichment and depletion zones have linear ion concentration profiles by balancing diffusion and electromigration [1, 8, 9, 28]. Weak linear ICP does not change the electric resistance of the system; therefore, we obtain a resistor-like linear current-voltage response (a.k.a. Ohmic regime). At higher voltage, the slope of a linear concentration profile becomes steeper and the lowest ion concentration in the depletion zone will reach zero at the interface of the electrolyte and the membrane. At this moment, the slope is maximized and the current is saturated even when we apply a higher voltage (a.k.a. limiting regime with limiting current [1, 3]). This linear ICP model explains two current regimes: Ohmic and limiting.

In microfluidic channels, the surface charges of the channel/membrane are significant. This surface charge and strong electric field can lead to nonlinear ion transport in the depletion zone. Dydek et al. [29] categorized three transport mechanisms outside of diffusion and electromigration: surface conduction, electro-osmotic flow at the dead end, and electroconvection (EC) [30, 31]. All of these mechanisms yield two distinct characteristics: a flat ion depletion zone with significantly

low conductance and an overlimiting current (higher current by overcoming diffusion-limited ion flux). This flat depletion zone is impenetrable to any charged particle because there are not enough ions to screen their surface charges [9]. For preconcentration applications, EOF and/or pressure-driven flow push the particles toward this zone. Next, the particles are condensed at the depletion zone's boundary. In this scenario, if the flow is too weak, then the ion depletion zone expands (propagating ICP) [24], whereas if the flow is too strong, then it bursts (bursting ICP) [32]. The preconcentrated plug will stay in the field of view for at least 10 min only when these two conditions are balanced (nonpropagating ICP) [24, 32]. Therefore, for a single preconcentration test, we need to find a proper set of applied voltage and flow velocity conditions manually. This is why previous ICP preconcentrators have not been able to escape the use of microscopes and fluorescent tracers to monitor preconcentration action [4, 9, 16-18, 20-22].

To overcome this issue, we suggest a novel spatiotemporally defined ICP platform that can preconcentrate targets at a designated region under any conditions, including a variety of targets, applied voltages or currents, ionic strengths, and pH values (Figure 1). For this purpose, we initiate an ion enrichment zone in response to the ion depletion zone by patterning two cation exchange membranes (Nafion). These thin Nafion membranes (thickness < 1 μm) are positioned on the bottom of a microchannel (see Experimental methods). The ends of the Nafion lines are placed in buffer reservoirs to apply the electric field. When voltage is applied through the two Nafion membranes, ion depletion (enrichment) zones occur on the anodic (cathodic) side of the membranes. Then, two ICP zones are merged and remain between the membranes (Figure 1b-c). This is because cations can circulate from the anode to the cathode along two Nafion membranes and the merged ICP zone. In previous systems, one Nafion keep removes cations in the channel, so the ion depletion zone should expand by sending anions toward the anode [9, 24] (those anions are then neutralized by Faradaic reaction on the anode). However, here we supply the same amount of cations as those being removed through one more Nafion membrane, which is connected to the reservoir and the anode. Therefore, the anions between two Nafion membranes do not need to be sent toward the anode. The anions (and cations also) are just redistributed to generate a steady concentration gradient and constant cation flux in the merged ion enrichment-depletion zone with a linear slope (Ohmic and limiting regime, Figure 1b) or a nonlinear slope (overlimiting regime, Figure 1c). In the overlimiting case, the steeper concentration gradient drives a larger ion flux by diffusion and electromigration in the enrichment part, and this larger flux is matched by convection with vortices in the depletion part (we will address the source of the vortices in the next section).

Consequently, the location of the preconcentration plug is also confined. As shown in Figure 1a, the charged targets (hollow circles) are preconcentrated on the interface of the ion depletion and enrichment zones (curved dotted line). The channel wall is negatively charged, and this generates the EOF between the Nafion membranes by the electric field. This EOF delivers charged particles toward the interface. Although the preconcentration process is similar to that of previous systems [9], in this ICP platform, preconcentration always occurs over a wide range of applied voltages at a predicted point between two Nafion membranes: **i)** even under a weak EOF, the ion depletion zone does not need to be expanded as described above (no propagating ICP), and **ii)** even under a strong EOF, its velocity cannot be larger than that of the recirculating flow (vortices) by EOF mismatching (no bursting ICP) [33]. In detail, the EOF velocity can be defined by the Helmholtz-Smoluchowski equation [1], $u_{EOF} = -\varepsilon\zeta E/\mu$ (ε: permittivity; ζ: zeta potential of the wall; E: electric field; and μ: dynamic viscosity). Because ion concentration in the depletion zone is significantly low, most of the voltage V drops and a higher electric field is generated than that in the enrichment zone. Hence, the speed of

EOF increases across the interface of the depletion-enrichment zones. As a result, this induces recirculating back flow, i.e. vortices, to maintain fluid mass [33] (Figure 1d). Using a similar theoretical analogy as that in Minerick et al. [33], the EOF flow rate in the enrichment zone (Q_{EOF1}) is equal to the total flow rate in the depletion zone by EOF (Q_{EOF2}) and pressure-driven recirculating flow (Q_{HP}):

$$\frac{\varepsilon\zeta E_1}{\mu} = \frac{\varepsilon\zeta E_2}{\mu} + \left(-\frac{dP}{dx}\right)\frac{w^3 h}{12\mu} \quad (1)$$

$$\left(-\frac{dP}{dx}\right) = \frac{12\mu\zeta}{w^2}\left(E_1 - E_2\right) \quad (2)$$

where E_1 and E_2 are the electric field in the enrichment and depletion zones, respectively. P is pressure, w is the channel width, and h is the channel height. With a stronger electric field in the depletion zone ($E_1 < E_2$), the direction of the pressure gradient ($-dP/dx$) and corresponding flow are reversed, as shown in Figure 1d. Here, the depletion zone will not burst if the EOF velocity in the enrichment zone (u_{EOF1}) is slower than the averaged back flow velocity in the depletion zone (average (u_{HP})):

$$\left|\frac{\varepsilon\zeta E_1}{\mu}\right| < \left|\left(-\frac{dP}{dx}\right)\frac{w^2 h}{12\mu}\right| \quad (3)$$

By substituting the equation (2), this no bursting condition is simplified by the ratio of the electric fields in the depletion and enrichment zones:

$$E_2 / E_1 > 2 \quad (4)$$

Typically, the ion concentration in the depletion zone is decreased to less than 1% of the initial concentration [6, 7]. Approximately, the electric field is inversely proportional to the ion concentration, resulting in E_2/E_1~100. This value is much larger than the threshold ratio of 2. In this regard, the new ICP platform has no propagating or bursting modes of ICP. The merged ICP zones between the two Nafion membranes are unconditionally stationary; thus, we can preconcentrate any charged target under any given conditions.

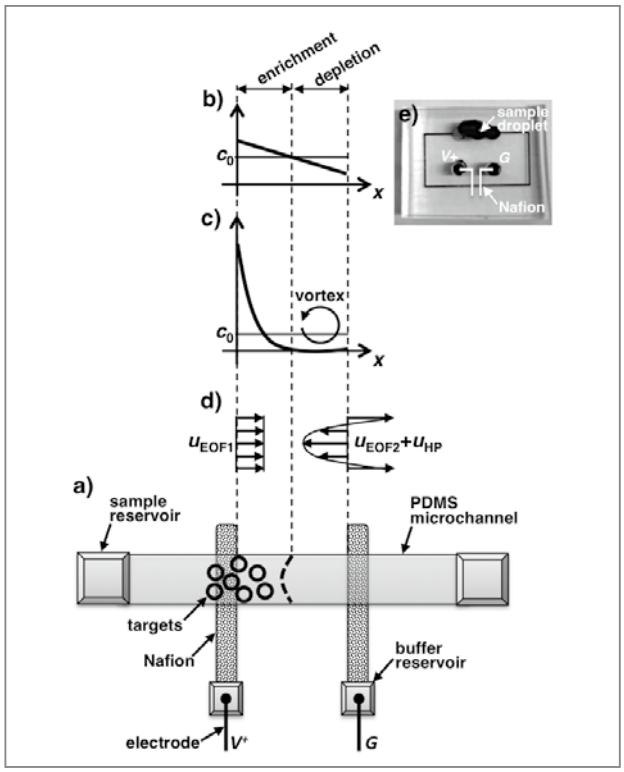

Figure 1. Schematic of a spatiotemporally defined preconcentrator. a) Targets (black hollow circles) are preconcentrated between two Nafion strips, which are line-patterned on the bottom of the PDMS channel. b-c) Schematic ion concentration profiles between the Nafion membranes by merging the ion enrichment and depletion zones. A linear concentration profile occurs in the Ohmic and limiting regimes (Figure 1b), whereas a nonlinear concentration profile occurs in the overlimiting regime with vortices (circular arrow, Figure 1c). C_0 indicates the initial ion concentration. d) Schematic profiles of flow velocity in the enrichment and depletion zones. e) The fabricated device.

Experimental methods

The spatiotemporally defined preconcentrator described in this study was fabricated with two Nafion

lines on a glass substrate and one poly(dimethylsiloxane) (PDMS) channel (Figure 1e). Using the micro-flow patterning method [19], Nafion perfluorinated resin (20 wt %, Sigma-Aldrich, St. Louis, MO) was patterned along a PDMS mold, which had two parallel channels (width: 100 μm; height: 50 μm; interchannel distance: 100-500 μm) resulting in two Nafion lines on a glass substrate (white lines, Figure 1e). This Nafion-patterned substrate was bonded with the PDMS microchannel (width: 50-100 μm; height: 10 μm) by oxygen plasma treatment. In this device, two buffer reservoirs were positioned on the Nafion membranes to apply the electric field, and two sample reservoirs were located at the ends of the channel. In the buffer reservoirs, a 1 M NaCl solution was filled to compensate for the ICP effect in these reservoirs. After filling the channel with sample solutions, we released one large droplet to connect the sample reservoirs. This process caused the pressure gradient to be zero across the channel. In this way, we were able to eliminate undesirable pressure-driven flows. PDMS channels were fabricated by conventional molding and photolithography.

To visualize the ICP phenomenon and preconcentration action, a negatively charged fluorescent dye (1.55 μM Alexa Fluor 488, Invitrogen, Carlsbad, CA) was added to various test solutions: 1-100 mM NaCl solution (pH~7), the mixture of 1 mM NaCl and 0.2 mM HCl (pH~3.7), and the mixture of 1 mM NaCl and 0.2 mM NaOH (pH~10.3). The dye's fluorescence intensity follows the ion concentration qualitatively [31, 34, 35]. Fluorescent images were obtained using an inverted epifluorescence microscope (Olympus, IX-71) and a charged-coupled device (CCD) camera (Hamamatsu Co., Japan). The obtained images were analyzed using ImageJ software. dc voltage was applied with Ag/AgCl electrodes, and the current responses were measured with a source measurement unit (Keithley 2635A, Keithley Instruments, Inc., Cleveland, OH).

Results and discussion

ICP phenomenon between two Nafions

First, we visualized the ICP phenomenon between two Nafion membranes, as represented by the current-voltage response, fluorescence images, and intensity profiles (Figure 2). The ion enrichment (depletion) zone occurs from the Nafion membranes on the left (right), which has a higher (lower) fluorescence intensity than the reference value at 0 V. The two ICP zones smoothly overlap between the Nafions. For a similar ICP with a single membrane [9, 29, 30], the merged ICP has three current regimes (Ohmic, limiting, and overlimiting) with distinct characteristics (Figure 2a). The Ohmic and limiting regimes (0.5-1 V) have linear concentration

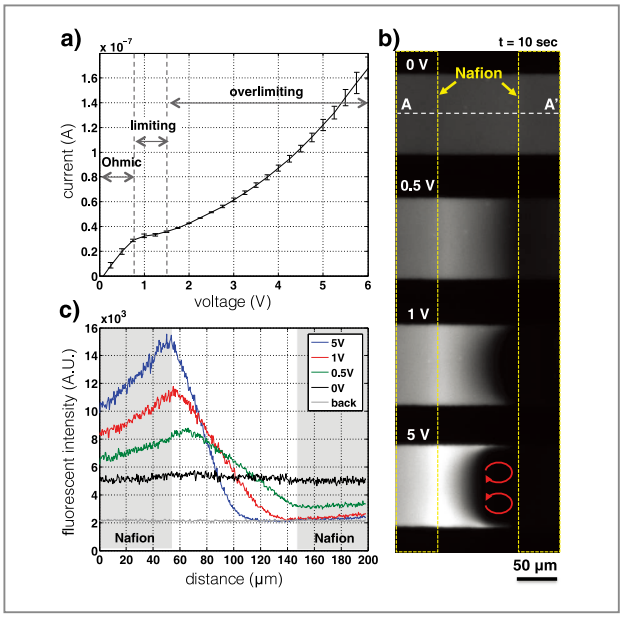

Figure 2. Merged ICP phenomenon between two Nafion membranes. a) Current-voltage curve shows three distinct regimes (Ohmic, limiting, and overlimiting). The current-voltage response is measured by ramping up at discrete intervals of 0.25V every 40 s, which is repeated three times. b-c) In the three regimes, fluorescence images (Figure 2b) and intensity profiles along *A-A'* at the middle of the channel (Figure 2c) were obtained. Yellow dotted boxes indicate the location of the Nafion membranes. We used the device with a PDMS microchannel (width: 100 μm; height: 10 μm) and two patterned Nafion membranes (width: 100 μm; inter-Nafion distance: 100 μm; height: ~1 μm). A 1mM KCl solution with 1.55 μM (1μg/mL) Alexa Fluor 488 was used.

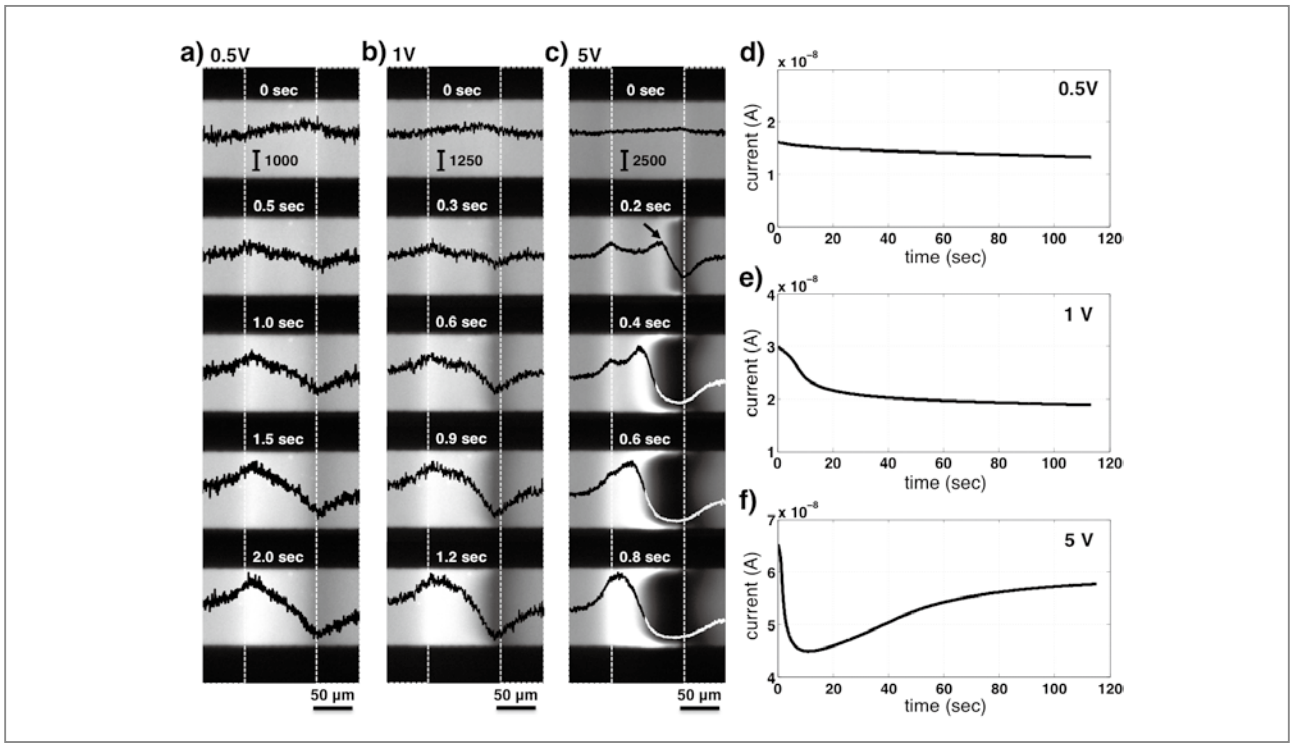

Figure 3. Dynamics of merging the ion depletion and enrichment zones. a-c) Concatenated concentration profiles measured from fluorescence images after applications of a constant voltage. The intensity curves are on different scales: 1000 A.U. (0.5V; a), 1250 A.U. (1V; b), and 2500 A.U. (5V; c). Initially, freestanding ion enrichment and ion depletion are visualized. d-f) During this operation, current-time responses are also measured for 115 s in every 0.1 s increments.

profiles, and their slopes indicate (approximately) the level of the currents (Figure 2b-c). The lowest intensity reaches the background signal in the limiting regime (1 V, red line at 150 μm), which indicates that the lowest ion concentration is nearly zero [1, 30]. With linear transport mechanisms (diffusion and electromigration), the current fluctuation is negligible (Figure 2a). In contrast, the overlimiting regime (5 V) shows a nonlinear intensity profile with a flat depletion zone by rejecting most ions (and dyes) (at 100-150 μm, Figure 2c). In this flat zone, a vortex pair generates a curved depletion boundary (red arrows, Figure 2b) and current fluctuation (> 2 V, Figure 2a) [9, 29].

Merging dynamics of ICP

From a more microscopic perspective, Figure 3 shows transient dynamics as the ion depletion and ion enrichment zones overlap. In the Ohmic and limiting regimes (0.5-1 V), linear concentration gradients evolve from both Nafion membranes (< 1 s), and they are then connected together (> 1 s) (Figure 3a-b). In the overlimiting regime (5 V), vortices drive the formation of a strong ion depletion zone and a preconcentration shock on the boundary by pushing the dyes (black arrow at 0.2 sec, Figure 3c). The two ICP zones are also overlapped, but this happens more quickly (< 0.6 s). The current-time responses in all three regimes show an initial drop in the current, which represents the development of a depletion zone with a low concentration (and a corresponding high electric resistance) (Figure 3d-f). Similar to previous work, the weak linear ICP in the Ohmic/limiting regime (0.5-1 V) does not significantly reduce the current level. However, the merged ICP in the overlimiting regime (5 V) shows a unique current-time response,

i.e., current recovery (Figure 3f). Previous studies presented exponential current drops in this regime [35, 36]. This current recovery is due to **i)** the electric field, vortices, and corresponding flat depletion zones, which are confined together in a very small region between the Nafion membranes, and **ii)** convective transport by vortices that can be strong enough to compensate for the reduction of diffusion and electromigration in the low ion concentration zone. The currents ultimately saturate, which indicates steady and merged concentration profiles (Figure 3d-f).

Spatiotemporally defined preconcentration

After the ICP zones are merged with the stationary concentration profile and a constant current, the fluorescent dyes are stably condensed (Figure 4a). As time passes and the EOF delivers the dye molecules, the fluorescence intensity increases continuously (Figure 4b-c). The peak location is fixed near ~60 μm, and the preconcentrated dye molecules diffuse out toward the left (< 60 μm). This is because the electric field is biased through a short cut, from the right edge of the left Nafion membrane (at ~50 μm) to the left edge of the right Nafion membrane (at ~150 μm), and because there is no electric barrier on the left side, whereas the barrier (the depletion zone) prevents diffusion on the right side.

All of the tendencies described above are the same at higher voltages in the overlimiting regime (10-50 V, Figure 5), whose values have been typically used for previous preconcentrators [9]: **i)** fixed peak locations weighted toward the left Nafion membrane (ion enrichment part), **ii)** diffusion out of the preconcentrated plug toward the left side (Figure 5b), and **iii)** current recovery up to the initial level (Figure 5c). As a stronger EOF is generated by a higher voltage, the peak's location shifts to the right (Figure 5b) and a faster preconcentration can be achieved (Figure 5d). Notably, the preconcentration plug also becomes sharper because a strong EOF and recirculating vortices flowing in opposite directions can compress the plugs better. From

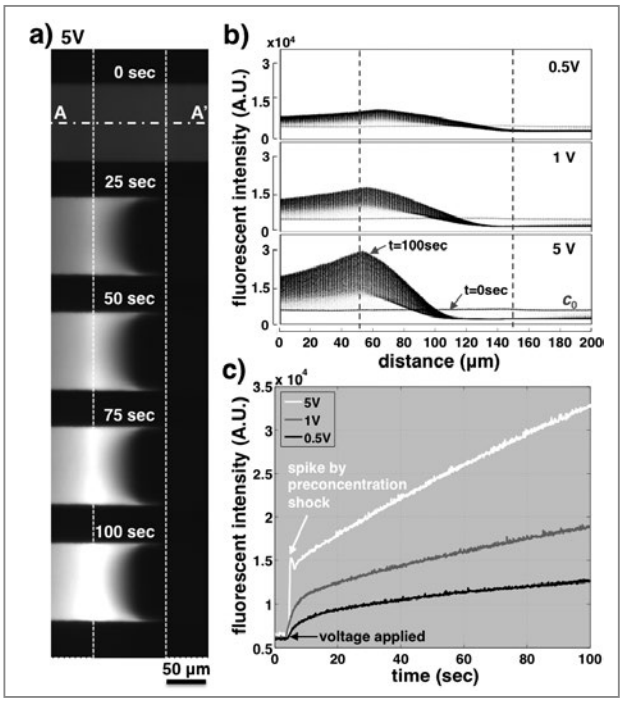

Figure 4. Spatiotemporally fixed preconcentration in three current regimes. a) Time-lapse fluorescence images after merging ICP zones at 5 V. White dotted boxes indicate the location of Nafion membranes. b) Along the middle of the channel (*A-A'*), time-lapse intensity profiles are stacked over 100 s. Although the peak intensity increases as dye molecules are preconcentrated, the peak locations are not changed. The initial intensity profile forms evenly at ~6000 A.U.. c) Peak fluorescence intensity presented over time. Initially, at 5V, a spike is observed by the preconcentration shock (black arrow, Figure 3c). The time-lapse profiles and peak intensities were measured every 0.1 s.

the peak intensity-time curves in Figure 5d, we define the preconcentration speed as the slope of the linear regime (Figure 5e). As observed, the speed is linearly proportional to the applied voltage (5-30 V). However, at 50 V, the peak fluorescence intensity is different from the tendency; as Green et al. [37] indicated, dye molecules are mostly trapped at the stagnation points at the corners of the wall and the Nafion membrane. This induced stronger confinement of the preconcentration plug and higher peak intensity. The preconcentration speed is gradually reduced, presumably due to unfavorably fast diffusion by the strong concentration gradient (< 350 μm, Figure 5b).

In addition to the spatiotemporally fixed precon-

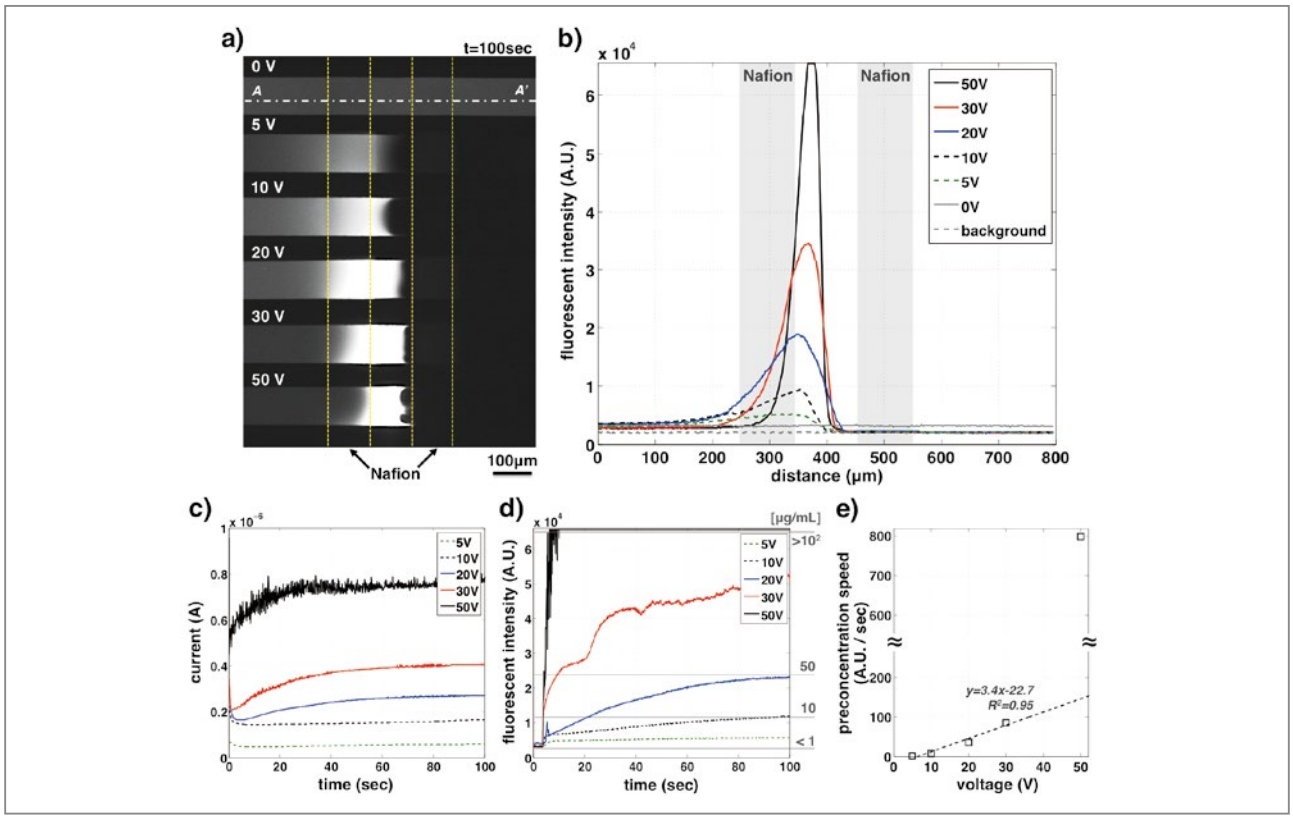

Figure 5. Spatiotemporally defined preconcentration at various operating voltages (5-50V). a) Fluorescence images after 100 s of operation and b) fluorescence intensity profiles along *A-A'*. Yellow dotted boxes indicate the location of Nafion membranes. c) In these high voltage tests, currents also fully recovered the initial values. d) Peak fluorescent intensities traced over 100 s along the reference lines, which indicate the actual concentration of fluorescent dyes (1-100 μg/mL of Alexa Fluor 488 in 1mM KCl solution). The same device is used in Figure 2-4. e) In addition, preconcentration speeds are calculated from the linear regime of the peak intensity-time curves in Figure 5d. Under 30V, the preconcentration speed is linearly proportional to the applied voltage (the dotted line is the linear fitting curve), whereas the speed is much faster at 50V.

centration over a wide voltage range (0.5-50 V), we verify that the preconcentration plug is also stationary between Nafion membranes, even at various ionic strengths (1-100 mM NaCl), pH values (3.7-10.3) and under 10-100 V (Figure 6). Generally, a high ionic strength weakens the ICP phenomenon because there are many ions available to compensate for the mismatched cations and anions near the membrane [1, 3, 8, 9]. The zeta potential of the channel wall and EOF are also weakened for the same reason [38]. As a result, the preconcentration fold of the peak intensity (after 100 s) becomes lower with higher ionic strength solutions (10-100 mM, Figure 6b). High or low pH induces co-ion leakage on Nafion membranes [39], and low pH also induces a decrease in the PDMS's zeta potential (and EOF) [38]. As a result, we obtained the weakened ICP preconcentration with an acidic or a basic solution (Figures 6a and 6c). Although the ICP and preconcentration performances are diminished under these unfavorable conditions, it is important that the preconcentration plugs remain between the two Nafion membranes. Enhancing the EOF and Nafion membranes' conductance permits this weakened ICP to be restored through various modulations, including higher applied voltage, shorter inter-Nafion distance, wider cross-sectional area of the Nafion membrane, narrower channel width (Figure 7), and divided channels, like that for EOF

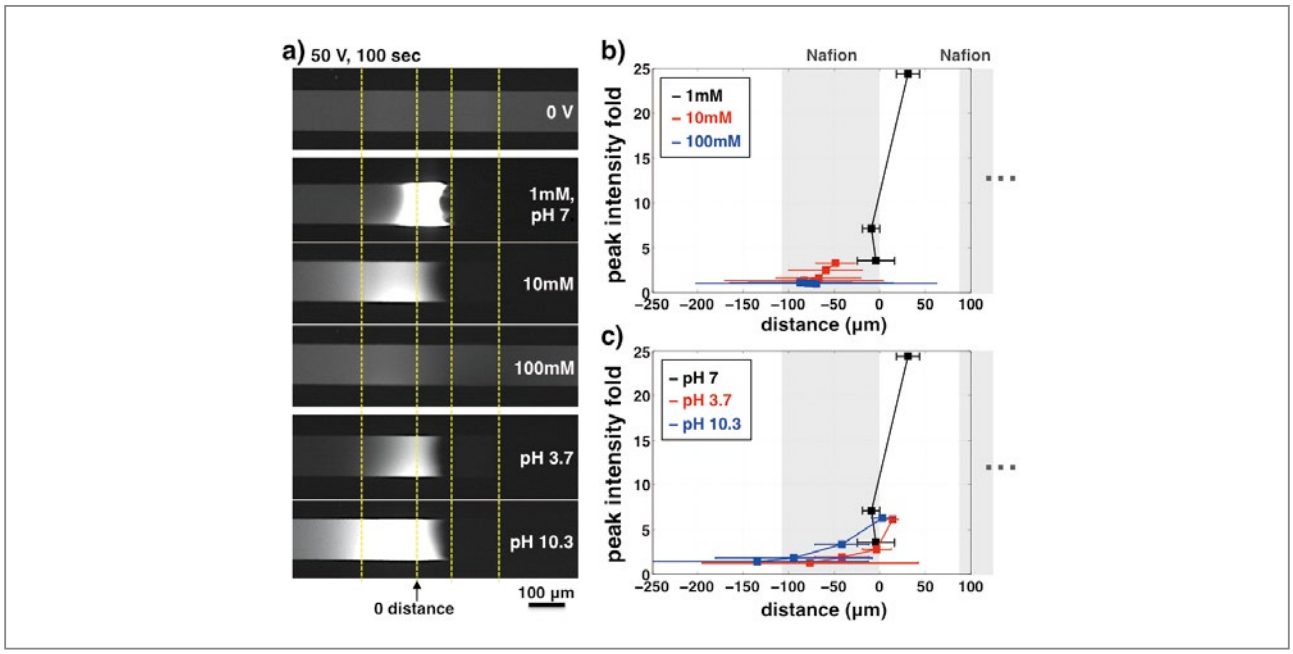

Figure 6. Spatiotemporally defined preconcentration at various ionic strengths (1-100mM NaCl) and pH values (3.7-10.3). a) Fluorescence images obtained after 100 s of operation at 50V. As can be seen, the locations of preconcentration plugs are still between two Nafion membranes (yellow dotted boxes), even though the intensity is weakened under high ionic strength and in strong acidic or basic solution. b-c) Location of peak intensity and its intensity fold (i.e., how many times over the initial intensity) are mapped under 10, 20, 50, and 100 V. 100V is not tested in 1mM NaCl (pH7), because the peak intensity already touches the highest values (due to the saturation of the CCD camera) at 50V. From the peak intensity profile (similar to that in Figure 5b), the peak region is also identified, with 1% being below the peak intensity, which is represented by error bars. In common with this, a higher voltage and stronger EOF shift the peak location to the right, with higher intensity fold and sharper preconcentration plug. Gray boxes indicate the location of Nafion membranes. The origin of the distance is the right edge of the left Nafion membrane.

micropumps [40].

Demonstration of protein preconcentration

Finally, protein preconcentration is demonstrated in this new ICP preconcentrator (Figure 7). To preconcentrate fluorescein isothiocyanate-conjugated albumin (FITC-albumin, Sigma-Aldrich, St. Louis, MO), which is a high ionic strength solution (1x phosphate buffer saline (PBS)), we used wider Nafion membranes (width: 200 μm) and a narrower channel (width: 50 μm). In this way, the ICP phenomenon can be facilitated. Wider Nafion membranes can transfer a larger portion of the cations in a smaller liquid volume between the Nafion membranes. Under 100 V, the preconcentration plug occurs in a designated region between the Nafions (white dotted box, Figure 7a) and achieves a 10,000-fold concentration of the protein in 10 min. The fluctuation in the peak fluorescence intensity is due to the perturbation of the vortices [41, 42]. However, the current maintains a constant level and represents the robust and stable operation of this platform.

Conclusion

In this article, we demonstrate a spatiotemporally defined preconcentrator by merging the ICP between two identical Nafion membranes. When the current flows through two juxtaposed membranes, the ion depletion and ion enrichment zones face each other on the anodic and cathodic sides of the Nafion membranes. If they are close enough, then two ICP zones merge and stabilize

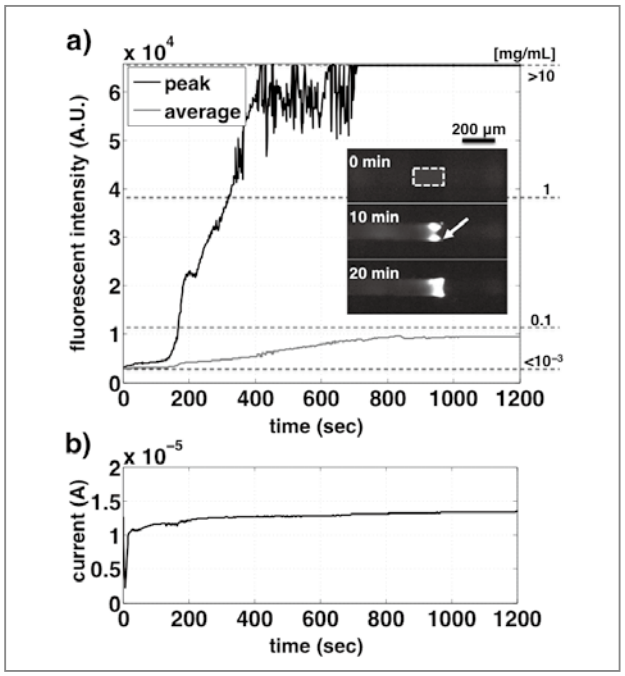

Figure 7. Demonstration of spatiotemporally fixed protein preconcentration. FITC-albumin (1 μg/mL) in 1x PBS was used. 0.1% Tween 20 was also added to prevent nonspecific binding. a) At an applied voltage of 100V, the peak and averaged fluorescence intensities are traced in the white dotted box, which is the region between Nafion membranes. Within 10 min of operation, the proteins are preconcentrated up to 10 mg/mL (peak) and ~0.1 mg/mL (averaged), indicating 10,000 and 100-fold preconcentration, respectively. The inset fluorescence images were obtained at 0, 10, 20 min. b) When the proteins were highly condensed, the current maintains a nearly constant value (10 μA).

their location even if the operating conditions, such as the voltage (0.5-100 V), ionic strength (1-100 mM), and pH (3.7-10.3), are changed. This spatiotemporally defined ICP allowed us to preconcentrate dyes and proteins up to 10,000-fold in 10 min with a pinpointed location of the preconcentration plug, i.e., between the Nafion membranes. Therefore, we no longer require the use of visualization instruments and tracers, which were previously used to specify the preconcentration site. This unique spatiotemporal controllability presents a commercial opportunity for integrating ICP preconcentrators into generic benchtop analyses such as real-time polymerase chain reactions and enzyme-linked immunosorbent assays.

Note

This article and images are drawn from "Spatiotemporally Defining Biomolecule Preconcentration by Merging Ion Concentration Polarization" in *Analytical Chemistry*, Vol. 88, P.988, 2016.

References

[1] Probstein RF. *Physicochemical Hydrodynamics: An Introduction* (Wiley-Interscience, New York, 2003), 2nd edn.

[2] Strathmann H. *Ion-exchange membrane separation processes* (Elsevier, 2004), Vol. 9.

[3] Newman J, Thomas-Alyea KE. *Electrochemical Systems* (Wiley-Interscience, New York, 2004), 3rd edn.

[4] Kwak R, Kim SJ, Han J. *Anal. Chem.* 2011; 83: 7348-7355.

[5] Jeon H, Lee H, Kang KH, Lim G. *Sci. Rep-Uk.* 2014; 4: 6668.

[6] Kim SJ, Ko SH, Kang KH, Han J. *Nat. Nanotechnol.* 2010; 5: 297-301.

[7] MacDonald BD, Gong MM, Zhang P, Sinton D. *Lab on a Chip* 2014; 14: 681-685.

[8] Schoch RB, Han JY, Renaud P. *Rev. Mod. Phys.* 2008; 80: 839-883.

[9] Kim SJ, Song YA, Han J. *Chem. Soc. Rev.* 2010; 39: 912-922.

[10] Scarff B, Escobedo C, Sinton D. *Lab on a Chip*, 2011; 11: 1102-1109.

[11] Pu QS, Yun JS, H. Temkin H, Liu SR. *Nano Lett.* 2004; 4: 1099-1103.

[12] Mai JY, Miller H, Hatch AV, *ACS Nano* 2012; 6: 10206-10215.

[13] Kim B, Heo J, Kwon HJ, Cho SJ, Han J, Kim SJ, Lim G. *ACS Nano* 2013; 7: 740-747.

[14] Wang YC, Stevens AL, Han JY. *Anal. Chem.* 2005; 77: 4293-4299.

[15] Lee JH, Cosgrove BD, Lauffenburger DA, Han J. *J. Am. Chem. Soc.* 2009; 131: 10340-+.

[16] Cheow LF, Han JY. *Anal. Chem.* 2011; 83: 7086-7093.
[17] Ko SH, Song YA, Kim SJ, Kim M, Han J, Kang KH. *Lab on a Chip* 2012; 12: 4472-4482.
[18] Phan DT, Chun Y, Nguyen NT. *RSC Adv.* 2015; 5: 44336-44341.
[19] Lee JH, Y. A. Song YA, Han JY. *Lab on a Chip* 2008; 8: 596-601.
[20] Ko SH, Kim SJ, Cheow LF, Li LD, Kang KH, Han J. *Lab on a Chip* 2011; 11: 1351-1358.
[21] Chen CH, Sarkar A, Song YA, Miller MA, Kim SJ, Griffith LG, Lauffenburger DA, Han J. *J. Am. Chem. Soc.* 2011; 133: 10368-10371.
[22] Dextras P, Payer KR, Burg TP, Shen WJ, Wang YC, Han JY, Manalis SR. *J. Microelectromech. S.* 2011; 20: 221-230.
[23] Slouka Z, Senapati S, Chang HC. *Annu. Rev. Anal. Chem.* 2014; 7: 317-335.
[24] Zangle TA, Mani A, Santiago JG. *Chem. Soc. Rev.* 2010; 39: 1014-1035.
[25] Yossifon G, Mushenheim P, Chang YC, Chang HC. *Phys. Rev. E* 2010; 81: 046301.
[26] Senapati S, Slouka Z, Shah SS, Behura SK, Shi ZG, Stack MS, Severson DW, Chang HC. *Biosens. Bioelectron.* 2014; 60: 92-100.
[27] Slouka Z, Senapati S, Shah S, Lawler, R Shi ZG, Stack MS, Chang HC. *Talanta* 2015; 145: 35-42.
[28] Sparreboom W, van den Berg A, Eijkel JCT. *Nat. Nanotechnol.* 2009; 4: 713-720.
[29] Dydek EV, Zaltzman B, Rubinstein I, Deng DS, Mani A, Bazant MZ. *Phys. Rev. Lett.* 2011; 107: 118301.
[30] Rubinstein I, Zaltzman B. *Phys. Rev. E* 2000; 62: 2238-2251.
[31] Kwak R, Pham VS, Lim KM, Han JY. *Phys. Rev. Lett.* 2013; 110: 114501.
[32] Kim SJ, Li LD, Han J. *Langmuir* 2009; 25: 7759-7765.
[33] Minerick AR, Ostafin AE, Chang HC. *Electrophoresis* 2002; 23: 2165-2173.
[34] Chambers RD, Santiago JG. *Anal. Chem.* 2009; 81: 3022-3028.
[35] Kwak R, Guan GF, Peng WK, Han JY. *Desalination* 2013; 308: 138-146.
[36] Rubinstein SM, Manukyan G, Staicu A, Rubinstein I, Zaltzman B, Lammertink RGH, Mugele F, Wessling M. *Phys. Rev. Lett.* 2008; 101: 236101.
[37] Green Y, Yossifon G. *Phys. Rev. E* 2013; 88: 049901.
[38] Kirby BJ, Hasselbrink EF. *Electrophoresis* 2004; 25: 187-202.
[39] Strathmann H. *Desalination* 2010; 264: 268-288.
[40] Wang XY, Cheng C, Wang SL, Liu SR. *Microfluid. Nanofluid.* 2009; 6: 145-162.
[41] Druzgalski CL, Andersen MB, Mani A. *Phys. Fluids* 2013; 25: 110804.
[42] Rubinstein I, Zaltzman B. *Phys. Rev. Lett.* 2015; 114: 236101.

Increase in Apoptotic Effect of Microwave-Processed Panax Ginseng in Human Prostate Cancer Cells

Pil Ju CHOI
Natural Constituents Research Center
Natural Products Research Institute
090609@kist.re.kr

Tae Jung KIM
Natural Constituents Research Center
Natural Products Research Institute
kgsing@kist.re.kr

Jung Yeob HAM
Natural Constituents Research Center
Natural Products Research Institute
ham0606@kist.re.kr

Introduction

Prostate cancer is a commonly diagnosed tumor in men that manifests along a broad spectrum of severity ranging from indolent to highly lethal [1]. Since prostate cancer cannot grow or differentiate without androgens, hormone therapy has become the standard treatment for this type of cancer [2]. However, the cancer normally recurs in subsequent years when it no longer responds to hormone therapy. At that point, chemotherapy with cytotoxic agents is suggested as an alternative growth inhibitor for hormone-refractory prostate cells [3]. Unfortunately, the effectiveness of cytotoxic agents against prostate cancer cells is often limited due to the slow proliferation of these cells [4].

Several anticancer agents which inhibit the proliferation of cancer cells, induce apoptosis, or modulate signal transductions are currently used for the treatment of prostate cancers. A combination of multiple chemopreventive agents with multiple targets is considered to be the most effective treatment strategy [5]. Herbal therapy has been suggested as a potential treatment option, partly because herbal medicines consist of several constituents with multiple targets, and partly because there is a long history of using herbal medicines in Asian and European countries [6]. Natural products have successfully contributed to the development of a large number of anticancer drugs. Approximately 50% of all anticancer drugs approved internationally are either natural products or natural product mimics and were developed

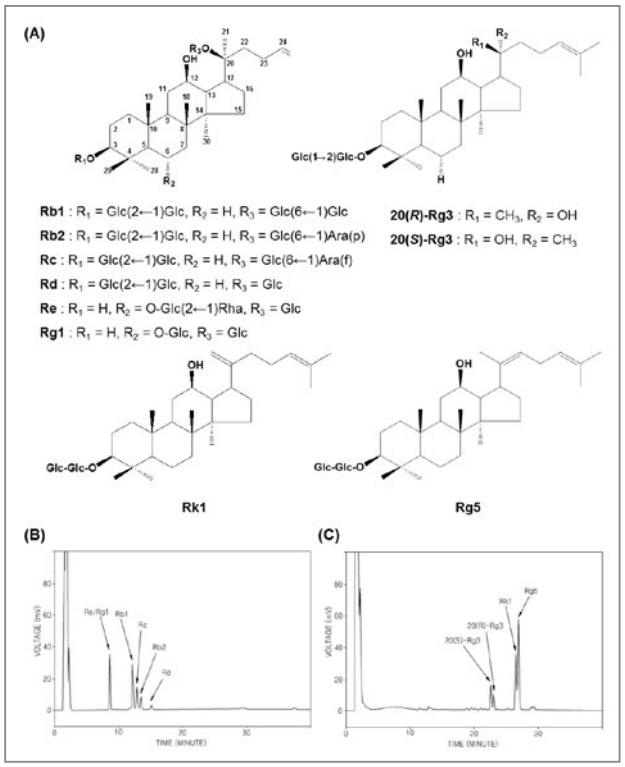

Figure 1. (A) Structures of ginsenosides contained in Panax ginseng. (B) HPLC chromatogram analyzing ginsenosides (Re/Rg1, Rb1, Rc, Rb2, and Rd) in ginseng processed by microwave. (C) HPLC chromatogram analyzing ginsenosides (20(S)-Rg3, 20(R)-Rg3, Rk1, and Rg5) in ginseng processed by microwave. -Glc: D-glucopyranosyl, -Rha: L-rhamnopyranosyl, -Ara(f): L-arabinofuranosyl, -Ara(p): L-arabinopyranosyl.

based on knowledge obtained from small molecules or macromolecules existing in nature [7].

Panax ginseng is one of the most widely used traditional herbal medicines in Asia, and a variety of commercial ginseng products such as white ginseng (moderately dehydrated by the sun), red ginseng (steamed at 95–100°C for 2–3 h), and black ginseng (subjected to steaming or enzyme fermentation) are available. Unlike other ginseng varieties, Panax ginseng contains a high concentration of saponins, including ginsenosides Rb1, Rb2, Rc, Rd, and Re (Figure 1). Research has been conducted to develop methods for increasing the pharmaceutical effect of ginseng by conversion of dammarane-based saponin into its less polar form through high temperature and high pressure thermal processing [8]. Red ginseng is a processed product of Panax ginseng obtained by steaming and drying raw ginseng. It is well known that red ginseng has different pharmacological activities compared with white ginseng, which may result from the chemical transformation of constituents during the heating process. Steaming is known to induce a structural change of ginsenoside and to enhance the biological activities of ginseng [9].

In our recent research on the diol-type ginsenosides Rb1, Rb2, Rc and Rd, the sugar moieties at carbon-20 were deglycosylated by heat-processing and gradually changed into 20(S)-Rg3, 20(R)-Rg3, Rg5 and Rk1 [10]. Depending on the position of the hydroxyl group (OH) on carbon-20 (Figure 1), ginsenosides 20(S)-Rg3 and 20(R)-Rg3 are epimers of each other, and this epimerization is known to be produced by the selective attack of the OH group after the elimination of glycosyl residue at carbon-20 during the steaming process [10, 11]. Similarly, in the case of Rk1 and Rg5, these ginsenosides are positional isomers of each other depending on the position of the double bonds on carbon-20(21) or -20(22), and this double bond is known to be produced by the elimination of H_2O at carbon-20 of Rg3 by high pressure and temperature. Regarding the processing method to increase the content of Rg3, several methods such as thermal processing with autoclave or fermentation have been suggested [10, 11]. However, no report on efficient methods to increase the amount of ginsenosides Rg5 and/or Rk1 in ginseng extract, except our own investigation [10, 12], has so far been reported.

Microwave technology has been widely used to process dielectric materials such as food products and is increasingly used in high temperature material processing applications [13]. Microwave heating is advantageous when compared to conventional heating methods since energy is introduced into the material in a volumetric way, thereby leading to a shorter processing time and a highly efficient process [14]. For this study, we developed a novel microwave-assisted heat-processing method

to maximize the content of ginsenosides Rg3, Rg5, and Rk1 in ginseng extract. Moreover, the anticancer effect and mechanism of microwave-assisted processed ginseng were evaluated in human prostate cancer cells both *in vitro* and *in vivo* (as human prostate cell (DU-145) xenografts in athymic nude mice) [12]. Our research demonstrated that ginseng processed through our microwave method inhibits prostate cancer cell growth in three human prostate cancer cell lines (DU145, LNCaP, and PC-3 cells). We further investigated the anticancer efficacy of this type of ginseng on the growth of prostate cancer cells *in vivo*.

Results and discussion

This section details the development of our method for improving the anticancer effect of ginseng by conversion of ginsenosides, the major active components of ginseng, by microwave-assisted high-temperature and high-pressure processing.

High performance liquid chromatography (HPLC) was used to examine each prepared ginseng extract, as illustrated in Figure 2 [12]. Raw ginseng showed typical ginsenosides consisting of Re, Rb1, Rc, Rb2, and Rd (Figure 2(A)). HPLC chromatograms were obtained by analyzing ginsenosides in microwave-treated ginseng (Figures 2(B) to 2(D)). During microwave processing, diol-type ginsenosides Rb1, Rb2, Rc and Rd in ginseng extract gradually changed into 20(S)-Rg3, 20(R)-Rg3, Rg5 and Rk1 through deglycosylation and dehydration at carbon-20 at a temperature of 150ºC. Also, the remaining ginsenoside of a white ginseng whose glycoside was not completely dissociated was detected between 8 min and 14 min. Contents of ginsenoside Rg3, Rk1, and Rg5 increased proportionally to microwave irradiation time as shown in Figures 2(B) to 2(D). Maximum amounts of ginsenoside Rk1 and Rg5 were generated after 60 min of microwave irradiation (Figure 3(A)). We subsequently investigated the effect of processing-

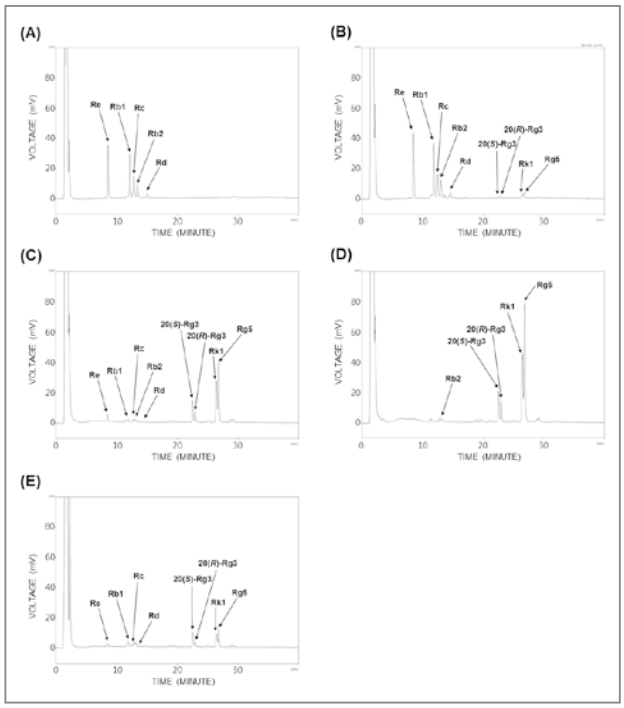

Figure 2. Comparison of ginsenoside content in ginseng extracts. HPLC chromatogram analyzing ginsenosides in: (A) white ginseng; (B) ginseng processed by microwave at a temperature of about 150°C for 10 min; (C) ginseng processed by microwave at a temperature of about 150°C for 30 min; (D) ginseng processed by microwave at a temperature of about 150°C for 60 min; and (E) ginseng processed by autoclave at a temperature of about 120°C for 180 min.

temperature on the generation of ginsenoside Rk1 and Rg5 in ginseng extract. When microwaving produced temperatures ranging from 130 to 200ºC for 30 min, the content of ginsenosides Re, Rb1, Rc, and Rb2 gradually decreased, whereas the content of ginsenoside Rg3, Rk1, and Rg5 increased (Figure 3(B)). Maximum amounts of ginsenoside Rg3, Rk1, and Rg5 were generated after microwave irradiation at 150ºC, but thermal decomposition of ginsenosides occurred after microwave irradiation at temperatures of 180 to 200ºC (Figure 3(B)). Although the amount of ginsenoside Rg5 was most abundant after microwave irradiation at 170ºC, the optimal temperature for processing is considered to be in the range of 150 to 160ºC because of the threat of

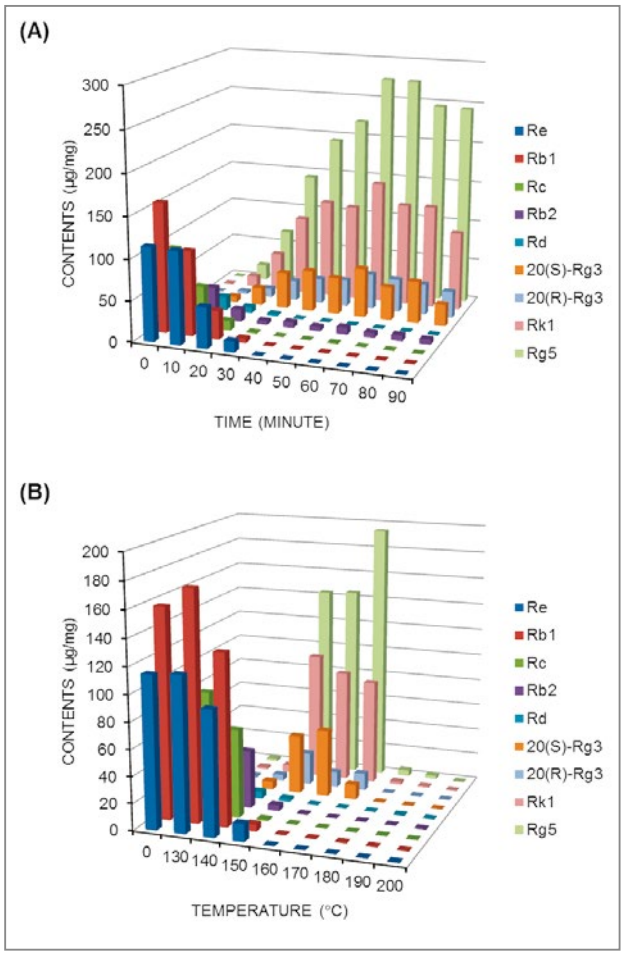

Figure 3. Comparison of the effects of treatment time and temperature on ginsenoside content in ginseng extracts. (A) Effect of treatment time on generating less polar ginsenosides after microwave assisted heat-processing of ginseng extract (μg/mg). (B) Effect of temperature on generating less polar ginsenosides after microwave assisted heat-processing of ginseng extract (μg/mg).

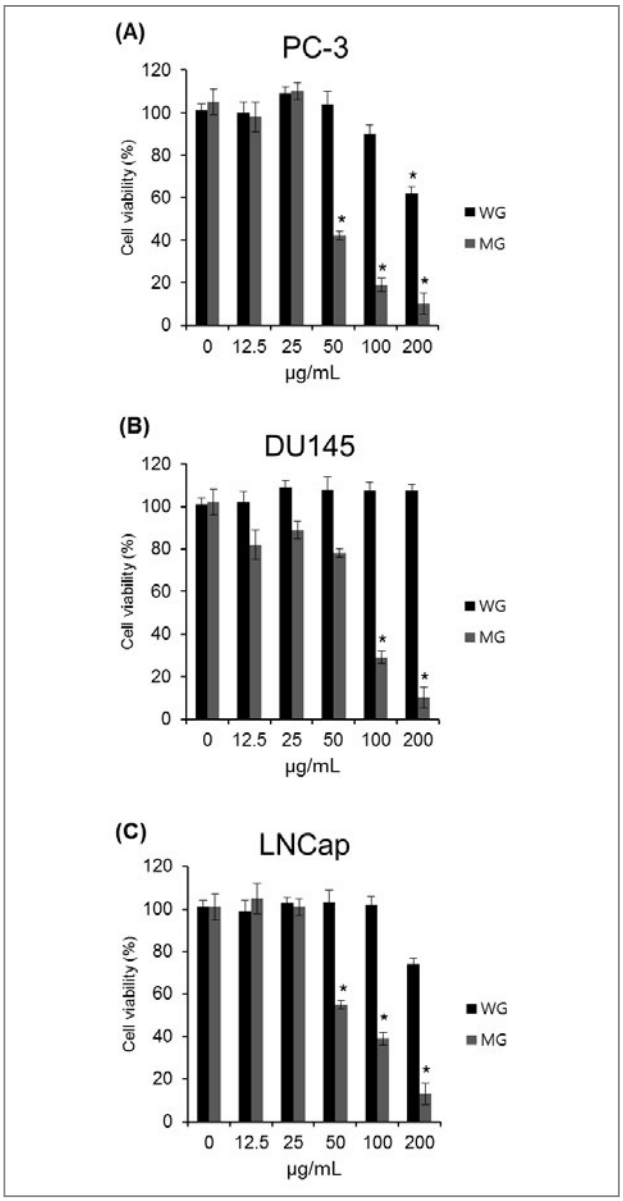

Figure 4. Comparison of the effect of ginseng extracts on the proliferation of human prostate cancer cells. (A) PC-3 prostate cancer cells were exposed to complete medium containing indicated concentrations of WG and MG (12.5-200 μg/mL) for 24 hr. (B) DU145 prostate cancer cells were exposed to complete medium containing indicated concentrations of WG and MG (12.5-200 μg/mL) for 24 hr. (C) LNCap prostate cancer cells were exposed to complete medium containing indicated concentrations of WG and MG (12.5-200 μg/mL) for 24 hr. Ez-cytox cell viability assay kit was used to determine cell viability. The data are presented as mean ± SD (*$p < 0.05$, $n = 3$).

thermal decomposition beyond those temperatures. It is important to note that the amounts of ginsenoside Rg3, Rk1, and Rg5 generated by microwave irradiation were considerably greater than those previously reported in an efficient thermal processing method by autoclave processing (Figures 2(C) to 2(E)). Based on these results, the ginseng produced by microwave processing at 150ºC for 60 min (hereinafter referred to as MG) contained the maximum content of ginsenosides Rg3, Rk1, and Rg5, and was therefore used for the evaluation of its anti-

prostate cancer effects.

To evaluate its anticancer effect, MG was tested in three human prostate cancer cell lines: DU145, LNCaP, and PC-3. MG inhibited proliferation of DU145, LNCaP, and PC-3 cells more strongly than white ginseng (WG) in a dose-dependent manner (Figure 4). The IC_{50} values were determined by interpolation from the dose–response curves. Anti-proliferation results for the three prostate cancer cell lines treated with ginseng extracts showed that MG had IC_{50} values of 48, 74, and 62 μg/mL in PC-3, DU145, and LNCap cells, respectively.

The roles of DNA damage, autophagy and apoptosis have been highly researched and reviewed for cancer prevention in ginseng research [15]. PARP, which stands for poly (ADP-ribose) polymerase, represents a family of enzymes found throughout the body that are involved in a wide range of cellular functions, including DNA repair. PARP inhibitors are currently undergoing clinical evaluation in advanced sporadic prostate cancer both as a single agent and in combination with multiple chemopreventive agents. PARP inhibitors may be the first of a generation of novel therapeutic strategies that improve or possibly avoid the use of hormone therapy to treat prostate cancer. Our study found that after treatment with 100 μg/mL of MG, the expression of PARP (cleaved PARP) increased slightly (Figure 5).

Superoxides, hydroxyl radicals, and peroxides are reactive oxygen species (ROS) that are generated during normal metabolic processes in cells. However, ROS that generate either endogenously or from external sources play a critical role in regulating several biological phenomena. The increased ROS generation not only has traditionally been associated with tissue injury or DNA damage, but also plays an essential role in several cellular processes associated with neoplastic transformation and aberrant proliferation and growth. Ginsenosides have been reported to inhibit cancer cell proliferation by inducing gene or protein expression of the cell cycle regulatory protein p21 and arresting cell cycle progression by inducing apoptosis through activation

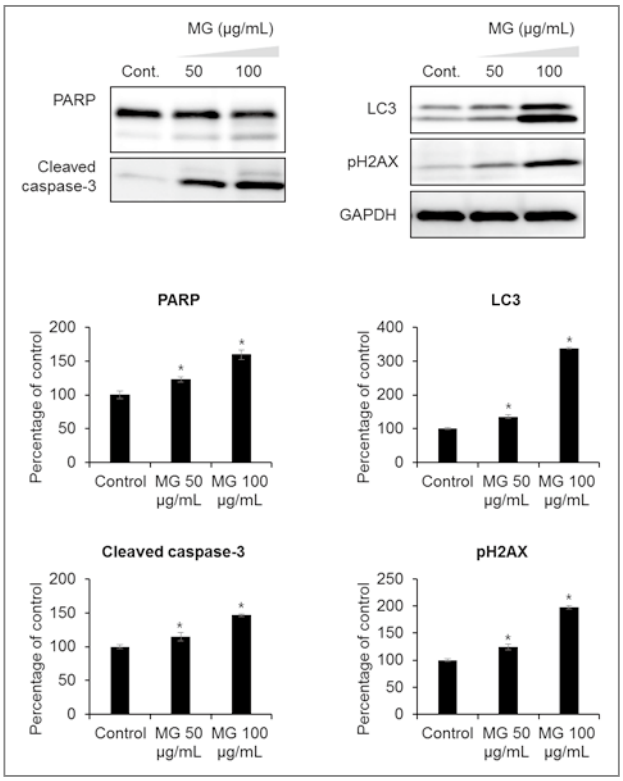

Figure 5. MG decreases the proliferation and expression of antiapoptotic proteins. PC-3 cells were exposed to vehicle (0.1% DMSO) or indicated concentrations of MG (50 and 100 μg/mL) for 24 hr. Cell lysates from each sample were used for Western blot analyses performed with antibodies directed against PARP, cleaved caspase-3, LC3 and pH2AX. GADPH was used as a loading control. The data are presented as mean ± SD (*p < 0.05, n = 3).

of caspases via a bcl-2-insensitive pathway and/or by inhibiting the mitogen-activated protein kinase signaling pathway in cancer cells [16]. In our study, co-treatment of cells with MG resulted in the activation of the inactive 32-kDa caspase-3 precursor to the cleaved p17 subunit, indicating that caspase-3 was activated during drug-induced apoptosis (Figure 5).

The pH2AX foci mark sites of double-strand DNA breaks and subsequently recruit multiple proteins involved in DNA strand break repair and damage signaling. The pH2AX is typically deactivated at the completion of proper DNA repair. In genomically unstable cells with dysfunctional DNA damage, pH2AX remains activated,

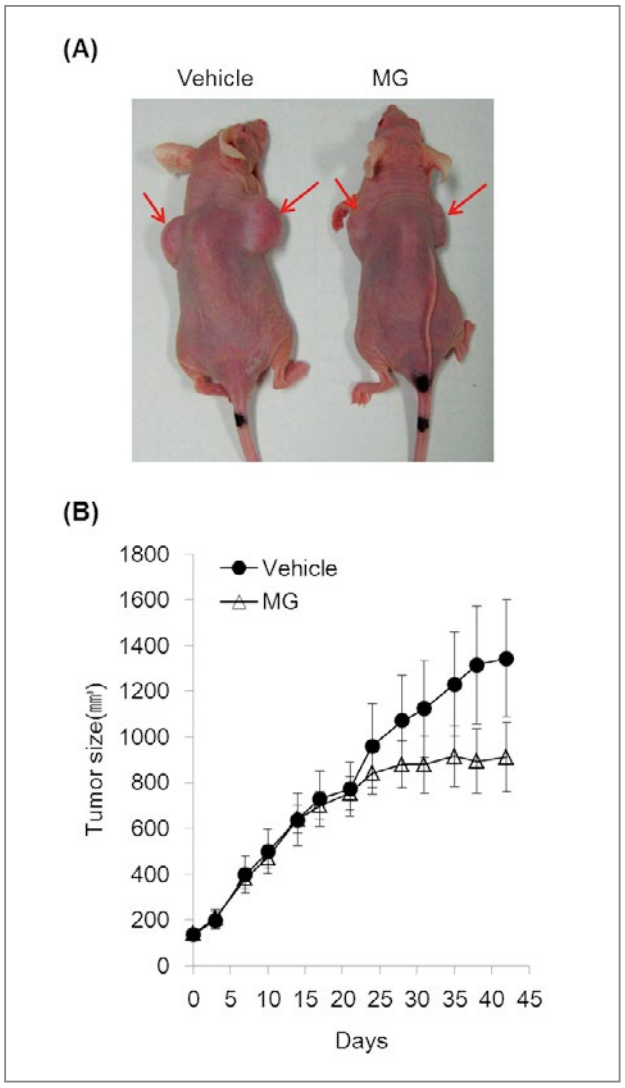

Figure 6. Effect of microwave-assisted processed ginseng on the growth of human prostate cancer DU145 cells in athymic nude mice. (A) Representative photographs of tumors in athymic nude mice. (B) Changes in tumor growth. DU145 cells (5×106 cells/100 μL PBS) were injected s.c. into the right and left flanks of the mice. Two weeks after inoculation, mice were randomly grouped according to body weight and tumor size and started on experimental diets.

and cells continue to replicate without proper DNA repair [17]. Therefore, the expression of pH2AX in PC-3 cells after MG treatment was investigated. Protein expression of pH2AX in PC-3 cells markedly increased after MG treatment in a dose-dependent manner (Figure 5).

Autophagy, a cellular process responsible for the degradation of cytoplasmic components through an autophagosomal–lysosomal pathway, has been implicated in cancer initiation and progression. Microtubule-associated protein light chain 3 (LC3) is widely used to monitor autophagosome formation. The conversion of LC3-I (18 kDa) to LC3-II (16 kDa) and its translocalization from the cytosol to autophagosomes is a reliable marker of autophagy [31]. Western blot analysis for LC3 showed a remarkable increase in LC3-II in response to MG treatment in a concentration-dependent manner (Figure 5). Thus, these results suggest that MG induces autophagic cell death as well as apoptosis in PC-3 cells.

To evaluate the anticancer effect of MG *in vivo*, we used the growth of human prostate cancer cell xenografts in athymic nude mice as a model (Figure 6). The result of *in vivo* tests shows the effect of MG on the growth of human prostate cancer DU-145 cells in athymic nude mice. A significant increase in tumor growth volume was observed during the course of and at the end of experimentation in vehicle-treated mice. However, treatment with MG significantly suppressed tumor growth over the 5-week experimental period (Figure 6(B)). These data indicate that MG suppresses prostate cancer growth *in vivo* by promoting cancer cell death, likely resulting from the increased induction of apoptosis and autophagy.

Conclusion

We have demonstrated that microwave-irradiated processed ginseng, MG, has a higher content of ginsenosides Rg3, Rg5, and Rk1, and thus a more powerful medicinal effect than ginseng processed by other methods. It was shown that MG suppressed the growth of human prostate cancer cells both *in vitro* and *in vivo*. This growth suppression by MG is associated with the inductions of apoptotic cell death and autophagy. Therefore, heat processing by microwave-assisted irradiation is a useful method to enhance the apoptotic

effect of ginseng and potentially improve prostate cancer treatment.

Note

This article and images are drawn from "Increase in apoptotic effect of Panax ginseng by microwave processing in human prostate cancer cells: *in vitro* and *in vivo* studies" in *Journal of Ginseng Research* 2016 Vol. 40, pp. 62-67 and "Improved anticancer effect of ginseng extract by microwave-assisted processing through the generation of ginsenosides Rg3, Rg5 and Rk1" in *Journal of Functional Foods* 2015 Vol. 14, pp 613-622.

References

[1] Gronberg H. *Lancet* 2003; 361: 859-864.

[2] Bidoli E, Talamini R, Bosetti C, Negri E, Maruzzi D, Montella M, Franceschi S, La Vecchia C. *Ann. Oncol.* 2005; 16: 152-157.

[3] Garnick MB, Fair WR. *Sci. Am.* 1998; 279: 74-83.

[4] Kyle E, Neckers L, Takimoto C, Curt G, Bergan R. *Mol. Pharmacol.* 1997; 51: 193-200.

[5] Hong WK, Sporn MB. *Science* 1997; 278: 1073-1077.

[6] Belaiche P, Lievoux O. *Phytother. Res.* 1991; 5: 267-269.

[7] (a) Bhanot A, Sharma R, Noolvi MN. *Int. J. Phytomedicine* 2011; 3: 9-26. (b) Newman DJ, Cragg GM. *J. Nat. Prod.* 2007; 70: 461-477. (c) Petit K, Biard JF. *Anti-Cancer Agents Med. Chem.* 2013; 13: 603-631.

[8] (a) Kang KS, Kim HY, Baek SH, Yoo HH, Park JH, Yokozawa T. *Biol. Pharm. Bull.* 2007; 30: 724-728. (b) Lee W, Park SH, Lee S, Chung BC, Song MO, Song KI, Ham J, Kim SN, Kang KS. *Food Chem.* 2012; 135: 2430-2435.

[9] Wang CZ, Zhang B, Song WX, Wang A, Ni M, Luo X, Aung HH, Xie JT, Tong R, He TC, Yuan CS. *J. Agric. Food Chem.* 2006; 54: 9936-9942.

[10] Kim YJ, Yamabe N, Choi P, Lee JW, Ham J, Kang KS. *J. Agric. Food Chem.* 2013; 61: 9185-9191.

[11] Kang KS, Kim HY, Yamabe N, Yokozawa T. *Bioorg. Med. Chem. Lett.* 2006; 16: 5028-5031.

[12] Choi P, Park JY, Kim T, Park SH, Kim H, Kang KS, Ham J. *J. Funct. Foods* 2015; 14: 613-622.

[13] Zhu J, Kuznetsov AV, Sandeep KP. *Heat Mass Transfer* 2007; 43: 255-264.

[14] Cuccurullo G, Giordano L, Viccione G. *Adv. Mech. Eng.* 2013; Article ID 929236.

[15] (a) Jang HJ, Han IH, Kim YJ, Yamabe N, Lee D, Hwang GS, Oh M, Choi KC, Kim SN, Ham J, Eom DW, Kang KS. *J. Agric. Food Chem.* 2014; 62: 2830-2836. (b) Kim AD, Kang KA, Kim HS, Kim DH, Choi YH, Lee SJ, Kim HS, Hyun JW. *Cell Death Dis.* 2013; 4: e750. (c) Kim DG, Jung KH, Lee DG, Yoon JH, Choi KS, Kwon SW, Shen HM, Morgan MJ, Hong SS, Kim YS. *Oncotarget* 2014; 5: 4438-4451. (d) Liang LD, He T, Du TW, Fan YG, Chen DS, Wang Y. *Mol. Med. Rep.* 2015; 11: 940-946. (e) Yang ZJ, Chee CE, Huang S, Sinicrope FA. *Mol. Cancer Ther.* 2011; 10: 1533-1541.

[16] Jang JH, Cho YC, Kim KH, Lee KS, Lee J, Kim DE, Park JS, Jang BC, Kim S, Kwon TK, Park JW. *Int. J. Oncol.* 2014; 45: 1680-1690.

[17] Cook PJ, Ju BG, Telese F, Wang X, Glass CK, Rosenfeld MG. *Nature* 2009; 458: 591-596.

[18] Janku F, McConkey DJ, Hong DS, Kurzrock R. *Nat. Rev. Clin. Oncol.* 2011; 8: 528-539.

Technical Review

Direct Electron Transfer of Enzymes in a Biologically Assembled Conductive Nanomesh Enzyme Platform

Hyun Jung YI
Center for Spintronics, Post-Silicon Semiconductor Institute
hjungyi@kist.re.kr

Introduction

The direct-electron-transfer (DET) process in biological systems [1] has been actively investigated in the fields of photosynthesis [2], biofuel cells [3], biomass degradation [4], bioelectronic devices [5] and biosensors [6]. Since biosensors based on the DET of redox biomolecules or enzymes [7] do not require toxic chemical mediators for electron transfer and can operate in the negative potential range without interfering with background chemicals, they provide an ideal solution for the challenges involved in the development of wearable items such as contact lenses [8, 9], patches [10], and tattoos [11] that also function as monitoring systems for healthcare, sports, and defense applications.

Intimate electrical coupling of enzymes with nanostructured electrodes showing excellent electrochemical conductance is of paramount importance for the highly efficient DET of enzymes. Various nanomaterials such as metallic nanoparticles (NPs) [12], carbon nanotubes (CNTs) [13], graphene and reduced graphene oxides [14], inorganic ultrathin layers [15], and conducting polymers [16] have been explored in attempts to improve the efficiency of the DET process. For facile processing of these nanoscale electronic materials in solution and/or for covalent conjugation of enzymes onto the electronic materials, destructive processes such as chemical treatment or surface modification of nanoscale electronic materials have been widely employed. However, destructive processes can cause

deterioration of the electrical properties of electronic materials and lead to poor electrical contact between enzyme-conjugated nanoscale electronic materials, thereby limiting the efficiency and applicability of the DET of enzymes.

The focus of this article is on KIST's efforts in designing a non-destructive assembly approach for constructing a nanostructured enzyme platform for the highly facilitated and versatile DET of enzymes. We show that a nanostructured enzyme platform assembled by combining specific biomolecular attraction and electrostatic coupling using a biological template material enables highly facilitated DET of enzymes with exceptional applicability and unprecedented versatility. Using our approach, we not only demonstrate highly facilitated DET in flexible integrated devices but also achieve DET for eight different enzymes with various types of catalytic activities.

Results and discussion

Figure 1 schematically illustrates the assembly process of the nanostructured conductive electrode platform, a nanomesh. A conductive nanomesh of nanoscale-electrical wires, single-walled carbon nanotubes (SWNTs), is assembled under a hydrodynamic process (Figure 1a) in the presence of a specific M13 clone with strong binding affinity toward SWNTs on its body surface [17]. The M13 phage, a biological template material, controls and stabilizes the nanostructure of the nanomesh in a non-destructive manner *via* biomolecular interaction in the concentration polarization region [17, 18]. The assembled conductive nanomesh is easily made free-standing by removal of the dialysis membrane; it remains stable owing to the biological glue effect of the M13 (Figure 1b).

For the fabrication of the enzyme platform, the freestanding nanomesh is then transferred onto metal-deposited substrates such as Au-coated screen-printed

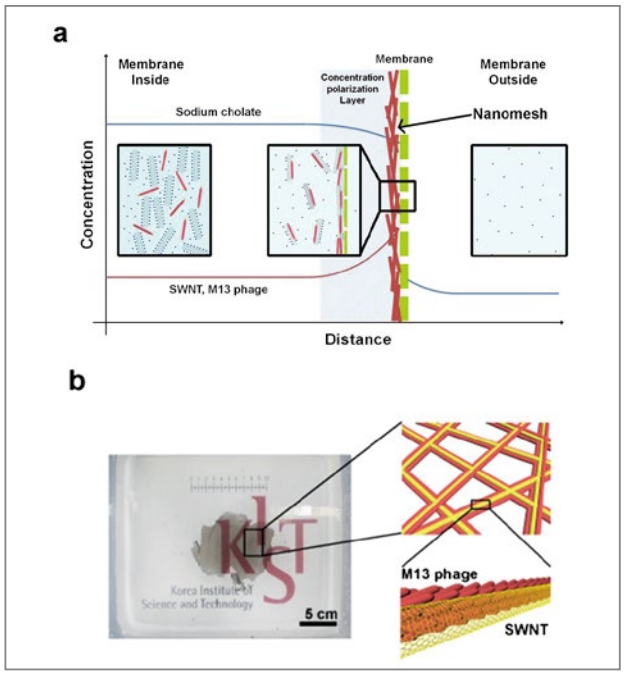

Figure 1. a) Schematic illustration of the hydrodynamic assembly of a conductive nanomesh of SWNTs using the biomolecular attraction of a genetically engineered M13 phage with its body surface expressing strong binding affinity toward SWNTs. The M13 phage binds SWNTs preferentially in the concentration polarization region, after which the M13 phage-SWNTs are assembled into a conductive nanomesh. b) A photograph of the freestanding nanomesh floating on DI water and the schematic binding scheme of SWNTs and M13 phage in the nanomesh.

electrodes using pre-patterned stencil masks, as shown in Figure 2. Once dried and adhered onto the substrates, the nanomesh remains robust during subsequent processes and continuous operation in biological solutions. In order to non-destructively and intimately couple negatively charged enzymes (pI<7.2), a monolayer of positively charged polyelectrolyte interlayer is formed on the negatively charged conductive nanomesh, after which enzymes are immobilized. For positively charged enzymes (pI>7.2), negatively charged polyelectrolyte layer can be additionally formed.

The microstructures of the enzyme-free nanomesh (SWNT-M13 nanomesh) and the enzyme-nanomesh layer (GOx/PEI/SWNT-M13 nanomesh) are shown in Figure 3. Enzymes are homogeneously distributed throughout the networks without any obvious clumps. The GOx

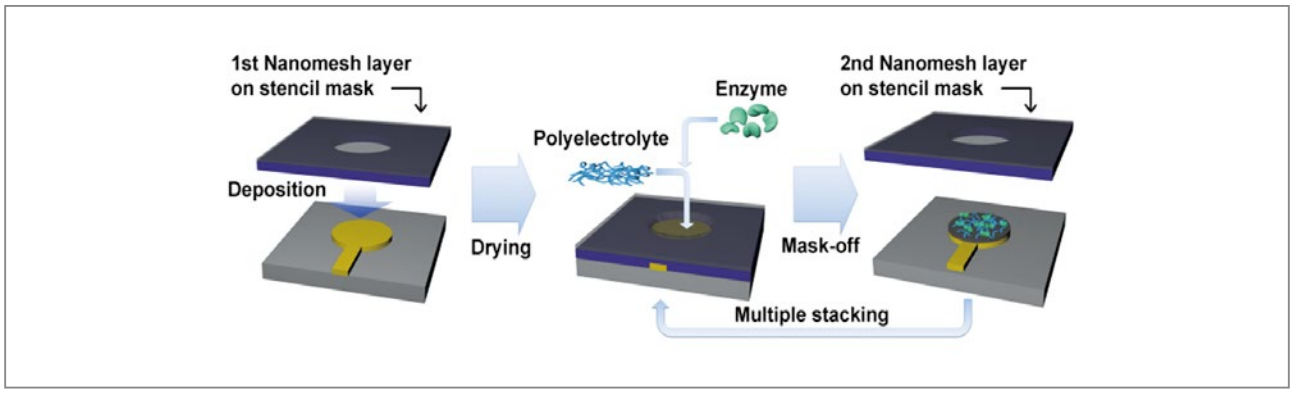

Figure 2. The fabrication process of the nanomesh enzyme platform for the DET of enzymes. Enzymes are electrostatically coupled via polyelectrolyte interlayers onto the naturally negatively charged hybrid nanomesh. Multiple stacking of the layered nanomesh is also illustrated.

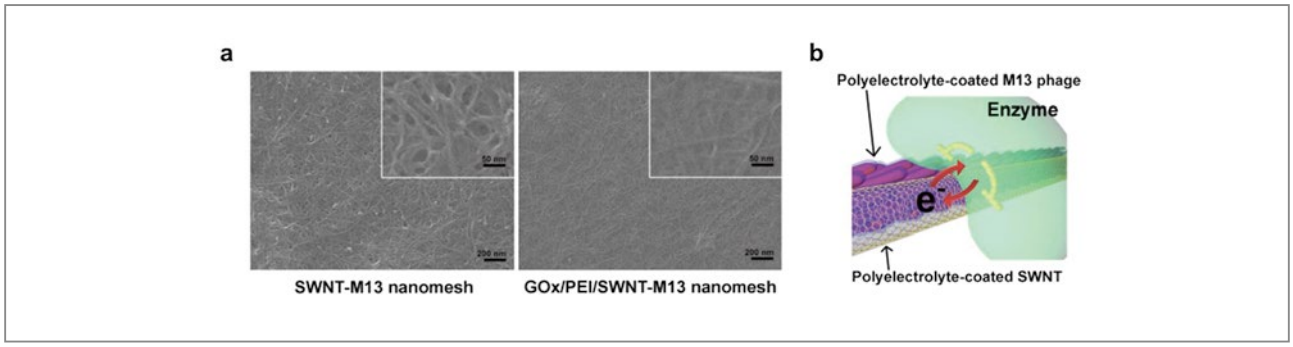

Figure 3. a) Scanning electron micrographs of the enzyme-free nanomesh (SWNT-M13 nanomesh) and the nanomesh-enzyme platform (GOx/PEI/SWNT-M13 nanomesh). Inset shows the magnified micrographs. b) Schematic illustration of the DET of enzymes in the biologically assembled conductive nanomesh enzyme platform.

enzymes immobilized on the nanomesh showed only a slight conformational change, and thereby retained high catalytic activities as demonstrated below. This totally non-destructive nature of our assembly approach can preserve the high conductivity of the SWNTs and the integrity of the biological molecules. Furthermore, our approach provides several other important features for DET-based biosensors. First, it provides a versatile platform since the assembly is not limited to specific types of enzymes. Second, the enzyme-nanomesh layer can be multilayered for tunable sensitivity. Third, it may enable DET-based flexible integrated biosensors since the freestanding conductive nanomesh can be patterned using a stencil mask.

Characteristics of the DET of enzymes in the biologically assembled conductive nanomesh enzyme platform were investigated using glucose oxidase (GOx) as a model enzyme system. Glucose biosensors have served as models for decades, and the efficient DET of GOx has been considered one of the most promising solutions for next-generation glucose biosensors [7]. Figure 4 shows the cyclic voltammograms (CVs) of the nanomesh-GOx layer on Au (GOx/PEI/nanomesh/Au) and of GOx on bare Au substrate (GOx/PEI/Au). The nanomesh-GOx layer clearly produced strong DET redox peaks at -380 mV vs. Ag/AgCl (the red curve in Figure 4). These strong faradic peaks at -380 mV arise from the FAD/$FADH_2$ redox couples [19], a redox cofactor of GOx.

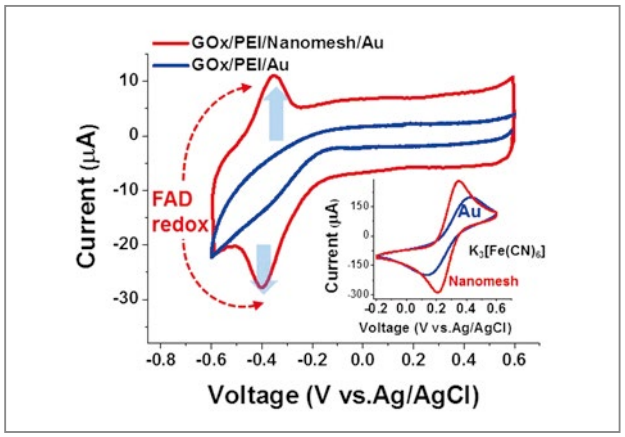

Figure 4. The effect of the nanomesh on the DET of GOx. CVs of nanomesh-GOx (GOx/PEI/Nanomesh/Au) and of the GOx on a bare Au substrate (control sample, GOx/PEI/Au). Only the nanomesh-GOx layer shows peaks at ~ -400 mV, which arise from the direct transfer of electrons from/to the enzyme. Inset: CVs of the nanomesh on an Au substrate and of a bare Au substrate in 10 mM $K_3Fe(CN)_6$ in 10 mM PBS buffer.

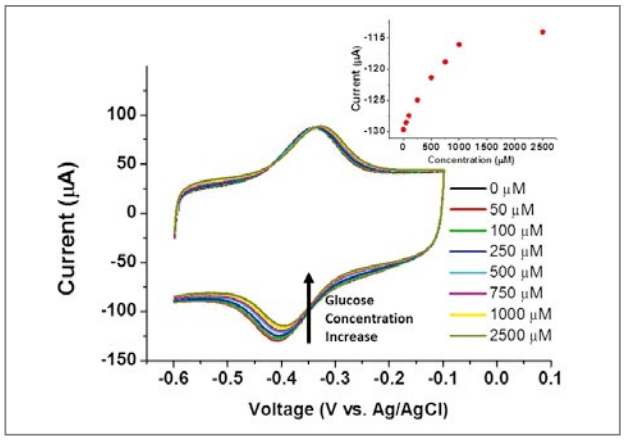

Figure 5. Dependence of the DET of GOx on glucose concentration. CVs of the nanomesh-GOx (100 mg/ml GOx/PEI/nanomesh)$_2$/Au) at different glucose concentrations are shown. Inset: dependence of the reduction current on the glucose concentration. As the glucose concentration increased, the reduction current decreased by a linear relationship. All the CVs were scanned at a rate of 200 mV/s.

The electro-catalytic reaction of FAD/$FADH_2$ is shown in Equation (1):

$$GOx\ (FAD) + 2H^+ + 2e^- \leftrightarrow GOx\ (FADH_2) \quad (1)$$

The voltage separation of cathodic and anodic peaks, ΔE_p, is ~25 mV, indicating that the reactions of FAD/$FADH_2$ redox pairs of GOx were reversible and GOx was electrically well-addressed. In contrast, the GOx immobilized on the bare Au electrode did not yield any obvious DET peaks at the negative potential window (the blue curve in Figure 4), highlighting the critical role of the conductive nanomesh for the highly facilitated DET of enzymes. The effect of the nanomesh on the improved electron-transfer was also confirmed using a standard chemical redox molecule, $K_4[Fe(CN)_6]$, as shown in the inset of Figure 4. The nanomesh on the Au substrate reduced the quasi-reversible redox potential of $[Fe(CN)_6]^{3-/4-}$ by ~ 100 mV and increased both the anodic and cathodic peak currents by ~ 40% compared to the bare Au substrate (Figure 4). Moreover, electrochemical impedance spectroscopy (EIS) analysis revealed that the charge transfer resistance (R_{ct}) was reduced by 83% (not shown here).

The glucose sensing characteristics of the nanomesh-GOx was also investigated. Figure 5 shows CVs of the nanomesh-GOx upon addition of glucose. The sensing mechanism of this DET-based glucose sensor can be explained by the following Equation (2):

$$GOx\ (FAD) + Glucose \rightarrow GOx\ (FADH_2) + Gluconolactone \quad (2)$$

Adding glucose into the electrolyte solution promoted the enzyme-catalyzed reaction between GOx (FAD) and glucose and resulted in an increase in the concentration of the reduced form of GOx, i.e., GOx ($FADH_2$). As a result, the reduction peak current of DET decreased (i.e., less reduction) due to the decrease in the concentration of the oxidized form of GOx, i.e., GOx (FAD). On the other hand, the addition of 1 mM of an interfering material such as ascorbic acid (AA) and uric acid (UA) did not significantly alter the DET peaks of GOx (blue curve in Figure 6). Moreover, the DET peak currents measured in human serum and artificial tear solution differed only by ~4% from the peaks in PBS buffer solution (not shown here). These results confirm the importance and advantages of DET operating at the negative potential

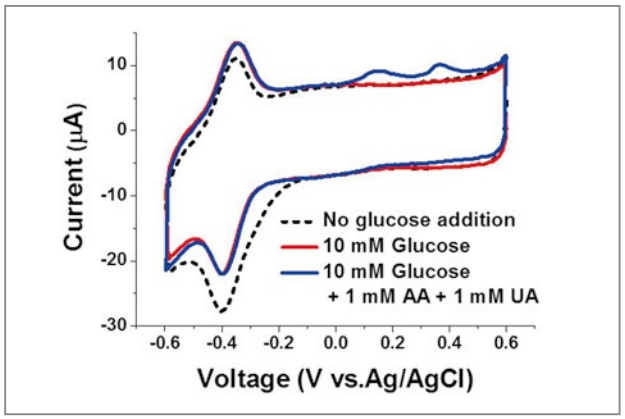

Figure 6. High selectivity of the DET-based glucose sensors. The effects of the addition of the substrate of GOx, i.e., glucose, and the interfering chemicals AA and UA on the DET of GOx are shown.

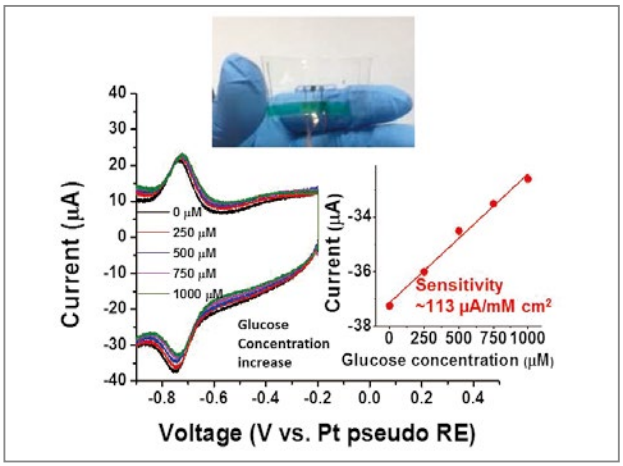

Figure 7. Flexible DET-based glucose biosensor. Top inset: photograph of a representative PDMS-based flexible biosensor. Bottom inset: dependence of the reduction current of the flexible nanomesh-GOx biosensor on glucose concentration.

ranges for biosensor applications.

Next, the possibility of fabricating flexible DET-based biosensors was investigated. Flexible biosensors were fabricated on a 0.5 mm-thick PDMS film. Figure 7 shows the CVs of the flexible glucose biosensor based on the nanomesh-GOx enzyme platform. DET peaks of GOx are clearly shown, being shifted by -315 mV due to the use of Pt pseudo-reference electrode (PRE) instead of Ag/AgCl. The performance of the biosensors under bending conditions was tested by fixing the device on a polyimide (PI) substrate and mounting on a programmable syringe pump. The peak currents and potential ranges of the DET did not significantly change upon bending the biosensor by 50° (not shown here), implying that the efficiency of the DET processes of GOx on the nanomesh was preserved. To the best of our knowledge, this work demonstrates a flexible DET-based glucose biosensor for the first time. Importantly, the sensitivity measured on the flexible fluidic device, 113 μA/mM-cm^2, is comparable to the values obtained using nanomeshes on a commercialized screen-printed electrode substrate. Moreover, the LOD was 35 μM, which is far lower than 150 μM, the concentration of glucose in tears [8]. Since the glucose level in tears has been reported to have a correlation with the blood glucose level [8], our work could provide a promising bio-sensing platform for noninvasive monitoring of the blood glucose level. These results suggest that our approach holds great promise for the development of biosensors with high selectivity, sensitivity, safety, and mechanical flexibility.

In addition to the advantages of DET such as non-fouling and non-toxicity, realizing DET with several types of enzymes can benefit the monitoring of various disease-related biomarkers. Since our assembly approach is generic in nature, we further investigated the possibility of efficient DET of seven other types of enzymes and catalytic activities, that is, cholesterol oxidase (CholOx), lactate oxidase (LOx), horseradish peroxidase (HRP), catalase, galactose oxidase (GalOx), tyrosinase, and laccase. These enzymes, when including GOx, can be categorized into three groups based on the types of redox centers they contain [20-24]. The three redox centers include those containing an FAD, heme, and copper. The categories and the tested results are shown in Table 1.

Conclusion

We have developed a biological template material-based assembly scheme for greatly facilitated DET of

Table 1. List of the tested enzymes and associated features including measures of the DET of these enzymes in the conductive nanomesh enzyme platform.

Redox center		Enzyme	Substrate	Clinical diagnosis	Normal Substrate Concentration	Sensitivity (DET potential vs. Ag/AgCl)	Linear range
FAD		Glucose oxidase (GOx)	Glucose	Diabetes	~ 5 mM in blood ~100 μM in tears	107 μA/mM cm^2 (-380 mV)	0.05 - 1 mM
FAD		Cholesterol oxidase (CholOx)	Cholesterol	Hypertension Kidney failure Chronic hepatitis Heart attack Depression Anxiety	2.2 - 5.2 mM for adults (The level in saliva is 4 x lower than in human serum)	28 μA/mM cm^2 (-350 mV)	0.01 - 1 mM
FAD		Lactate oxidase (LOx)	Lactate	Lactic acidosis Heart failure Hypoxia	0.3 - 1.3 mM in venous blood 0.3 - 0.8 mM in arterial blood	143 μA/mM cm^2 (-350 mV)	0.01 - 0.5 mM
Heme		Horesradish peroxidase (HRP)	H_2O_2	Oxidative stress	less than 0.05 mM	230 μA/mM cm^2 (-300 mV)	0.01 - 7.5 mM
Heme		Catalase				334 μA/mM cm^2 (-360 mV)	0.01 - 5 mM
Cu	T2	Galactose oxidase (GalOx)	Galactose	Galactosemia	0.5 - 1 mM	40 μA/mM cm^2 (-350 mV)	0.05 - 1 mM
Cu	T3	Tyrosinase	Catechol/ Catechol amine	Schizophrenia Attention deficiency Alzheimer's disease Parkinson's disease Epilepsy	-	326 μA/mM cm^2 (-350 mV)	0.01 - 1 mM
Cu	T2/3	Laccase				541 μA/mM cm^2 (-270 mV)	0.01 - 1 mM

enzymes with unprecedented applicability and versatility. The non-destructive assembly of a nanostructured enzyme platform which combines specific biomolecular attraction and electrostatic coupling using a biological template material enabled DET-based flexible biosensors and DET for eight different enzymes with various types of catalytic activities. We envision that this work will not only enable the development of high-performance wearable health-monitoring devices but also benefit other research fields involving the DET of biomolecules, such as artificial photosynthesis, biofuel cells, and bio-mechanistic studies.

Note

This article and images have been drawn from "Direct electron transfer of enzymes in a biologically assembled conductive nanomesh enzyme platform" in *Adv. Mater.* (2016) Vol. 28, pp. 1577-1584.

References

[1] Moser CC, Keske JM, Warncke K, Farid RS, Dutton PL. *Nature* 1992; 355: 796-802.

[2] Yacoby I, Pochekailov S, Toporik H, Ghirardi ML, King PW, Zhang S. *Proceedings of the National Academy of Sciences* 2011; 108: 9396-9401.

[3] Zebda A, Gondran C, Le Goff A, Holzinger M, Cinquin P, Cosnier S. *Nat. Commun.* 2011; 2: 370.

[4] Liu W, Mu W, Liu MJ, Zhang XD, Cai HL, Deng YL. *Nat. Commun.* 2014; 5: 3208.

[5] Lee EH, Lee SW, Saraf RF. *ACS Nano* 2014; 8: 780-786.

[6] Shan D, Zhang J, Xue HG, Ding SN, Cosnier S. *Biosens. Bioelectron.* 2010; 25: 1427-1433.

[7] Wang J. *Electroanalsis* 2001; 13: 983-988.

[8] Chu MX, Miyajima K, Takahashi D, Arakawa T, Sano K, Sawada S, Kudo H, Iwasaki Y, Akiyoshi K, Mochizuki M, Mitsubayashi K. *Talanta* 2011; 83: 960-965.

[9] Yao HF, Shum AJ, Cowan M, Lahdesmaki I, Parviz BA. *Biosens. Bioelectron.* 2011; 26: 3290-3296.

[10] Guinovart T, Valdés-Ramírez G, Windmiller JR, Andrade FJ, Wang J. *Electroanalysis* 2014; 26: 1345-1353.

[11] Jia WZ, Bandodkar AJ, Valdes-Ramirez G, Windmiller JR, Yang ZJ, Ramirez J, Chan G, Wang J. *Anal. Chem.* 2013; 85: 6553-6560.

[12] Liu GD, Lin YH, Ostatna V, Wang J. *Chem. Commun.* 2005; 3481-3483.

[13] Zhang X, Liu D, Li L, You T. *Sci. Rep.* 2015; 5: 9885.

[14] Razmi H, Mohammad-Rezaei R. *Biosens. Bioelectron.* 2013; 41: 498-504.

[15] Liu JQ, Paddon-Row MN, Gooding JJ. *J. Phys. Chem. B* 2004; 108: 8460-8466.

[16] Wang ZY, Liu SN, Wu P, Cai CX. *Anal. Chem.* 2009; 81: 1638-1645.

[17] Lee KY, Byeon HH, Jang C, Choi JH, Choi IS, Jung Y, Kim W, Chang J, Yi H. *Advanced Materials* 2014; 27:922-928.

[18] Ju S, Lee KY, Min SJ, Yoo YK, Hwang KS, Kim SK, Yi H. *Sci. Rep.* 2015; 5: 9196.

[19] Deng C, Chen J, Nie Z, Si S. *Biosens. Bioelectron.* 2010; 26: 213-219.

[20] S.-Q. Liu, H.-X. Ju, Anal. Biochem. 2002; 307: 110-116.

[21] Shleev S, Tkac J, Christenson A, Ruzgas T, Yaropolov AI, Whittaker JW, Gorton L. *Biosens. Bioelectron.* 2005; 20: 2517-2554.

[22] Wright C, Sykes AG. *J. of Inorg. Biochem.* 2001; 85: 237-243.

[23] Lee SW, Lopez J, Saraf RF. *Electroanal.* 2013; 25: 1557-1566.

[24] Lunsford SK. *ECS Trans.* 2006; 3:13-19.

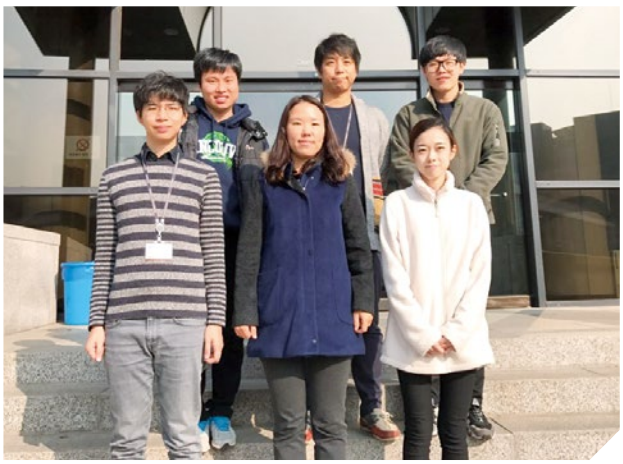

Feature Articles

Electrically-Excited Spin Wave Reveals Interfacial Dzyaloshinskii-Moriya Interaction

Jong Min LEE
Center for Spintronics, Post-Silicon Semiconductor Institute
jongmin.lee0311@gmail.com

Byoung Chul MIN
Center for Spintronics, Post-Silicon Semiconductor Institute
min@kist.re.kr

Introduction

Magnetic order in ferromagnetic materials originates mainly from the Heisenberg exchange interaction which is symmetric with respect to the inversion of a system. When the inversion symmetry is broken in a ferromagnetic system with strong spin-orbit coupling, there exists a non-negligible anti-symmetric exchange interaction, namely, the Dzyaloshinskii-Moriya interaction (DMI) [1, 2]. The DMI represents an important topic in spintronics research, since the presence of DMI in a magnetic system leads to the stabilization of chiral spin textures such as skyrmion and provides an efficient manipulation of magnetic nanostructures [3-5]. The DMI is observed not only in bulk materials (e.g., B20 materials such as MnSi and FeGe), but also in magnetic nanostructures where the inversion symmetry is broken at the interfaces with strong spin-orbit coupling (e.g., Pt/CoFeB/MgO) [6-13]. In order to understand the effect of interfacial DMI (*i*-DMI) in such systems, it is important to measure the sign and magnitude of interfacial DMI.

Spin wave provides a unique tool to study the DMI [14-17]. While several research groups have employed Brillouin light spectroscopy (BLS) to study such effects [18-22], it has been difficult to realize an all-electrical measurement of interfacial DMI using collective spin-wave dynamics. An electrical method is relatively free from the possible constraints and artifacts caused by nonlinear interaction of thermal magnons having various wave

vectors, which might be critical for BLS investigation.

Spin wave spectroscopy

Propagating spin wave spectroscopy [23] is employed to study the effect of interfacial DMI on the electrically-excited spin wave in ferromagnet/nonmagnet nanostructures. In the magnetostatic surface wave (MSSW) or Damon-Eshbach (DE) mode [24], where the magnetization polarity (p) is perpendicular to the spin wave vector (k), the k and p determine the spatial chirality of spin alignment (see Figure 1). This is because, given the propagation direction, the direction of magnetization determines the orientation of spin precession and thereby the spin chirality. For instance, when the magnetization is along the $+y$-axis, the spin wave propagating with wave vector $+k$ ($-k$) has a counter-clockwise (clockwise) rotation of spins (see Figure 1a). The presence of i-DMI could lift the degeneracy in the spin wave frequency (f), resulting in asymmetric frequency response with respect to k [16, 17].

In order to measure the effect of i-DMI on the spin wave frequency, we prepared ferromagnetic film structures consisting of substrate/Ta (3 nm)/Pt (3 nm)/Co (t nm)/MgO (1.8 nm)/Ta (3 nm), hereafter referred to as the Pt/Co (t)/MgO samples. The film stacks were grown on oxidized silicon substrates by magnetron sputtering and patterned into an 8-μm-wide strip; thereafter, a 40-nm-thick AlO_x layer was deposited on the strip for electrical insulation. On top of the ferromagnet (FM) strip and AlO_x insulation, a pair of meander-shaped antennae (see Figure 1b) were formed by a lift-off of Ti (5 nm)/ Au (150 nm). The spatial period of the meander lines determined the k of spin wave. The first antenna connected to a microwave source generated a spatially-periodic magnetic field, which in turn, excited spin waves in the FM strip with a well-defined wave vector k; and the second antenna located at the other end detected the propagated spin waves inductively. With interchanging the injector and detector antenna, we could manipulate the propagating direction of the spin waves. During the measurement, a static magnetic field was applied in the transverse direction (y direction) to secure the MSSW mode.

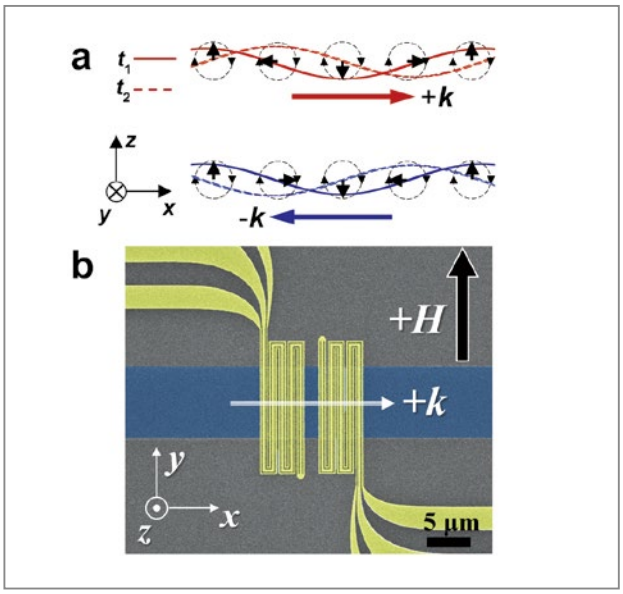

Figure 1. Spin configuration and measurement geometry for propagating spin wave spectroscopy. (a) Schematic diagram of counter-clockwise (clockwise) spin alignment of the spin wave propagating with $+k$ ($-k$) taken at time t_1 and t_2 ($t_2 > t_1$). (b) Scanning electron micrograph image of the measurement geometry showing ferromagnet strip (blue) for the spin wave propagation in the longitudinal (x) direction and meander-line antennae (yellow) for the spin wave injection and detection. External magnetic field (H) is applied in the transverse (y) direction.

Results

The imaginary part of mutual inductance, $Im(DL_{ij})$, displays an absorption of spin waves at the detecting antenna as a consequence of spin wave resonance. Figure 2 shows an example of the measured $Im(DL_{ij})$ of an Pt/Co (20)/MgO sample when the spatial period of antenna is 800 nm (k = 7.85 μm^{-1}) and the applied transverse field (H) is +500 Oe. The DL_{21} (red line) and DL_{12} (blue line) correspond, respectively, to the spin wave propagating

in the forward (from the left to the right antenna) and the reverse (from the right to the left antenna) directions. We check whether the asymmetry in the frequency response agrees with what has been predicted in the presence of *i*-DMI [16, 17]. When a positive transverse field (H = +500 Oe) is applied, the forward-going (reverse-going) spin wave has a counter-clockwise (clockwise) spin chirality; the forward-going (+k) spin wave shows a signal maximum at 15.48 ±0.01 GHz whereas the reverse-going (–k) spin wave shows a signal maximum at 15.32 ±0.01 GHz. A substantial frequency difference ($Df = f(+k) - f(-k)$ = +160 MHz) between two maxima is observed with respect to the change of propagation direction. When the sign of transverse field (p) is reversed (see Figure 2b), the forward-going spin wave (+k) shows a peak at a lower frequency in comparison with reverse-going spin wave (–k). The frequency difference (($Df = f(+k) - f(-k)$ = -160 MHz) in this case has the opposite sign, and the magnitude of Δf is the same as the previous case. Various combinations of k and p show that the counter-clockwise chiral alignment results in a higher spin wave frequency than the clockwise alignment in this system. This is exactly what is predicted by the theory [16, 17].

An important question is how this frequency shift is related to *i*-DMI. A precise estimation of *i*-DMI requires a delicate consideration to distinguish the pure contribution of *i*-DMI from other sources such as the non-reciprocity of MSSW mode and the influence of interfacial magnetic anisotropy [20]. We should take into account that the propagating spin wave is partially localized on either the top or bottom interface of the ferromagnetic layer depending on the propagation direction. Hence, if the top interface has a substantially different interface anisotropy in comparison with that of the bottom interface, this may result in a frequency shift (Δf_{ks}) with respect to the sign change of k or p. Therefore, the measured frequency difference (Δf) could be a sum of both the Δf_{DMI} from *i*-DMI and Δf_{ks} from the interfacial anisotropy difference. After subtracting the contribution from other sources to the frequency shift, it is possible to quantify the DMI energy in Pt/Co/MgO systems.

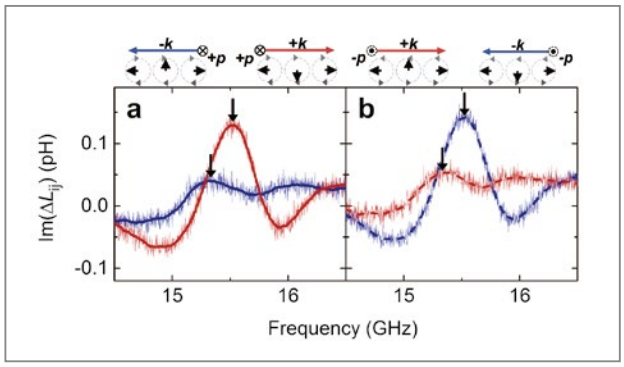

Figure 2. Asymmetric spin wave propagation in the Pt/Co(20)/MgO sample. The imaginary part of mutual inductances, $Im(DL_{ij})$, displaying the absorption of spin waves at the detecting antenna as a consequence of spin wave resonance (k = 7.85 μm^{-1} and H = 500 Oe). (a) Frequency response of spin wave with –k, +p (blue solid line) and with +k, +p (red solid line). (b) Frequency response of spin wave with -k, -p (blue dashed line) and with +k, -p (red dashed line). Schematic diagrams of spin alignment are shown for each combination of k and p.

The measurement of DMI as a function of Co thickness (see Figure 3) provides important insights on the nature of the DMI in Pt/Co (t)/MgO structures. The measured DMI of Pt/Co (t)/MgO samples is proportional to 1/t, displaying the interfacial origin of the DMI. The sign of *i*-DMI is positive in the Pt/Co (t)/MgO samples, meaning that the clockwise spin alignment is energetically more stable than the counter-clockwise spin alignment in this system. In order to investigate whether the sign of *i*-DMI corresponds to the inversion asymmetry of the film structures, we prepare inverted structures consisting of substrate/Ta (3 nm)/MgO (1.8 nm)/Co (t nm)/Pt (3 nm)/Ta (3 nm) referred to as MgO/Co (t)/Pt samples, and a symmetric structure consisting of substrate/Ta (3 nm)/MgO (1.8 nm)/Co (20 nm)/MgO (1.8 nm)/Ta (3 nm) referred to as an MgO/Co/MgO sample.

Figure 3b shows the measured $Im(DL_{ij})$ of three different samples when a spatial period of antenna is 800 nm (k = 7.85 μm^{-1}) and a transverse field (H) is +500 Oe. The inverted MgO/Co/Pt samples (bottom panel)

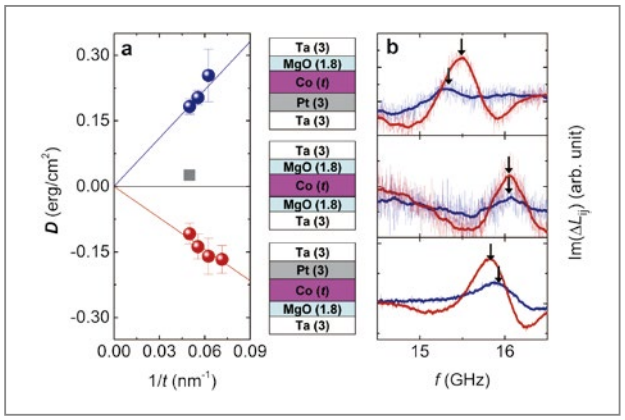

Figure 3. Interfacial DMI depending on the sample asymmetry, and corresponding frequency response of spin wave propagation.
(a) Measured DMI (D) of the MgO/Co (t nm)/Pt (red circles) and Pt/Co (t nm)/MgO (blue circles) samples as a function of the reciprocal of Co film thickness ($1/t$) with a fixed k of 7.85 μm^{-1}. The D of an MgO/Co/MgO sample having symmetric interfaces (square) is also shown.
(b) The imaginary part of mutual inductances, $Im(DL_{ij})$, measured with MgO/Co (20 nm)/Pt (top panel), MgO/Co (20 nm)/MgO (center panel), and Pt/Co (20 nm)/MgO (bottom panel) samples. Corresponding sample structures are shown on the left of the panels. The frequency responses are obtained with k = +7.85 μm^{-1} (red lines) and k = -7.85 μm^{-1} (blue lines) with applying H = +500 Oe. The peak frequencies are indicated by arrows.

also show a substantial frequency shift, but the sign of frequency shift is now opposite to that of the Pt/Co/MgO structures (top panel). For the MgO/Co/Pt (Pt/Co/MgO) structures, the forward-going spin wave shows a peak at a lower (higher) frequency in comparison with that of the reverse-going spin wave, implying that the counter-clockwise (clockwise) alignment is energetically more stable than the clockwise (counter-clockwise) alignment in MgO/Co/Pt (Pt/Co/MgO) systems. This sign reversal of frequency shift, once again, strongly supports that the measured frequency shift is dominantly induced by *i*-DMI, since the DMI vector changes its sign with the structure inversion. It is noteworthy that the MgO/Co/MgO sample (center panel), having nominally symmetric interfaces, shows a negligible frequency shift, implying that the contribution from the top MgO/Co interface has been canceled out by the contribution from the bottom Co/MgO interface.

Conclusion and outlook

The presence of interfacial DMI changes the energy of the magnetic system and lifts the degeneracy in the spin wave frequency with respect to the spin wave propagating direction. By analyzing the substantial frequency shift depending on the spin chirality, we find that the DMI originates dominantly from the interfaces, and the sign of DMI corresponds to the inversion asymmetry of the film structures. We believe that this investigation using an all-electrical method will lead to a deeper understanding of the interfacial DMI in ferromagnetic nanostructures.

Clearly the impact of this work extends well beyond a simple measurement of sign and magnitude of DMI using spin wave. Spin wave or magnon (i.e., the quantum of spin wave) also raises the prospects of realizing an energy-efficient computing technology, namely, magnon spintronics or magnonics. A wide range of spin wave devices can be envisioned from the demonstrated effect of DMI on the spin wave propagation. For example, spin wave logic devices and magnon transistors are possible concepts where the collective spin wave is electrically excited and modulated (see Figure 4). The electrical excitation and detection of spin waves and the influence of interfacial DMI on collective spin-wave dynamics will pave the way to the emerging field of spin-wave logic devices.

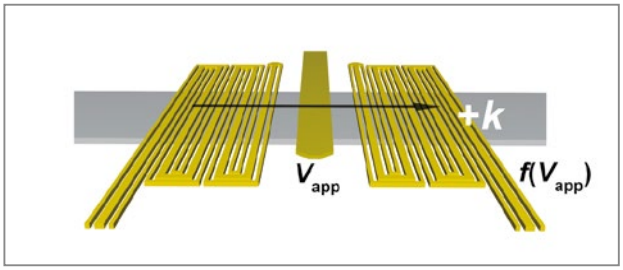

Figure 4. Frequency modulation of spin wave by voltage bias. Schematic diagram of a spin-wave modulator with an external voltage bias, which is assumed to control the magnitude of interfacial DMI (D_i). The spin-wave frequency at the detector is modulated as a function of voltage bias (V_{app}) .

Note

The contents used in this article are drawn from "All-electrical measurement of interfacial Dzyaloshinskii-Moriya interaction using collective spin-wave dynamics" in *Nano Letters* 2015, Vol. 16, pg. 62.

References

[1] Dzyaloshinsky I. *J. Phys. Chem. Solids* 1958; 4: 241-255.

[2] Moriya T. *Phys. Rev.* 1960; 120: 91-98.

[3] Bode M, Heide M, von Bergmann K, Ferriani P, Heinze S, Bihlmayer G, Kubetzka A, Pietzsch O, Blugel S, Wiesendanger R. *Nature* 2007; 447: 190-193.

[4] Yu XZ, Onose Y, Kanazawa N, Park JH, Han JH, Matsui Y, Nagaosa N, Tokura Y. *Nature* 2010; 465: 901-904.

[5] Yu XZ, Kanazawa N, Onose Y, Kimoto K, Zhang WZ, Ishiwata S, Matsui Y, Tokura Y. *Nat Mater* 2011; 10: 106-109.

[6] Chen G, Ma T, N'Diaye AT, Kwon H, Won C, Wu Y, Schmid AK. *Nat. Commun.* 2013; 4: 2671.

[7] Thiaville A, Rohart S, Jué É, Cros V, Fert A. *Europhys. Lett.* 2012; 100: 57002.

[8] Fert A, Cros V, Sampaio J. *Nat. Nano* 2013; 8: 152-156.

[9] Emori S, Bauer U, Ahn S-M, Martinez E, Beach GSD. *Nat. Mater.* 2013; 12: 611-616.

[10] Ryu K-S, Thomas L, Yang S-H, Parkin S. *Nat. Nano* 2013; 8: 527-533.

[11] Je S-G, Kim D-H, Yoo S-C, Min B-C, Lee K-J, Choe S-B. *Phys. Rev. B* 2013; 88: 214401.

[12] Hrabec A, Porter NA, Wells A, Benitez MJ, Burnell G, McVitie S, McGrouther D, Moore TA, Marrows CH. *Phys. Rev. B* 2014; 90: 020402.

[13] Ryo H, Kim K-J, Yoshinobu N, Takahiro M, Teruo O. *Japan J. Appl. Phys.* 2014; 53: 108001.

[14] Udvardi L, Szunyogh L. *Phys. Rev. Lett.* 2009; 102: 207204.

[15] Zakeri K, Zhang Y, Prokop J, Chuang TH, Sakr N, Tang WX, Kirschner J. *Phys. Rev. Lett.* 2010; 104: 137203.

[16] Cortés-Ortuño D, Landeros P. *J. Phys. Cond. Matter* 2013; 25: 156001.

[17] Moon J-H, Seo S-M, Lee K-J, Kim K-W, Ryu J, Lee HW, McMichael RD, Stiles MD. *Phys. Rev. B* 2013; 88: 184404.

[18] Di K, Zhang VL, Lim HS, Ng SC, Kuok MH, Yu J, Yoon J, Qiu X, Yang H. *Phys. Rev. Lett.* 2015; 114: 047201.

[19] Nembach HT, Shaw JM, Weiler M, Jué E, Silva TJ. *Nat Phys.* 2015; 11: *825.*

[20] Stashkevich AA, Belmeguenai M, Roussigné Y, Cherif SM, Kostylev M, Gabor M, Lacour D, Tiusan C, Hehn M. *Phys. Rev. B* 2015; 91: 214409.

[21] Belmeguenai M, Adam J-P, Roussigné Y, Eimer S, Devolder T, Kim J-V, Cherif SM, Stashkevich A, Thiaville A. *Phys. Rev. B* 2015; 91: 180405.

[22] Cho J, Kim N-H, Lee S, Kim J-S, Lavrijsen R, Solignac A, Yin Y, Han D-S, van Hoof NJJ, Swagten HJM, Koopmans B, You C-Y. *Nat. Commun.* 2015; 6: 7635.

[23] Vlaminck V, Bailleul M. *Science* 2008; 322: 410-413.

[24] Damon RW, Eshbach JR. *J. Phys. Chem. Solids* 1961; 19: 308-320.

Feature Articles

Black Phosphorus–Zinc Oxide 2D-1D Nano Hybrid p–n Diode and Junction Field-Effect Transistor

Young Tack LEE
Center of Opto-Electronic Materials and Devices
Post-Silicon Semiconductor Institute
023273@kist.re.kr

Won Kook CHOI
Materials and Life Science Research Division
wkchoi@kist.re.kr

Do Kyung HWANG
Center of Opto-Electronic Materials and Devices
Post-Silicon Semiconductor Institute
dkhwang@kist.re.kr

Introduction

In addition to graphene, several other promising two dimensional (2D) semiconductors, including transition metal dichalcogenide [1-5] and black phosphorus nanosheet (BP or phosphorene) [6-10], have recently attracted much attention from researchers due to their relatively high mobility and distinct energy band gap. BP nanosheet is somewhat similar to graphene in two respects: it is composed of single element phosphorus (P) and has quite high mobilities, depending on how it is fabricated. Its bandgap is reported to range from 0.3 to 1 eV, depending on its thickness. Additionally, there have been exciting reports on its crystal structure [11,12], mechanical flexibility [13,14], ambient stability [15,16], high anisotropic mobilities in field effect transistors (FETs) [17,18], and even on its use in heterojunction p-n diodes [19, 20].

The focus of this study is on BP-ZnO heterojunction p-n diodes and junction field effect transistors (JFETs) with n-ZnO channels. These devices take advantage of the mechanical flexibility and p-type conduction of BP through a process whereby the van der Waals heterojunction is fabricated on glass substrate by the direct imprinting of 17 nm-thin BP nanosheet on 85 nm-thick ZnO nanowire. Such a one dimension-two dimension (1D-2D) hybrid junction has rarely been used in p-n diodes [21] and has never been reported in JFETs to the best of our knowledge. Our BP-ZnO nano-dimension p-n diode demonstrates static rectification curves with a high

ON/OFF ratio of ~10^4 as well as a kilohertz dynamic rectification at a few volt AC application. Moreover, the heterojunction we designed between ZnO and BP successfully enables the production of a ZnO channel JFET which demonstrates kilohertz switching dynamics. As a result, it is expected that our BP-ZnO junction devices will have an important role to play in future nanoelectronics.

Results and discussion

2D BP – 1D ZnO heterojunction p-n diode

Figures 1a~c display the fabrication of BP-ZnO nanowire junction devices in a step-by-step manner. An 85 nm-thick ZnO nanowire having two terminals with an Au/Ti ohmic electrode was initially used [22,23]. Then, a 17 nm-thin BP nanosheet was transferred to directly cover the center of the ZnO nanowire and form a van der Waals junction interface as aforementioned. Since the length of the BP sheet was sufficiently long, our BP had two terminals with Au/Ti ohmic metal, as seen in the optical microscopy image of Figure 1c, where the BP nanosheet is located vertically to the ZnO nanowire

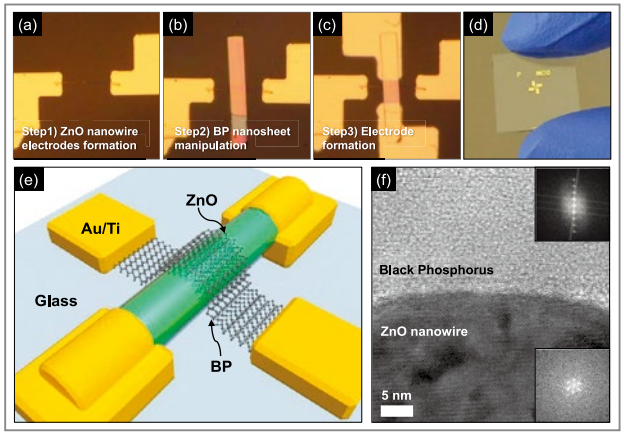

Figure 1. (a)~(c) Fabrication steps in the production of a black phosphorus (BP)-ZnO nanowire heterojunction device. (d) Photographic snapshot and (e) schematic illustration of our BP-ZnO heterojunction device as fabricated on glass substrate. (f) Cross-sectional STEM image of BP-ZnO junction along with reciprocal lattices.

in the fabrication process. A photographic snapshot and schematic 3D view of our device are illustrated in Figures 1d and 1e. Scanning transmission electron microscopy was also used to obtain a cross sectional image of our BP-ZnO junction (Figure 1f). Fourier transformation patterns for the reciprocal lattices of thin film BP and ZnO wire are noted as insets, the dotted line indicating that BP is 2D.

In Figure 2a, the two terminal current-voltage (I-V) measurements on ZnO nanowire and BP nanosheet (see inset photo) provide evidence that both ZnO nanowire and BP nanosheet maintain their ohmic behavior with Au/Ti contact, while the conductance of BP nanosheet (100 μS) appears to be two~three orders higher than that of ZnO nanowire (0.6 μS). Other two terminal I-V measurements were taken of BP nanosheet and ZnO nanowire. Results are shown in Figure 2b as the rectifying behavior of the p-n diode. It is regarded that a BP nanosheet/ZnO nanowire system is certainly a heterojunction p-n diode. The inset photo of Figure 2b displays the measurement setup for left and right diodes. The two diodes show almost the same properties in respect to the ON/OFF ratio (~10^4) and ideality factor (~1.3). Dynamic rectification was also observed from our p-n diode as seen in Figure 2c which is the time domain current plot obtained under 1 kHz square AC pulse (V_A = -5 ~ 5 V). The dynamic current at 5 V appears to be 10 μA, which is the same as the static one observed in Figure 2b. Another rectification dynamic (Figure 2d) was taken with 1 kHz sinusoidal AC pulses; this time a circuit with external resistance (R_{EXT} = 100 kΩ, see the inset of Figure 2d) was set up for output voltage (V_{OUT}) measurement. As can be seen in Figures 2c and 2d, no time delay was observed, implying that even higher frequency rectification is possible in our p-n diodes. It can be said with certainty that this BP-ZnO nanostructure heterojunction p-n diode has very promising properties. It is interesting to note that the ZnO and BP nanomaterials in the two terminal measurements (Figure 2a) independently showed linear conductance despite the

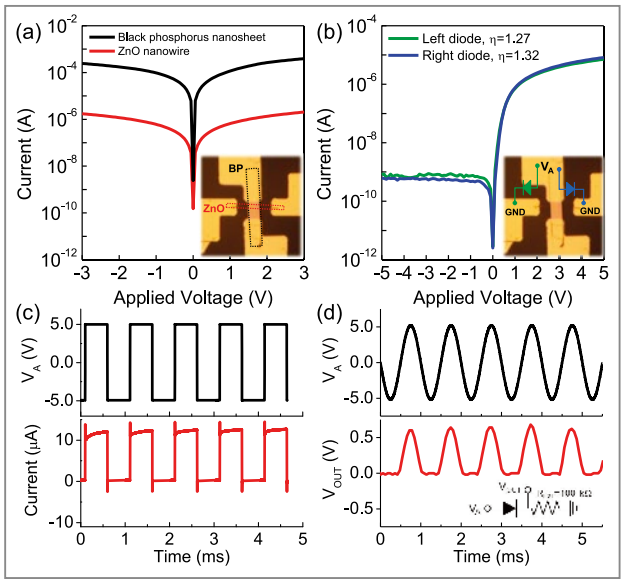

Figure 2. (a) Two terminal current-voltage (I-V) curves of BP nanosheet and ZnO nanowire channels shown in the inset photo. (b) Two terminal I-V curves of left and right p-n diodes shown in the measurement setup of the inset photo. (c) Rectified output current of our p-n diode under applied AC voltage of square waveform (V_A = ± 5 V) at 1 kHz. (d) Rectified output voltage obtained from the inset diode circuit with external resistor (R_{EXT} = 100 kΩ) under applied AC voltage of sine waveform (V_A = -5 ~ 5 V) at 1 kHz.

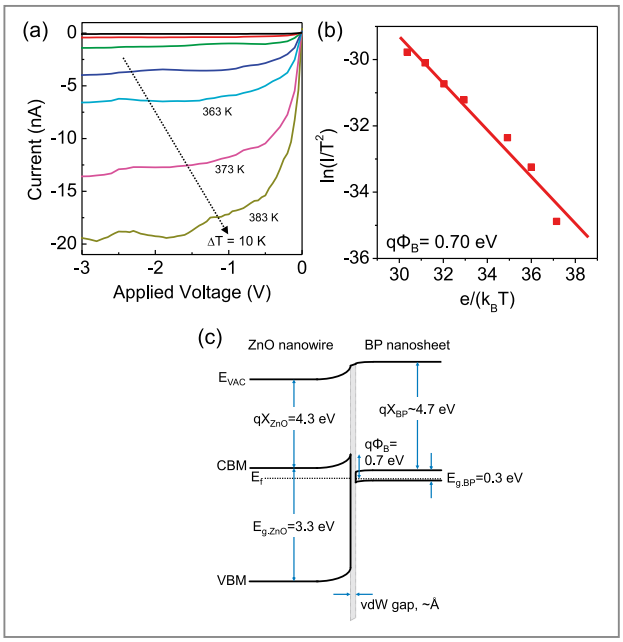

Figure 3. (a) Temperature-dependent current-voltage (I-V) curves of our p-n diode as obtained under the reverse bias condition of V_A= -5 ~ 0 V by elevating temperature from 323 to 383 K. (b) Richardson plot of ln(I/T^2) versus e/(k_BT). The potential barrier $q\Phi_B$, ~0.7 eV is obtained from the slope of the linear fit. (c) Energy band diagram of n-type ZnO nanowire and p-type BP nanosheet heterojunction with van der Waals (vdW) gap. Since the electron affinity (qX_{ZnO}) and E_g values of ZnO are known to be 4.3 and 3.3 eV, respectively, the electron affinity (qX_{BP}) can be extrapolated to be 4.7 eV.

fact that the ZnO nanowire lay across and beneath the BP nanosheet and had an overlapped area. These results imply that one nanochannel hardly influences the other unless the rectifying connection, such as that shown in Figure 2b, is involved. We can thus assume that ZnO and BP form a van der Waals (vdW) junction interface which affords a few angstrom gap between the two materials. Moreover, the high conductance and thickness of our p-type BP nanosheet indicate that our BP flake contains a high hole concentration as well as a low energy gap of ~0.3 eV. All of these results and observations enabled us to develop: 1) an approximation of the BP-ZnO nanomaterial heterojunction band diagram; and 2) the realization of a BP gate JFET with a ZnO channel.

Energy band alignment estimation

An approximate BP-ZnO nanomaterial band diagram could be drawn after experimentation involving a heterojunction energy barrier measurement which is conceptually the same or at least similar to the Schottky barrier measurement assuming thick BP as a metallic conductor. For such barrier analysis, we implemented reverse bias I-V measurements at various elevated temperatures (Figure 3a) based on the following Schottky barrier equation (1) [24],

$$I = AA^*T^2 exp\left(\frac{-q\Phi_B}{k_BT}\right)\left[exp\left(\frac{qV_A}{k_BT}\right) - 1\right] \quad (1)$$

where A, A*, T, q, k_B and $q\Phi_B$ are the contact area, Richardson constant, temperature, electonic charge, Boltzmann constant, and Schottky barrier height, respectively. V_A is applied reverse bias voltage. In the plot of Figure 3b, the slope is taken as $q\Phi_B$ and is here estimated to be ~0.7 eV. As a result, we could finally obtain an approximate band diagram of a BP-

ZnO heterojunction (Figure 3c) in which the vdW gap is depicted and BP is regarded as a strong p-type so that its Fermi energy (E_f) may be close to the valence band maximum (VBM). We consider this heterojuction band digram to be critical for the understanding of the operation of our heterojunction p-n diode.

ZnO channel JFET and inverter operation

The vdW interfaces made it possible to test the operations of two types of JFETs, one integrating a BP nanosheet channel and the other with a ZnO nanowire channel. Figure 4a displays the drain current-gate voltage (I_D-V_{GS}) transfer characteristics and gate leakage (I_G) behavior obtained from a BP channel JFET (its circuit configuration is shown in the inset photo). As shown, I_D of ~0.1 mA never changed with V_{GS} while I_G maintained a low level of 10 nA. (Note that it increased to 1 μA at V_{GS} of -2 V or below, which drove a forward bias action for the ZnO-BP p-n diode.) It is thus quite evident that our BP contains high density hole carriers which effectively screen the gate-induced electric field. As a result, a BP-channel JFET did not function effectively. In contrast, the other JFET incorporating a ZnO channel and BP gate appeared to operate well, as evidenced by an ON/OFF I_D ratio of ~$2'10^3$ as reflected in the transfer characteristics shown in Figure 4b. This figure also shows low I_G of a few nA (the circuit configuration is shown in the inset photo) and OFF I_D of ~1 nA at -1 V gate voltage. Output characteristics (I_D-V_{DS}) of the ZnO-channel JFET showed good I_D saturation (Figure 4c) which clearly started from 2 V drain voltage. Transconductance plots in Figure 4d display a maximum of 1.7 μS at 1 V gate voltage. The inset drawings illustrate nanowire device cross sections for ON and OFF states. We attribute this successful JFET operation to the vdW interface, which would protect channel nanomaterials from any mutual (contamination/chemical) influence, as previously shown in Figure 2a.

As shown in the inset circuit of Figure 5a, a resistive-load inverter was also set up with our JFET and 10 MΩ external resitor to extend the usage of our JFET for

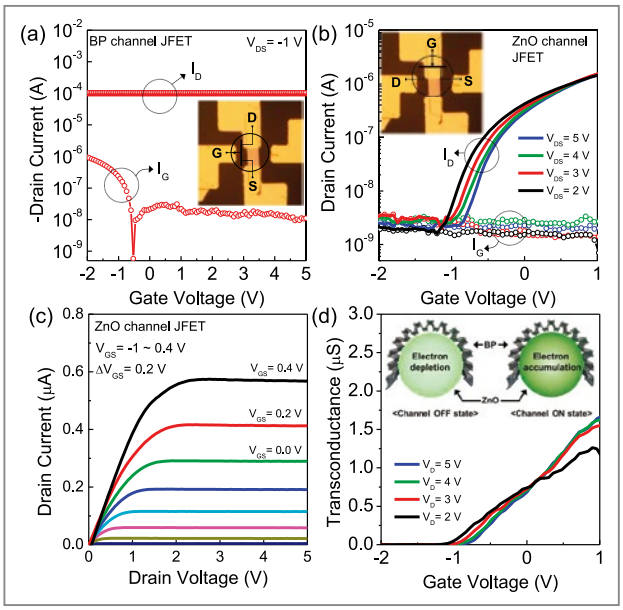

Figure 4. (a) Drain current-gate voltage (I_D-V_{GS}) transfer curves of BP nanosheet JFET under ZnO nanowire gating at V_{DS} = -1 V. (b) Drain current-gate voltage (I_D-V_{GS}) transfer curves of ZnO nanowire channel JFET under BP nanosheet gating at V_{DS} = 2 ~ 5 V. (c) Drain current-drain voltage (I_D-V_{DS}) output curves of ZnO nanowire channel JFET under V_{GS} showing increases from -1 to 0.4 V with a 0.2 V step. Saturation clearly starts from 2 V. (d) Transconductance ($g_m = dI_D/dV_{GS}$) curves of our ZnO channel JFET as a function of gate voltage. Inset cross section views illustrate ON and OFF states of BP-gated JFET with nanowire channel.

further practical application. Figure 5a shows the voltage transfer characteristics (VTCs) of our inverter and its voltage gain is displayed in the plots of Figure 5b. These figures demonstrate that the peak static gain of ~4 was achieved at 5 V of supplied voltage (V_{DD}). Under this supplied voltage, inverter switching dynamics were then carried out with a square pulse AC voltage input of 0.5 V. Figures 5c and 5d exhibit 0.1 and 1 kHz switching dynamics, respectively. Top and bottom output signals were observed to be 4 and 1.5 V, respectively, which is precisely the same as the values in the static VTC curve of Figure 5a (as noted by dots). For this inverter switching, the maximum RC delay appeared to be ~250 μs along with an AC gain of ~2.5. Since no apparent overlap capacitance existed in our nanowire channel JFET, such delay is attributed to resistance involved with the ZnO nanowire itself as well as the ZnO nanowire/

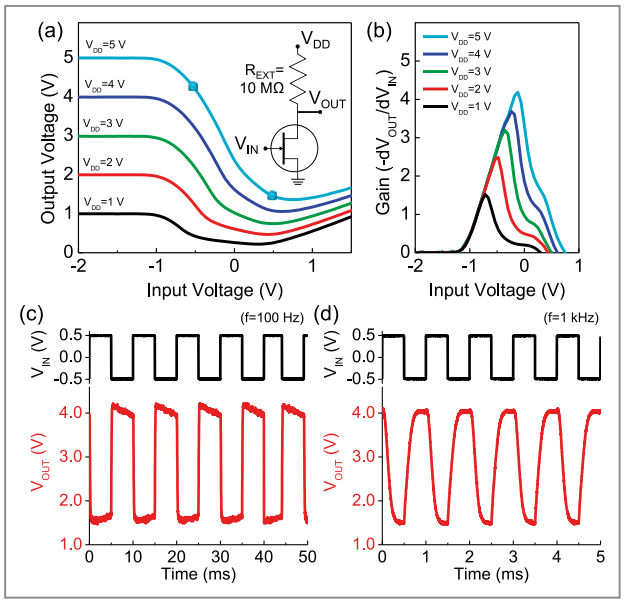

Figure 5. (a) Voltage transfer characteristics obtained from a load-resistive inverter setup comprised of our ZnO channel JFET and an external resistor of 10 MΩ (inset circuit) under supply voltages of V_{DD}s = 1 ~ 5 V. (b) Voltage gain ($-dV_{OUT}/dV_{IN}$) curves as a function of input voltages. Dynamic switching behavior of our resistive-load inverter under AC square waves at (c) 100 Hz and (d) 1 kHz. AC gain of 2.5 and RC delay of 250 μs were obtained from this inverter setup.

Ti contact. To improve the inverter's performance as regards electrostatics and dynamics, it will be necessary to undertake more study of property optimization. Nonetheless, our study clearly demonstrated that the BP nanosheet-ZnO nanowire vdW heterojunction can work effectively in both p-n diode and JFET devices.

Conclusion

We fabricated BP nanosheet-ZnO nanowire heterojunction p-n diodes and JFETs with n-ZnO channels on glass, taking advantage of the mechanical flexibility and p-type conduction of BP. As a result, our BP-ZnO nano-dimension p-n diode displayed a high ON/OFF ratio of ~10^4 in static rectification and showed kilohertz dynamic rectification. ZnO channel JFET operations were nicely demonstrated by BP gate switching in both electrostatics and kilohertz dynamics. This successful JFET operation is attributed to the vdW junction interface between ZnO and BP. These findings lead us to conclude that our BP-ZnO vdW heterojunction respresents a promising advance in the development of future nanoelectronic devices.

Note

This article and images are drawn from "Black Phosphorus–Zinc Oxide Nanomaterial Heterojunction for p–n Diode and Junction Field-Effect Transistor" in *Nano Letters*, Vol. 16, pp. 1293-1298.

References

[1] Lee HS, Min SW, Chang YG, Park MK, Kim T, Kim H, Kim JH, Ryu S, Im S. *Nano Lett.* 2012; 12: 3695-3700.

[2] Coleman JN, Lotya M, O'Neill A, Bergin SD, King PJ, Khan U, Young K, Gaucher A, De S, Smith RJ, Shvets IV, Arora SK, Stanton G, Kim HY, Lee K, Kim GT, Duesberg GS, Hallam T, Boland JJ, Wang JJ, Donegan JF, Grunlan JC, Moriarty G, Shmeliov A, Nicholls RJ, Perkins JM, Grieveson EM, Theuwissen K, McComb DW, Nellist PD, Nicolosi V. *Science* 2011; 331: 568-571.

[3] Wang QH, Kourosh KZ, Kis A, Coleman JN, Strano MS. *Nat. Nanotechnol.* 2012: 7: 699-712.

[4] Chhowalla M, Shin HS, Eda G, Li LJ, Loh KP, Zhang H. *Nat. Chem.* 2013; 5: 263-275.

[5] Kuc A, Zibouche N, Heine T. *Phys. Rev. B* 2011; 83: 245213.

[6] Das S, Zhang W, Demarteau M, Hoffmann A, Dubey M, Roelofs A. *Nano Lett.* 2014; 14: 5733-5739.

[7] Churchill HOH, Jarillo-Herrero P. *Nat. Nanotechnol.* 2014; 9: 330-331.

[8] Wu RJ, Topsakal M, Low T, Robbins MC, Haratipour N, Jeong JS, Wentzcovitch RM, Koester SJ, Mkhoyan KA. *J. Vac. Sci. Technol. A* 2015; 33: 060604.

[9] Liu H, Neal AT, Zhu Z, Luo Z, Xu X, Tománek D, Ye PD. *ACS Nano* 2014; 8: 4033-4041.
[10] Lee YT, Kwon H, Kim JS, Kim HH, Lee YJ, JA, Song YW, Yi Y, Choi WK, Hwang DK, Im S. *ACS Nano* 2015; 9: 10394-10401.
[11] Tran V, Soklaski R, Liang Y, Yang L. *Phys. Rev. B* 2014; 89: 235319.
[12] Castellanos-Gomez A, Vicarelli L, Prada E, Island JO, Narasimha-Acharya KL, Blanter SI, Groenendijk DJ, Buscema M, Steele GA, Alvarez JV, Zandbergen HW, Palacios JJ, Van der Zant HSJ. *2D Mater.* 2014; 1: 025001.
[13] Wei Q, Peng X. *Appl. Phys. Lett.* 2014; 104: 251915.
[14] Zhu W, Yogeesh MN, Yang S, Aldave SH, Kim JS, Sonde S, Tao L, Lu N, Akinwande D. *Nano Lett.* 2015; 15: 1883-1890.
[15] Na J, Lee YT, Lim JA, Hwang DK, Kim G, Choi WK, Song Y. *ACS Nano* 2014; 8: 11753-11762.
[16] Wood JD, Wells SA, Jariwala D, Chen KS, Cho E, Sangwan VK, Liu X, Lauhon LJ, Marks TJ, Hersam MC. *Nano Lett.* 2014; 14: 6964-6970.
[17] Fei R, Yang L. *Nano Lett.* 2014; 14: 2884-2889.
[18] Xia F, Wang H, Jia Y. *Nat. Commun.* 2014; 5: 4458.
[19] Deng Y, Luo Z, Conrad NJ, Gong Y, Najmaei S, Ajayan PM, Lou J, Xu X, Ye PE. *ACS Nano* 2014; 8: 8292-8299.
[20] Gehring P, Urcuyo R, Duong DL, Burghard M, Kern K. *Appl. Phys. Lett.* 2015; 106: 233110.
[21] Jariwala D, Sangwan VK, Wu CC, Prabhumirashi PL, Geir ML, Marks TJ, Lauhon LJ, Hersam MC. *Proc. Natl. Acad. Sci. U.S.A.* 2013; 110: 18076-18080.
[22] Raza SRA, Shokouh SHH, Lee YT, Ha R, Choi HJ, Im S. *J. Mater. Chem. C* 2014; 2: 4428-4435.
[23] Jeon PJ, Lee S, Lee YT, Lee HS, Oh K, Im S. *J. Mater. Chem. C* 2013; 1: 7303-7307.
[24] Yang H, Heo J, Park S, Song HJ, Seo DH, Byun KE, Kim P, Yoo IK, Chung HJ, Kim K. *Science* 2012; 336: 1140-1143.

Technical Review

High-Performance Thermoelectric Paper Based on Carrier-Filtering Processes at Carbon Material/Tellurium Nanowire Heterojunctions

Hee Suk KIM
Photo-electronic Hybrids Research Center
National Agenda Research Division
heesukkim@kist.re.kr

Jae Yoo CHOI
Photo-electronic Hybrids Research Center
National Agenda Research Division
Calla13@kist.re.kr

Introduction

Thermoelectric (TE) materials are very effective in harvesting electricity from heat sources or cooling/heating devices without moving parts [1]. Their energy conversion efficiency is evaluated by a dimensionless figure of merit (ZT), given by

$$ZT = (S^2\sigma)\, T/\kappa \quad (1)$$

where S, σ, T, and κ are the Seebeck coefficient (also called the thermopower), electrical conductivity, absolute temperature, and thermal conductivity, respectively. Equation 1 shows that high ZTs are achieved with high S and σ and low κ. Inorganic semiconductors and their alloys are perhaps the most commonly used TE materials because their high-quality crystalline structures allow effective and large-scale energy transport [2-4]. Three fundamental concepts are currently being investigated to improve the performance of inorganic TE materials: (1) the quantum confinement effect, whereby sharp increases in the electronic density of states can lead to increased thermopower; (2) the energy filtering effect, whereby energy-dependent scattering of charge carriers can increase the thermopower without a major decrease in the electrical conductivity; and (3) phonon scattering, whereby nanostructures limit the mean free paths of phonons but not of electrons, reducing the lattice thermal conductivity without affecting the electrical conductivity [5-8]. Recently, the phonon scattering and energy filtering effect have been exploited via the introduction of superlattices, nanoinclusions, and composites to significantly improve the performance

of inorganic TE materials [9-12]. However, these inorganic nanostructures have some drawbacks. Indeed, the scarcity and fragility of the raw materials and the expensive fabrication processes that are required limit the more general commercial use of inorganic TE materials, notably for flexible/or wearable power conversion devices [13, 14]. Flexibility is also crucial to cover and adhere closely to the heat sources that emit low thermal radiation in practical applications at temperature ranges lower than 400 K.

Flexible TE materials have already been investigated to overcome the limitations of inorganic semiconductors. Early studies focused on the TE properties of homogeneous organic materials such as polymers [15-17] or carbons [18-21] not only because of their unique electronic properties, but also because of their low-cost, light weight, and flexibility. More recently, hybrid systems designed to exploit the advantages of each component have led to enhanced TE performance [22]. For example, a carbon nanotube/poly(vinyl acetate) (PVAc) hybrid with ZT = 0.006 at room temperature (RT) [23], a single-walled carbon nanotube (SWCNT)/poly(styrenesulfonate) doped poly(3,4-ethylenedioxythiophene) (PEDOT:PSS) hybrid with ZT = 0.02 at RT [24], and a MWCNT/polyvinylidene fluoride composite with ZT = 0.02 at RT [25] have been reported. Elsewhere, the potential of flexible inorganic semiconductor/polymer composites, notably Bi_2Te_3/PEDOT:PSS, have also been investigated [26, 27]. Interestingly, a few studies have reported hybrid materials with significantly enhanced TE performance, possibly due to the efficient energy filtering introduced in the inorganic TE area. Yu et al. prepared carbon nanotube/PEDOT:PSS/PVAc composites with a ZT of ~0.2 at RT by possibly filtering low energy carriers at the carbon-polymer junctions [28]. Further, See et al. presented Te nanowire/PEDOT:PSS composites with increased thermopower, indicating the potential of energy filtering at inorganic semiconductor-polymer junctions [29]. However, the improvements achieved so far are based on speculation concerning the energy filtering effects involved and systematic study is still lacking. Therefore, a more systematic understanding of the energy filtering effect at organic-organic or organic-inorganic interfaces is desirable to improve the performance of organic composites for potential applications in flexible TE devices. The review presented here focuses on a rationally designed high-performance thermoelectric paper based on carrier-filtering processes at carbon material/tellurium nanowire heterojunctions.

Concept of carrier filtering

In TE composites, the interfacial energy barrier between the two materials governs the transport of carriers across the interface. Shakouri and Bowers introduced the concept of carrier filtering in 1997, whereby the selective emission of hot electrons over interfacial barriers enhances the TE performance of inorganic semiconductor heterostructures [30]. This ensures that low energy carriers are filtered out within the narrow energy barrier, increasing the average potential energy of the carriers and thereby the thermopower of the material, with only a small decrease in its electrical conductivity.

Carbon nanotubes/tellurium nanowire heterojunction

We prepared a simple SWCNT-doped inorganic semiconductor hybrid film with a rationally engineered SWCNT work function to systematically tune the energy filtering at the carbon-inorganic semiconductor interfaces. Tellurium nanowire (TeNW) as a 1-dimensional inorganic semiconductor and SWCNT were selected due to their high thermopower and electrical conductivity, respectively. The SWCNT work function was controlled by acid treatment, lowering the interfacial barrier between the SWCNTs and TeNWs from 0.82 to 0.23

eV to selectively scatter low-energy carriers at the interface. Because strong acids such as nitric/sulfuric mixture lead to the extensive formation of defects, they dramatically decrease the electrical conductivity of the SWCNTs; however, nitric acid by itself allows the electrical conductivity, work function, and dispersibility of the SWCNTs to be controlled as a function of the sonication time at RT. Short treatment time (2 h) with nitric acid ensures that oxide impurities on the surface of the bare SWCNTs are removed, leading to the purified SWCNTs (p-SWCNT). The electrical conductivity of the SWCNT treated with nitric acid for 4 h (a-SWCNT) is 4 times higher than that of p-SWCNT because the acid treatment drastically reduces the junction resistance between individual tubes and bundles, thereby increasing hole mobility. The carrier concentrations of a-SWCNT and p-SWCNT are similar, at 2.67×10^{20} and 2.48×10^{20} cm^{-3}, respectively, but the mobility in the former - and therefore its electrical conductivity - is 4 times higher than that of p-SWCNT.

We hybridized the TeNWs with the p-SWCNT to get a higher barrier height of 0.82 eV and compared them with a-SWCNT/TeNW film with a 0.23 eV barrier height. As shown in Figure 1a, the a-SWCNT/TeNW hybrid film has a higher electrical conductivity than the p-SWCNT/TeNW film with the same SWCNT content. This is probably due to the higher electrical conductivity of the as-prepared a-SWCNT. As expected, Figure 1b shows that the thermopower of the a-SWCNT/TeNW film is slightly lower than that of the film prepared with the same concentration of p-SWCNT. As a result, the a-SWCNT/TeNW hybrid film has a higher power factor ($S^2\sigma$) than the p-SWCNT/TeNW film at the same SWCNT content (Figure 1c). This is because the a-SWCNT/TeNW film has a relatively high thermopower with increasing electrical conductivity compared with the p-SWCNT/TeNW film. Figure 1d shows the thermopower of the two hybrid films as a function of their electrical conductivity. It is noteworthy that for electrical conductivities ranging from 10 to 50 S/m, the a-SWCNT/TeNW hybrid films

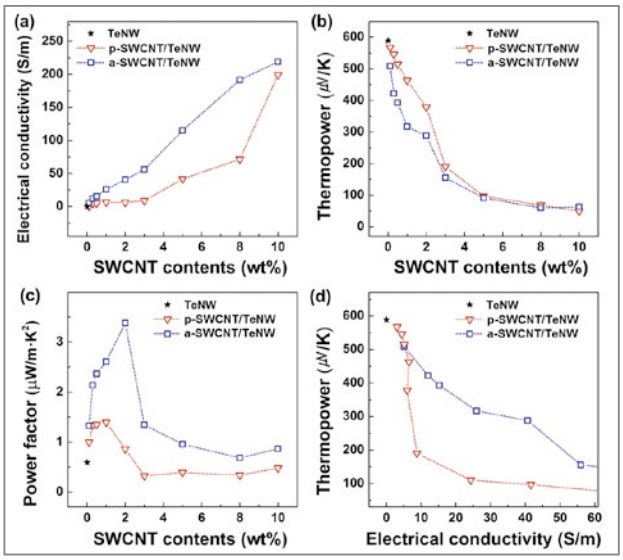

Figure 1. (a) Electrical conductivity, (b) thermopower, and (c) power factor of SWCNT/TeNW hybrid films as a function of SWCNT content. (d) Thermopower of the hybrid film as a function of electrical conductivity.

show a significantly higher thermopower than those prepared with p-SWCNT. This points toward more effective energy filtering at the a-SWCNT-TeNW interfaces due to the lower energy barrier of 0.23 eV.

The alignment of the SWCNT and TeNW bands is illustrated in Figure 2. TeNWs form a degenerate semiconductor with a narrow band gap of 0.33 eV in which the Fermi level is positioned close to the valence band. The work function of these TeNWs is assumed to be the same as that of bulk Te. Moreover, the Fermi level of doped SWCNTs is known to be within the valence band. The equilibrium band diagram in Figure 2a for the p-SWCNT/TeNW hybrid film indicates that the 0.82 eV energy barrier scatters most charge carriers, reducing carrier transfer, the thermopower, and the power factor of this composite. In contrast, for the a-SWCNT/TeNW hybrid film, Figure 2b shows that low-energy carriers are filtered out by the 0.23 eV potential barrier while high-energy carriers readily cross the interface. The 4-fold enhancement of the power factor for the a-SWCNT/TeNW composite is therefore attributed to effective energy filtering at the a-SWCNT-TeNW interfaces. It

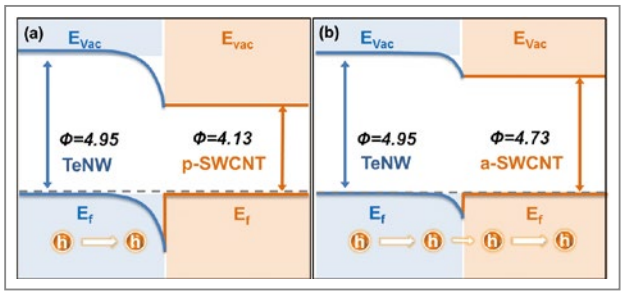

Figure 2. Energy diagrams of (a) p-SWCNT/TeNW and (b) a-SWCNT/TeNW hybrid films.

is worth mentioning that a more precise control of the SWCNT work function and more precise measurements thereof could allow the energy filtering effect to be exploited at other carbon-inorganic semiconductor interfaces.

Graphene/PEDOT:PSS/tellurium nanowire heterojunction

While we controlled the energy barrier between carbon materials and TeNWs by adjusting the work function of carbon materials (SWCNT), as described in the previous section, we introduced a conducting polymer (PEDOT:PSS) between carbon materials (reduced graphene oxide) and TeNWs for an optimized energy barrier. To do this, we rationally designed a ternary hybrid paper of reduced graphene oxide (rGO)/PEDOT:PSS/TeNW which consisted of two heterojunctions at rGO/PEDOT:PSS and PEDOT:PSS/TeNW and demonstrated that the two interfaces could act as energy filters to scatter low-energy carriers. Our rationally designed concept of flexible TE paper is illustrated in Figure 3a. First, we synthesized PEDOT:PSS-coated TeNWs (DTe) and characterized its structural morphology. Well-dispersed DTe in water was mixed with a graphene oxide (GO) aqueous solution and vacuum filtered. The as-prepared GO-DTe hybrid paper was 50 μm in thickness on average and showed great flexibility due to the mechanical strength of 2-D GO sheets. After film formation, the

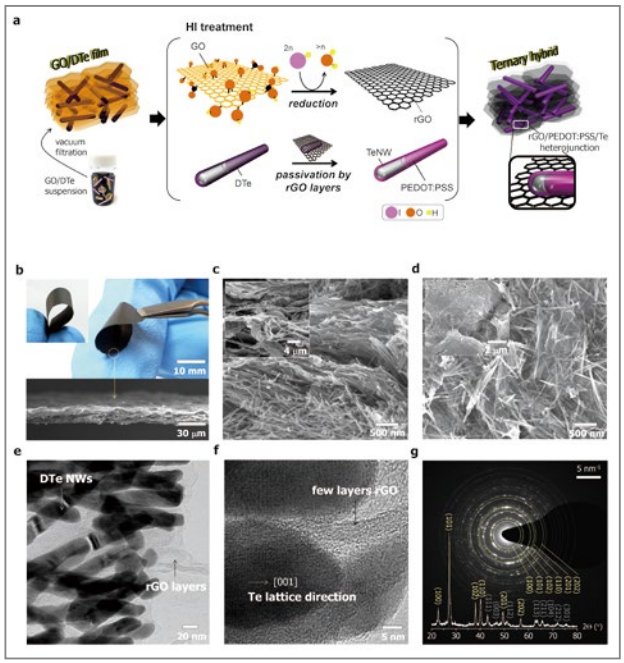

Figure 3. Synthesis of GDTe hybrid paper. (a) Schematic illustration of our rationally designed TE hybrid paper. (b) Photographs of flexible $G_{0.1}DTe_{0.9}$ hybrid paper prepared with HI reduction at 40°C for 72 h. (c, d) Cross-sectional and surface SEM images of the $G_{0.1}DTe_{0.9}$ hybrid paper. (e, f) HR-TEM images of the $G_{0.1}DTe_{0.9}$ hybrid showing hybrid heterojunction between few rGO layers and several DTe nanowires. (g) SAED pattern obtained from TEM image and XRD spectrum of the as-prepared DTe nanowire.

GO-DTe paper had to be chemically reduced in order to enhance the TE properties because GO itself is an electronic insulator. Figure 3b shows the great flexibility of the reduced GO-DTe (GDTe) hybrid paper and Figures 3c and 3d show the cross-sectional and surface scanning electron microscopy images of the hybrid paper. These results indicate that the GDTe hybrid paper has a porous microstructure and hierarchically layered morphology composed of a few rGO layers with DTe randomly distributed between the layers.

The power factor reaches its maximum for a hybrid composition of $G_{0.1}DTe_{0.9}$, and a hybrid paper with less than 10 wt% of GO content is not flexible. Therefore, we fixed the DTe content in the hybrid to 90 wt% and evaluated the TE properties of the hybrid paper as a function of the HI reduction time (Figure 4). As expected,

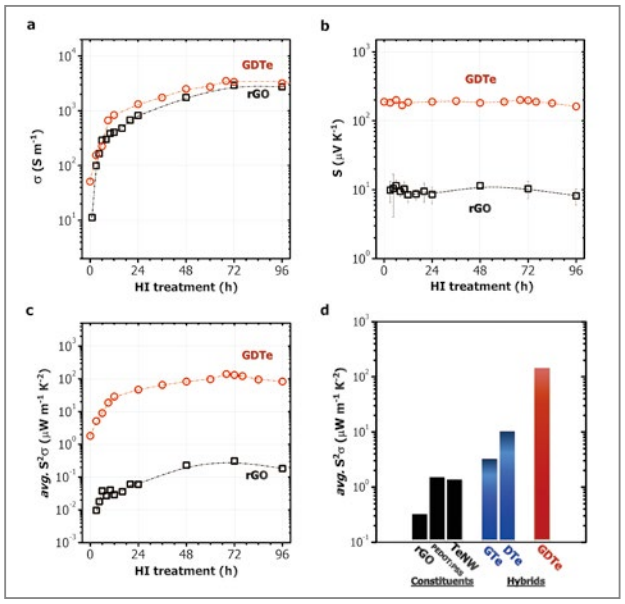

Figure 4. TE properties of GDTe hybrid paper. (a) Electrical conductivities, (b) thermopowers, and (c) power factors of the $G_{0.1}DTe_{0.9}$ hybrid papers and rGO films as a function of HI treatment time at 40°C. (d) Power factors of single components (TeNW, PEDOT:PSS, and rGO) and hybrids (rGO/TeNW hybrid ($G_{0.1}Te_{0.9}$), PEDOT:PSS/TeNW hybrid ($D_{0.08}Te_{0.92}$), and $G_{0.1}DTe_{0.9}$).

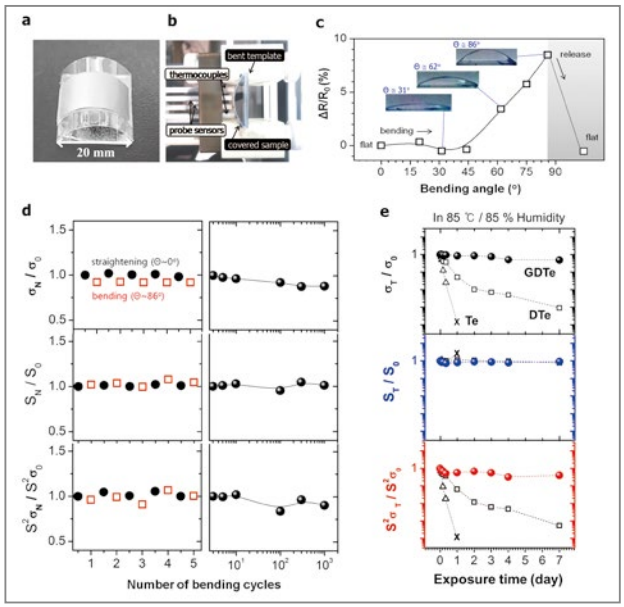

Figure 5. Mechanical and chemical TE stabilities of GDTe paper. (a, b) Photographs of an as-prepared specimen deposited on a template bent at Θ ~ 86° and the experimental setup for TE bending test. (c) Ratio of resistance variation (ΔR) to initial resistance (R_0) of the $G_{0.1}DTe_{0.9}$ paper as a function of bending angle. (d) Ratios of electrical conductivity (σ_N), thermopower (S_N), and power factor ($S^2\sigma_N$) of the $G_{0.1}DTe_{0.9}$ paper to their initial values as a function of the number of bending cycles. (e) Ratios of electrical conductivity (σ_T), thermopower (S_T), and power factor ($S^2\sigma_T$) of the $G_{0.1}DTe_{0.9}$ paper to their initial values as a function of exposure time in the 85°C/85 % humidity condition.

the TE properties of $G_{0.1}DTe_{0.9}$ hybrid paper show opposite trends compared to those from hybrid composition with increasing HI treatment time. The electrical conductivity of the hybrid paper drastically increases with the HI treatment time owing to the graphitization of GO to rGO (Figure 4a). However, interestingly, the thermopower of the hybrid paper is rarely changed with HI treatment time, thereby leading to an increase in the power factor to 143 $\mu W \cdot m^{-1} \cdot K^{-2}$, which is significantly higher than that of single-component (TeNW, PEDOT:PSS and rGO) or binary hybrid materials (rGO/TeNW hybrid ($G_{0.1}Te_{0.9}$), PEDOT:PSS/TeNW hybrid ($D_{0.08}Te_{0.92}$)) (Figures 4b-d).

For practical use of the flexible TE paper, the mechanical and chemical durability had to be confirmed. We first controlled the bending angle of $G_{0.1}DTe_{0.9}$ paper, as shown in Figure 5a. The TE properties were directly measured in bent and flat states (Figure 5b). The resistance of the GDTe paper remained almost unchanged up to a bending angle of 45° and changed by less than 10% even at 90° (Figure 5c). When we characterized electrical conductivity, thermopower, and power factor of the GDTe paper as a function of the number of bending cycles, we observed a slight decrease (~ 10%) in the power factor without any serious decrease in performance after 1000 bending cycles; this was due to the small decrease in electrical conductivity as well as the stable thermopower (Figure 5d). These results demonstrate that the GDTe hybrid paper shows not only high flexibility but also good mechanical durability owing to the excellent mechanical strength and flexibility of the rGO layers. It is well-known that inorganic materials such as tellurium are very sensitive to oxidation and PEDOT:PSS is also sensitive to humidity, thus reducing its TE performance.

The TeNWs used in our study also had the problem of oxidation, resulting in morphological deformation. Therefore, we tested the chemical durability of TeNW, DTe and GDTe paper under an 85°C/85% humidity condition. After 7 days in this condition, while TeNW and DTe films showed a decrease in the power factor by three orders of magnitude, the GDTe paper showed a much higher chemical durability than the TeNW and DTe films (Figure 5e). This could be attributed to the chemical stability of the rGO layers that cover DTe nanowires effectively and act as a barrier to prevent the oxidation of TeNW.

Our rationally designed GDTe paper showed significant enhancement in TE performance as well as the mechanical and chemical durability described above. In order to systematically analyze the enhanced TE performance of the GDTe paper, we used Hall measurements of the carrier concentration and mobility in a pure TeNW, DTe, and GDTe hybrid. Pure TeNW film has a low electrical conductivity and a high thermopower based on low carrier concentration of 2.9×10^{18} cm^{-3} and mobility of 0.46 $cm^2 \cdot v^{-1} \cdot s^{-1}$. On the other hand, the binary DTe hybrid shows higher electrical conductivity of 224 $S \cdot m^{-1}$ and a lower thermopower of 204 $\mu V \cdot K^{-1}$, which are attributed to the higher carrier concentration of 3.7×10^{19} cm^{-3}. However, the degree of decrease in the thermopower is relatively low compared to the increase in the carrier concentration owing to the energy filtering at the interfaces between PEDOT:PSS and TeNW. It is important to consider the scattering time and carrier mobility to demonstrate the energy filtering at the junctions. We calculated the scattering time (defined as $\tau = \mu \cdot m^*/e$, where τ, μ and m^* are the scattering time, carrier mobility, and effective mass of the carrier, respectively) from the measured carrier mobility. The DTe film shows a shorter scattering time of 0.97×10^{-16} s and a lower mobility of 0.38 $cm^2 \cdot v^{-1} \cdot s^{-1}$ than pure TeNW (1.78×10^{-16} s and 0.46 $cm^2 \cdot v^{-1} \cdot s^{-1}$, respectively), indicating that more scattering events could have occurred in the DTe film. The ternary GDTe paper also shows the same trend as that of binary DTe film. The carrier concentration and mobility of the ternary hybrid are one order of magnitude higher than those of the DTe films, thus increasing electrical conductivity to 3496 $S \cdot m^{-1}$ with little difference in thermopower (202 $\mu V \cdot K^{-1}$) compared to that of the binary DTe film. Further, although the high thermopower of the ternary paper indicates energy filtering at the interfaces between rGO and PEDOT:PSS of DTe, the scattering time calculated from the measured carrier mobility is still higher than that of the DTe film. This can be attributed to the drastic increase in the high carrier mobility of rGO itself during reduction.

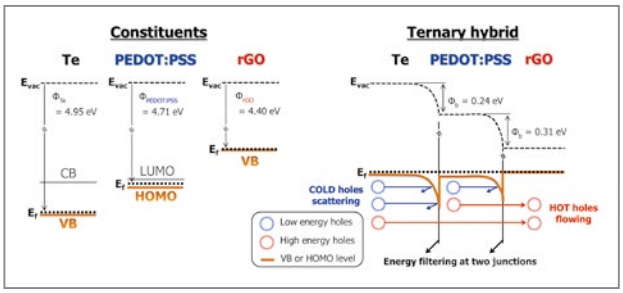

Figure 6. Energy filtering effects at two junctions. Energy diagram of the rGO/PEDOT:PSS/TeNW (bulk Te) heterojunctions showing energy filtering at two junctions, i.e., PEDOT:PSS/TeNW and rGO/PEDOT:PSS of DTe.

The energy diagram of the rGO/PEDOT:PSS/TeNW heterojunctions in Figure 6 shows the energy filtering at two junctions of PEDOT:PSS/TeNW and rGO/PEDOT:PSS of DTe. The equilibrium band diagram for the ternary GDTe hybrid indicates that the energy barriers of 0.24 and 0.31 eV at the PEDOT:PSS/TeNW and rGO/PEDOT:PSS interfaces, respectively, filter out low-energy carriers while they allow high-energy carriers to cross over the interfaces, thus enhancing TE performance. Notably, the binary hybrid ($G_{0.1}Te_{0.9}$) without PEDOT:PSS has a high energy barrier of 0.55 eV, but it has a low power factor of 0.03 $\mu W \cdot m^{-1} \cdot K^{-1}$, as mentioned above (Figure 4d). Therefore, this seems to be the optimum energy barrier value for efficient carrier filtering.

Conclusions

We presented two types of rationally designed high-performance thermoelectric papers. The first one is a flexible SWCNT-doped TeNW hybrid film. The SWCNT work function was controlled by acid treatment, the duration of which was optimized to lower the interfacial energy barrier between the SWCNTs and TeNWs. The power factor (3.40 $\mu W \cdot m^{-1} \cdot K^{-2}$ at RT) of the a-SWCNT/TeNW film with an interfacial barrier energy of 0.23 eV increased 3-fold compared to the pure TeNW film due to the doping of optimum a-SWCNT content into the TeNW matrix. This enhancement is also attributed to 12% enhanced energy filtering at the a-SWCNT-TeNW interfaces where low-energy carriers are filtered out, leaving only high-energy carriers to cross the barrier. The second paper we developed is a ternary hybrid paper composed of rGO, PEDOT:PSS, and TeNW to enhance TE performance as well as to improve flexibility and mechanical and chemical durability. The PEDOT:PSS passivated TeNW showed an 8-fold enhancement in the power factor over that of pure TeNW because of the energy-dependent filtering at the junction. Further, the introduction of rGO into this binary system resulted in a power factor 15-times higher than that of the binary film, which could be attributed to the additional energy filtering at the interface between the rGO and PEDOT:PSS.

Notes

This article and images are drawn from "Enhanced thermopower in flexible tellurium nanowire films doped using SWCNTs with a rationally designed work function" in *Carbon*, 2015; Vol. 94, pg. 577 and "High-performance thermoelectric paper based on double carrier-filtering processes at nanowire heterojunctions" in *Advanced Energy Materials*, 2016; Vol. 6, pg. 1502181.

References

[1] Bell LE. *Science* 2008; 321: 1457-61.

[2] Snyder GJ, Toberer ES. *Nat. Mater.* 2008; 7: 105-14.

[3] Yang J, Yip HL, Jen AKY. *Adv, Energy Mater.* 2013; 3: 549-65.

[4] Bux SK, Fleurial JP, Kaner RB. *Chem. Commun.* 2010; 46: 8311-24.

[5] Sootsman JR, Chung DY, Kanatzidis MG. *Angew. Chem. Int. Ed. Engl.* 2009; 48: 8616-39.

[6] Zebarjadi M, Esfarjani K, Dresselhaus MS, Ren ZF, Chen G. *Energy & Environ. Sci.* 2012;5:5147-62.

[7] Hicks L, Dresselhaus MS. *Phys. Rev. B* 1993; 47: 16631-34.

[8] Dresselhaus MS, Chen G, Tang MY, Yang RG, Lee H, Wang DZ, et al. *Adv. Mater.* 2007; 19: 1043-53.

[9] Poudel B, Hao Q, Ma Y, Lan Y, Minnich A, Yu B, et al. *Science* 2008; 320: 634-8.

[10] Minnich AJ, Dresselhaus MS, Ren ZF, Chen G. *Energy & Environ. Sci.* 2009; 2: 466-79.

[11] Zide J, Vashaee D, Bian Z, Zeng G, Bowers J, Shakouri A, et al. *Phys. Rev. B* 2006; 74: 205335.

[12] Zebarjadi M, Joshi G, Zhu G, Yu B, Minnich A, Lan Y, et al. *Nano Lett.* 2011; 11: 2225-30.

[13] Yadav A, Pipe KP, Shtein M. *J. Power Sources* 2008; 175: 909-13.

[14] Francioso L, De Pascali C, Farella I, Martucci C, Cretì P, Siciliano P, et al. *J. Power Sources* 2011; 196: 3239-43.

[15] Dubey N, Leclerc M. *J. Polym. Sci. Part B: Polym. Phys.* 2011; 49: 467-75.

[16] Zhang K, Zhang Y, Wang S. *Sci. Rep.* 2013; 3: 3448.

[17] Bubnova O, Khan ZU, Malti A, Braun S, Fahlman M, Berggren M, et al. *Nat. Mater.* 2011;10:429-33.

[18] Hone J, Ellwood I, Muno M, Mizel A, Cohen ML, Zettl A, et al. *Phys. Rev. Lett.* 1998; 80: 1042-5.

[19] Zuev YM, Chang W, Kim P. *Phys. Rev. Lett.* 2009; 102: 096807.

[20] Tan XJ, Liu HJ, Wei J, Shi J, Tang XF, Uher C. *Carbon* 2013; 53: 286-91.

[21] Kim SL, Choi K, Tazebay A, Yu C. *ACS Nano* 2014; 8: 2377-86.
[22] Bubnova O, Crispin X. *Energy & Environ. Sci.* 2012; 5: 9345-62.
[23] Yu C, Kim YS, Kim D, Grunlan JC. *Nano Lett.* 2008; 8: 4428-32.
[24] Kim D, Kim Y, Choi K, Grunlan JC, Yu C. *ACS Nano* 2010; 4: 513-23.
[25] Hewitt CA, Kaiser AB, Roth S, Craps M, Czerw R, Carroll DL. *Nano Lett.* 2012; 12: 1307-10.
[26] Zhang B, Sun J, Katz HE, Fang F, Opila RL. *ACS Appl. Mater. Interf.* 2010; 2: 3170-8.
[27] Du Y, Shen SZ, Cai K, Casey PS. *Prog. Polym. Sci.* 2012; 37: 820-41.
[28] Yu C, Choi K, Yin L, Grunlan JC. *ACS Nano* 2011; 5: 7885-92.
[29] See KC, Feser JP, Chen CE, Majumdar A, Urban JJ, Segalman RA. *Nano Lett.* 2010; 10: 4664-7.
[30] Shakouri A, Bowers JE. *Appl. Phys. Lett.* 1997; 71: 1234-6.

Feature Articles

Effect of Nitrogen Doping on Titanium Carbonitride-Derived Adsorbents Used for Arsenic Removal

Keun Su CHOI
Computational Science Research Center
Materials and Life Science Research Division
c.keunsu@kist.re.kr

Hiroshi Mizuseki
Computational Science Research Center
Materials and Life Science Research Division
mizuseki@kist.re.kr

Jae Woo CHOI
Center for Water Resource Cycle Research
Green City Technology Institute
plead36@kist.re.kr

Summary

The removal of heavy metals from industrial wastewater is important owing to their eco-toxicity in aqueous environments. Arsenic is an especially harmful contaminant in water and wastewater as it poses serious health risks. This article describes our research concerning an efficient system for the removal of arsenic by a nitrogen-doped carbon-based material (CN). Though porous carbon material having a large surface area is a good adsorbent by itself, functionalization can enhance its adsorption capacity even further. N-doping is particularly advantageous in view of its charge and structure. Differences in the electronegativity between N and carbon and hydrogen atoms induce neighboring atoms to be charged in the N-doping process, and thus enhance adsorption reactivity. Furthermore, the structural deformation of carbon material by N-doping is moderate, since the atomic size of N and C atoms are similar. These results suggest that nitrogen-doped carbon is a promising adsorbent for the treatment of toxic anionic heavy metals, such as arsenic, from wastewater and sewage.

Introduction

There is growing global concern about the high concentration of arsenic in groundwater and its carcinogenic health effects [1]. The National

Academy of Science (NAS) and the National Research Council (NRC) have reported that even a concentration of 3 μg/L of arsenic increases the risk of bladder and lung cancer, leading to between 4 and 7 deaths per 10,000 people; extended long-term exposure to 10 μg/L of arsenic can increase this risk up to 23 deaths per 10,000 people [2]. In most countries, the maximum contaminant level (MCL) in drinking water has been established at 50 μg/L [3]; however, the World Health Organization (WHO) recommended an even lower MCL level of 10 μg/L in 1993 [4]. The U.S. Environmental Protection Agency (EPA) has recommended a standard of only 5 μg/L, a guideline which is currently used by the Department of Environmental Protection of New Jersey, U.S.A. [5].

Among the sorption materials used in the removal of arsenic, iron oxides or hydroxides have demonstrated excellent sorption characteristics and have been applied to various carbon nanomaterials [6, 7]. Typically, improvement in adsorption capacity has been realized by either decreasing the particle sizes of iron oxides or hydroxides or changing supporting agents such as carbon-based materials [7, 8], As these modification procedures can be easily optimized, intensive efforts have been focused on the development of eco-friendly, iron-based materials for the removal of arsenic; meanwhile, progress in developing chemically and thermally stable carbon for the adsorption of arsenic has been insignificant as compared to its broad and successful utilization in sorbents and energy-related materials [9, 10]. Adsorbents used for the removal of arsenic from water should not contain impurities because they can contaminate the water; in addition, they should exhibit chemical stability while removing the arsenic so as not to react with it and form by-products [11]. Hence, changing the intrinsic properties of carbon, such as by the modification of its pore structure or doping by heteroatoms such as N, S, and B, is highly desirable.

Carbide-derived carbon (CDC), prepared by the selective removal of metals from carbides, exhibits narrow pore size distribution with interconnected pores as well as a high specific surface area, typically originating from the micro-pore region [12]. These characteristics of CDC facilitate its use as a gas adsorbent and electrode material for supercapacitors. Recently, modified CDC, having dual micro- and meso-porous regions, has been synthesized by the template method followed by chlorination [13]. On account of its well-developed micro-pores, which exhibit strong interaction between the adsorbent and adsorbate, and uniform meso-pores, which facilitate the diffusion of electrolytes, it demonstrates high performance for use in lithium sulfur batteries [13].

Doping pure carbon with nitrogen makes it highly reactive, so nitrogen-doped carbon can be applied for CO_2 capture and electrocatalytic activity [14, 15]. In fact, nitrogen-doped carbon has already been applied as an adsorbent for arsenic [16, 17]. However, because nitrogen has insufficient sorption properties, it has not been thoroughly investigated in the field of arsenic capture.

In this study, we synthesized nitrogen-doped carbon by the chlorination of titanium carbonitride, $Ti(C_xN_{1-x})$, which exhibits well-developed micro- and small meso-pores with uniform pore structures. Extensive investigation was then carried out on its arsenic adsorption capacity. We found that this nitrogen-doped CDC with its unique CDC-like porosities shows promise as a new method for arsenic adsorption, even comparable to the metal oxide-carbon hybrids reported previously.

Investigation results

Properties of nitrogen-doped carbon-based materials

Samples are denoted as CNX, where X represents the chlorination temperature. Figure 1 shows the field emission-scanning electron microscopy (Fe-SEM) images of the $Ti(C_{0.7}N_{0.3})$ precursors and their corresponding CNs produced by chlorination at different temperatures. CNs retained their original angular shape and size, irrespective of temperature. This result implies that conformal-like transformation occurred, similar to that in the formation

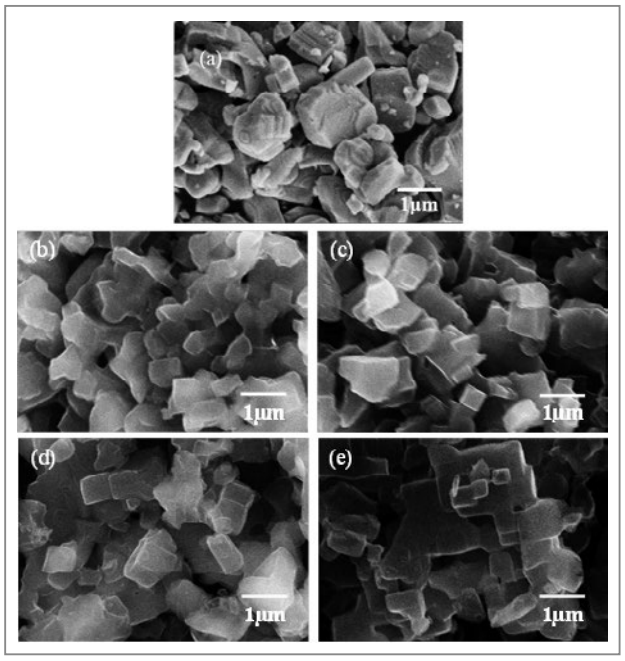

Figure 1. Fe-SEM images of $Ti(C_{0.7}N_{0.3})$ precursors (a) and their corresponding CN700 (b), CN800 (c), CN900 (d), and CN1000 (e).

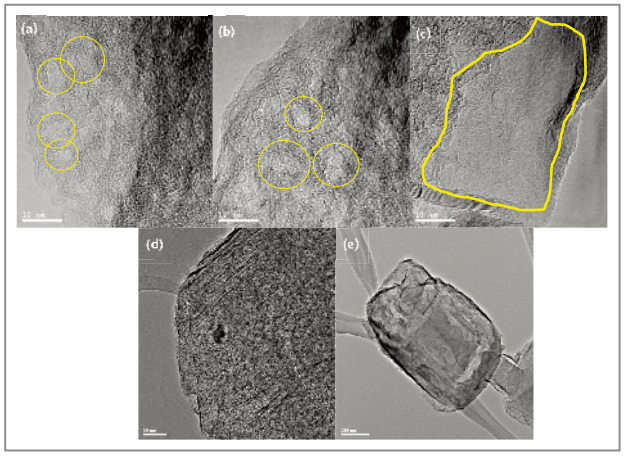

Figure 2. Transmission electron microscopy (TEM) images of CN700 (a), CN800 (b), CN900 (c), CN1000 (d), and CN1000 (e). Small meso-pores are represented as circles in (a) and (b). Larger pores are observed in (c).

of CDC [18, 19]. Figure 2 shows the transmission electron microscopy (TEM) images of CNs. The ones shown in Figures 2(a) and 2(b) feature small sized meso-pores developed by curved graphitic layers. With the increase of synthesis temperature, the pores incorporated

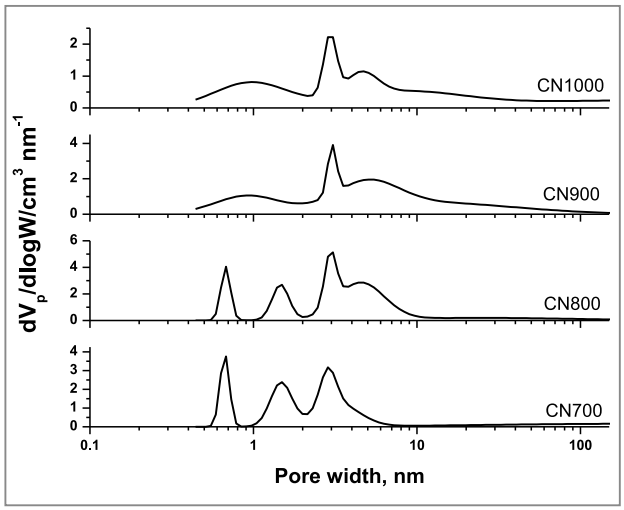

Figure 3. Pore size distribution (PSD) of CNs calculated by NLDFT (cylinder pore model).

into the stretched ones shown in Figure 2(c). In CN1000, stretched layers were highly stacked at the boundary of the particles (Figures 2(d) and (e)).

As shown in Figure 3, the pore size distribution (PSD) of CNs, which is calculated by the non-local density functional theory (NLDFT), varies with chlorination temperature. The pore size of CN700 was centered at 0.7 nm, which is a characteristic of TiC-derived carbon [20]. Meanwhile, those of 1.5 nm and 3.0 nm are believed to be affected by CN_x desorption [21]. CN700 exhibited a uniform tri-modal distribution, depicted in Figure 3, and spherical pores, as shown in Figures 2(a) and 2(b). With the increase of synthesis temperature, the pores centered at 0.7 nm and 1.5 nm collapsed because of the high stress caused by the curved graphitic layer, thereby leading to irregularity. In the case of CN1000, large pores with a diameter of 20–100 nm were well developed, but the total pore volume was less than the other CNs tested.

Figure 4(a) shows the X-ray diffraction (XRD) spectra of the synthesized CNs. Sharp (002) and broad (10) peaks were observed, which are characteristic of turbostratic structure [22]. A sharp shoulder peak from CN700, observed around 26~27°, represents well-crystallized carbon layers [23]. This is further verified from Raman

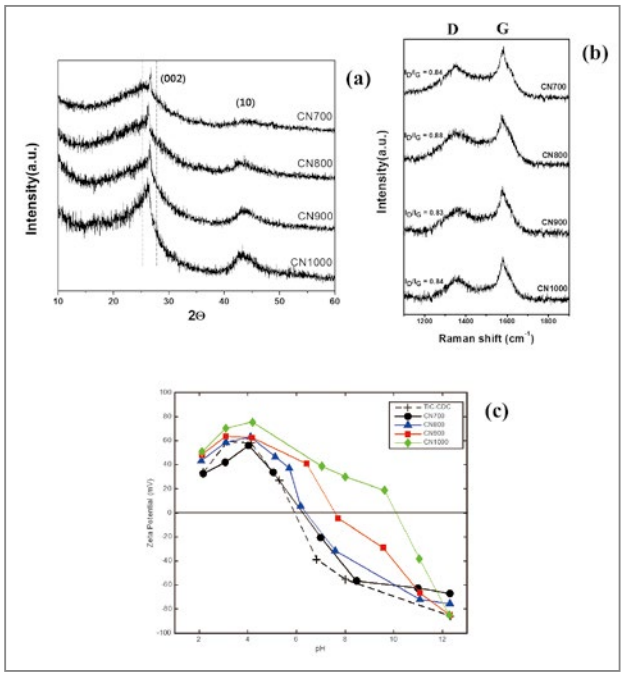

Figure 4. (a) X-ray diffraction (XRD) spectra of CNs featuring a turbostratic carbon structure. (b) Raman spectroscopy of CNs with the I_D/I_G ratio. (c) Zeta potential measurement for CNs.

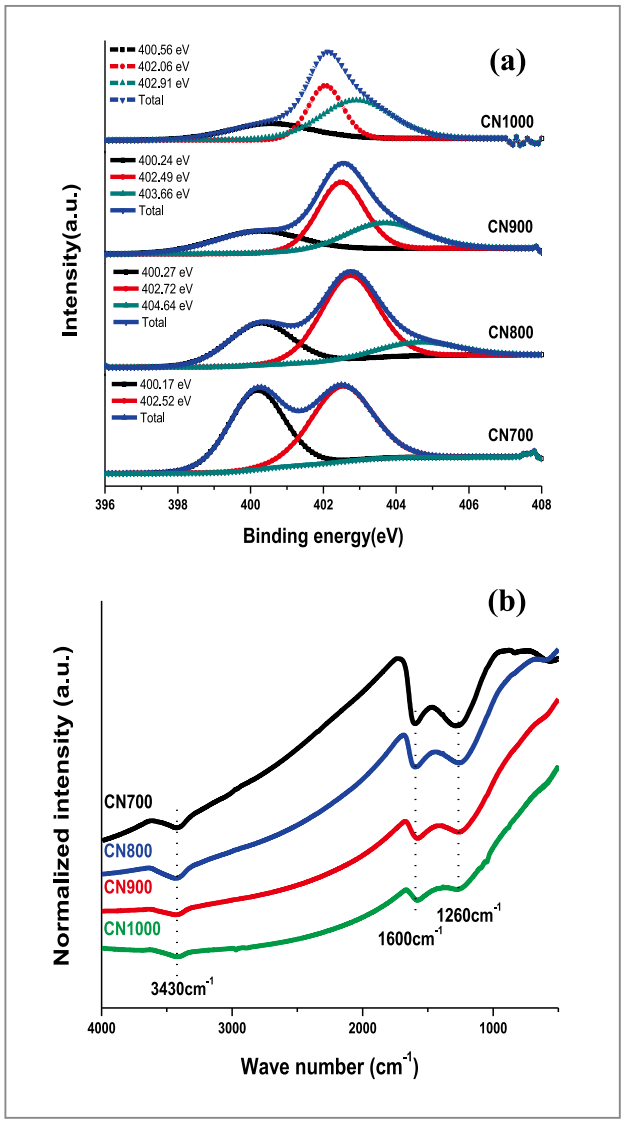

Figure 5. X-ray photoelectron spectroscopy (XPS) spectra (a) and Fourier Transform infrared spectroscopy (FTIR) (b) of CN700, CN800, CN900, and CN1000.

spectroscopy (Figure 4(b)) where I_D/I_G values, which are used to evaluate the defect degree of graphene, are much lower than that of TiC-CDC [24]. Porous carbon derived from pure TiC requires temperatures greater than 1200°C to be well graphitized [25], whereas titanium carbonitride-derived carbons show much higher graphitization even from 700°C due to CN_x decompositions, which seem to catalyse the graphitization. Zeta potential measurements were performed on CNs and TiC-CDC. As shown in Figure 4(c), the zeta potential of all the powders was strongly related to pH values. At low pH, the particles were positively charged by protonation, which is beneficial for attracting the anionic metal complexes.

In contrast, the particles were negatively charged at high pH. The isoelectric points (pH_{PZC}), where the zeta potential is zero, of TiC-CDC, CN700, CN800, CN900, and CN1000 were pH 5.9, 6.3, 6.4, 7.6, and 10.1, respectively. In CNs, as synthesized temperature increased, these values also increased. This comes from the basicity of carbon, which could be attributed to the π-electrons on the graphitic basal planes, and/or basic oxygen functional groups [26].

X-ray photoelectron spectroscopy (XPS) spectra (Figure 5(a)) were recorded for the comparison of the chemical composition and bonding properties of CNs produced by chlorination at different temperatures.

Table 1. Chemical composition of CNs synthesized at different temperatures, as measured by XPS. The bulk compositions of nitrogen, oxygen, and hydrogen obtained by EA have been shown within parenthesis.

Samples	C (wt%)	N (wt%)	O (wt%)	H (wt%)
CN700	80.77	3.14 (13.43)	14.71 (6.14)	1.64
CN800	84.24	3.72 (9.44)	10.71 (4.17)	1.26
CN900	84.08	2.67 (6.70)	12.78 (2.89)	0.73
CN1000	84.67	2.17 (4.55)	16.65 (1.27)	0.36

Table 1 summarizes the XPS data. CN700, CN800, CN900, and CN1000 exhibited nitrogen content of 3.14 wt%, 3.72 wt%, 2.67 wt%, and 2.17 wt%, respectively. The 1s peak of nitrogen was deconvoluted into two types of configuration: pyrrolic-N (400.37 0.2 eV) and oxidized-N (402–404 eV), which mainly consists of N-oxides of pyridinic-N (402.060.3 eV) [27]. Given that these functional groups were invariably located at the edges [27], the synthesized CNs seem to consist of a large amount of edges caused by the development of pores [28]. As indicated by elemental analysis (EA) which identifies the bulk composition, nitrogen content in the synthesized CNs was higher than that observed from XPS analysis. Because the surface can easily be contaminated by oxygen, the relative nitrogen content at the surface decreased. On the other hand, a previous study has demonstrated that pores in CDC develop not only at the surface but also throughout its bulk [28]. Moreover, edges along the pore growth of the bulk seem to be desired sites for an edged-nitrogen doping. Micro-pores are formed in pure carbide systems, while micro- and meso-pores are formed in carbonitride systems. Pores grow as a result of the decomposition of unstable C–N bonds, such as pyrrolic-N (5-membered ring), while stable nitrogen bonds, such as pyridinic- or graphitic-N (6-membered ring), are retained, or unstable bonds are converted to stable bonds on the pores [29].

Applicability of CN for the treatment of arsenic-contaminated water

The applicability of CNs for the treatment of arsenic-contaminated water was investigated by performing equilibrium batch adsorption tests. The arsenic adsorption isotherms of CNs are shown in Figure 6. CN700 exhibited a non-linear adsorption isotherm for the removal of arsenic. CN800 also exhibited a non-linear adsorption isotherm; however, the concentration of arsenic adsorbed on CN800 was lower than that adsorbed on CN700. CN900 adsorbed very little arsenic in low arsenic concentrations On the other hand, CN1000 did not adsorb arsenic. This difference in the removal of arsenic among the CNs is probably related to their pore structure and surface functional groups. In light of the reasonable adsorption isotherms of CN700 and CN800, it seems that having micro-pores of 0.7 nm and a high content of N are the reasons for higher As adsorption as compared with CN900 and CN1000. To compare the arsenic adsorption properties of CNs with that of a

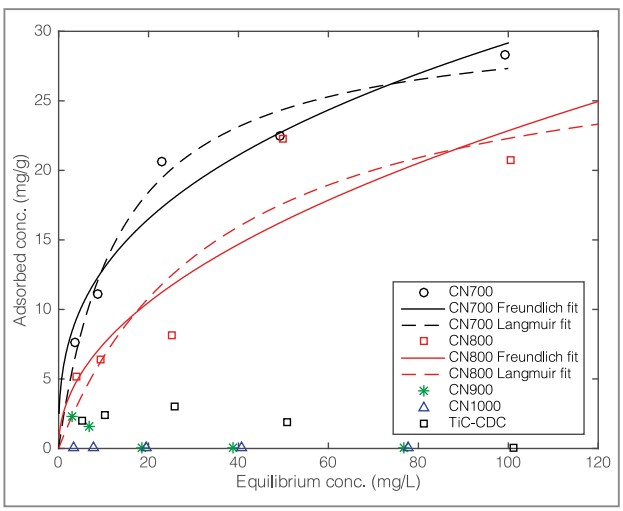

Figure 6. Comparison of adsorption isotherms of As on CNs (700, 800, 900, and 1000°C) and typical CDC (TiC-CDC).

typical CDC, an equilibrium adsorption test was also performed using TiC-CDC. The adsorption of arsenic on TiC-CDC was not significant, probably related to the negligible meso-pores and/or the absence of nitrogen functional groups. It is worth noting that CNs have shown much better As adsorption than that of activated carbon modified by polyaniline [30].

Adsorption mechanism of arsenic ion on CNs

We performed first principles calculations based on density functional theory to reveal the adsorption mechanism of As(V) ion on N-doped carbon material. We adopted circum-coronene (CC), which consists of 54 carbon and 18 hydrogen atoms in its pristine form as adsorbent. We prepared two N-doped adsorbents which contained pyridine N-Oxide (NO) and pyrrolic N (NH) functional groups, based on the XPS spectrum in Figure 7(a) and N-free (NF) CC as a reference, as shown in Figure 8. Comparing adsorption processes in adsorbents with and without N atoms would be useful to reveal the role of N atoms in adsorption of As(V) ions. Adsorption was evaluated by the difference of free energies, $\Delta G = G_{adsorbent + adsorbate} - (G_{adsorbate} + G_{adsorbent})$. The free energy is defined as $G = H - T \times S + ZPE$, where H, $T \times S$, and ZPE denote the enthalpy, product of temperature and entropy, and zero-point energy, respectively. All configurations were optimized by full relaxation with DFT calculations, and free energies were obtained for pre-optimized configurations using GAUSSIAN 09. Since the adsorption must take place in aqueous environments in the real world, considering the relative ΔG is more reasonable than the absolute ΔG. If we set ΔG in NF-CC to zero, relative ΔGs of NO-CC and NH-CC are 0.16 and 0.67 eV, respectively. Introducing pyrrolic N enhances binding strength between As(V) and adsorbent. These theoretical results are consistent with our experimental results whereby the content of pyrrolic N in Figure 6 is proportional to the adsorption capacity of As(V), as shown in Figure 6.

Figure 8 shows the optimized structures of As(V) on pyrrolic N and carbon plane that is located above the pyrrolic N without covalent bonding. Since As(V) is adsorbed on pyrrolic N by electrostatic interaction, we analyzed the amount of charges on each atom by using the Mulliken population method. Four oxygen atoms in As(V) complex, $[H_2AsO_4]^{-1}$, are negatively charged and the other atoms, two H and As, are positively charged. In Figure 8(a), two C atoms and an H atom, which are connected to the pyrrolic N atom, are positively charged with 0.31e, 0.33e, and 0.35e, while pyrrolic N is negatively charged with −0.71e. Therefore, the electrostatic interaction between these three positively

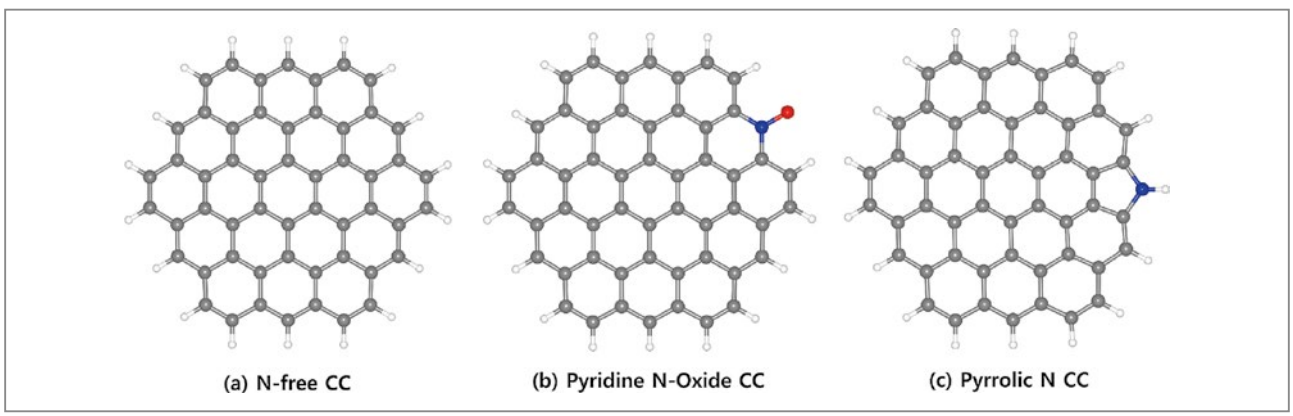

Figure 7. Three adsorbents are prepared from circumcoronene (CC), which consists of 54 carbons and 18 hydrogen atoms: (a) N-free, (b) pyridine N-oxide (NO), and (c) pyrrolic N (NH) CC. Two N-doped adsorbents, NO-CC and NH-CC, were adopted based on the XPS spectra, 402.06 ± 0.3 eV and 400.37 ± 0.2 eV, in Figure 5(a). Gray, white, blue, and red balls represent carbon, hydrogen, nitrogen, oxygen and arsenic atoms, respectively.

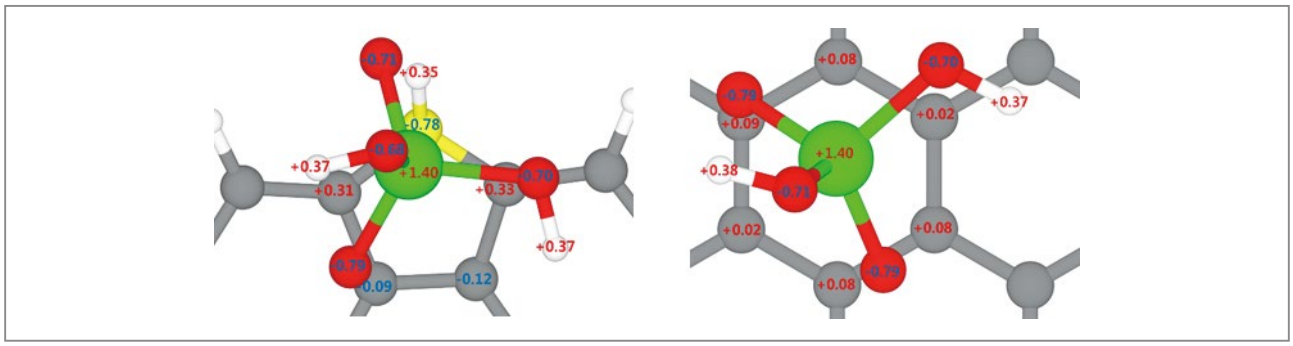

Figure 8. Two optimized structures of As(V) on pyrrolic N and carbon plane. Plus (negative) represents the deficiency (abundance) of electrons.

charged atoms in adsorbent and negatively charged O atoms in the As(V) complex causes As(V) to be adsorbed on pyrrolic N. Comparing charge distributions of the two configurations clearly shows the role of pyrrolic N on adsorption of As(V). Though the charge amount of the O atoms in As(V) are similar in both configurations, C atoms in carbon plane are nearly neutral and the electrostatic interaction between As(V) and carbon plane is not sufficiently strong to bind it. These theoretical results are consistent with experimental results, which indicate that the sample without an N atom (TiC-CDC) does not adsorb As(V). Consequently, pyrrolic N in carbon-based material makes neighboring atoms positively charged, thereby reinforcing electrostatic interactions between As(V) and the adsorbent.

Conclusions

We synthesized nitrogen doped carbon (CNs) by simple chlorination of $Ti(C_{0.7}N_{0.3})$ at various temperatures and demonstrated their potential applicability for treatment of arsenic-contaminated water. With chlorinated $Ti(C_{0.7}N_{0.3})$, CNs developed nitrogen functional groups on the edges, including pyrrolic-N (PN) and pyridinic N-Oxide (NO). Among the synthesized CNs, CN700 showed the highest maximum adsorption capacity of 31.08 mg/g. This remarkable removal capacity is mainly attributed to pyrrolic-N, which imparts positive charges to adjacent carbon and hydrogen atoms, binding arsenic complex, $H_2AsO_4^{-1}$, through electrostatic interaction. In addition, well-developed micro-pores served as active sites for arsenic adsorption while small meso-pores boosted the rapid diffusion of arsenic complex in water due to the unique conformal reaction of chlorination. These results suggest that CNs may serve as important adsorbents for the removal of arsenic in wastewater. Further enhancement in adsorption may also be possible through the synergetic effect of hybridization between CNs and iron oxides/hydroxides.

Note

This article and images are drawn from "Effect of nitrogen doping on titanium carbonitride-derived adsorbents used for arsenic removal" in *Journal of Hazardous Materials*, vol. 302, pp 275~385.

References

[1] Smedley PL, Kinniburgh DG. *Appl. Geochem.* 2002; 17: 517-568.

[2] United States Congress, House Committee on Science, Subcommittee on Environment Technology and Standards. *Arsenic in drinking water: an update on the science, benefits, and cost*; October 4, 2001.

[3] An B, Kim H, Park C, Lee SH, J.W. Choi JW. *J. Hazard Mater.* 2015; 289: 54-62.
[4] World Health Organization (Ed.). *WHO Guidelines for Drinking Water Quality: Recommendations vol. 1*; Geneva, 1993.
[5] Xia Y, Mokaya R. *Advanced Materials* 2004; 16: 1553-1558.
[6] Chen W, Parette R, Zou J, Cannon FS, Dempsey BA. *Water Res.* 2007; 41: 1851-1858.
[7] Chandra V, Park J, Chun Y, Lee JW, Hwang IC, Kim KS. *ACS Nano* 2010; 4: 3979-3986.
[8] Mayo JT, Yavuz C, Yean S, Cong L, Shipley H, Yu W, Falkner J, Kan A, Tomson M, Colvin VL. *Sci. Technol. Adv. Mat.* 2007; 8: 71-75.
[9] Vix-Guterl C, Frackowiak E, Jurewicz K, Friebe M, Parmentier J, Beguin F. *Carbon* 2005; 43: 1293-1302.
[10] Sun YQ, Wu QO, Shi GQ. *Energ. Environ. Sci.* 2011; 4: 1113-1132.
[11] Mohan D, Pittman CU. *J. Hazard. Mater.* 2007; 142: 1-53.
[12] Chmiola J, Largeot C, Taberna PL, Simon P, Gogotsi Y. *Science* 2010; 328: 480-483.
[13] Lee JT, Zhao Y, Thieme S, Kim H, Oschatz M, Borchardt L, Magasinski A, Cho WI, Kaskel S, Yushin G. *Adv. Mater.* 2013; 25: 4573-4579.
[14] Gong K, Du F, Xia Z, Durstock M, Dai L. *Science* 2009; 323: 760-764.
[15] Hao GP, Li WC, Qian D, Lu AH. *Adv. Mater.* 2010; 22: 853-857.
[16] Saada A, Breeze D, Crouzet C, Cornu S, Baranger P. *Chemosphere* 2003; 51: 757-763.
[17] Yang L, Wu SN, Chen JP. *Ind. Eng. Chem. Res.* 2007; 46: 2133-2140.
[18] Gogotsi Y, Nikitin A, Ye H, Zhou W, Fischer JE, Yi B, Foley HC, Barsoum MW. *Nat. Mater.* 2003; 2: 591-594.
[19] Kim J, Han J, Ha D, Kang S. *J. Mater. Chem. A* 2014; 2: 16645-16651.
[20] Yushin G, Dash R, Jagiello J, Fischer JE, Gogotsi Y. *Adv. Funct. Mater.* 2006; 16: 2288-2293.
[21] Seo MS, Kim JH, Kim JM, Han JS, Kang S, Ihm JS, Kim DO. *Carbon* 2013; 60: 299-306.
[22] Leis J, Perkson A., Arulepp M, Kaarik M, Svensson G. *Carbon* 2001; 39: 2043-2048.
[23] Hou J, Cao C, Idrees F, Ma X. *ACS Nano* 2015; 9: 2556-2564.
[24] Chmiola J, Yushin G, Gogotsi Y, Portet C, Simon P, Taberna PL. *Science* 2006; 313: 1760-1763.
[25] Dash R, Chmiola J, Yushin G, Gogotsi Y, Laudisio G, Singer J, Fischer J, Kucheyev S. *Carbon* 2006; 44: 2489-2497.
[26] Li M, Wang C, O'Connell MJ, Chan CK. *Environ. Sci. Nano* 2015.
[27] Lai L, Potts JR, Zhan D, Wang L, Poh CK, Tang C, Gong H, Shen Z, Lin J, Ruoff RS. *Energ. Environ. Sci.* 2012; 5: 7936.
[28] Palaniselvam T, Aiyappa HB, Kurungot S. *J. Mater. Chem.* 2012; 22: 23799-23805.
[29] Pels JR, Kapteijn F, Moulijn JA, Zhu Q, Thomas KM. *Carbon* 1995; 33: 1641-1653.
[30] Yang L, Wu S, Chen JP. *Ind. Eng.Chem. Res.* 2007; 46: 2133-2140.

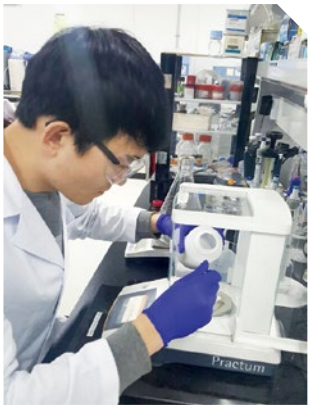

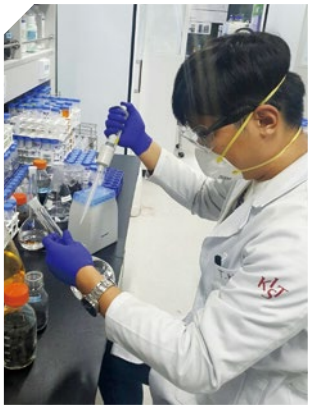

Feature Articles

Anion Exchange Membrane Water Electrolyzer with an Ultra-Low Loading of Pt-Decorated Ni Electrocatalyst

Jong Hyun JANG
Fuel Cell Research Center
National Agenda Research Division
jhjang@kist.re.kr

Introduction

The development of alternative energy technologies in place of conventional fossil fuel-based energy systems is considered essential in this era of global climate change. To this end, renewable energy sources, such as wind and solar power, are expected to supply sustainable electricity in the near future. At the same time, large-scale energy storage systems must be developed to address imbalances that can occur between energy supply and energy consumption. Electrolysis technology that can electrochemically convert electricity to CO_2-free hydrogen is one of the developments that has been attracting considerable attention in recent years [1, 2]. Using an electrochemical cell called an electrolyzer, liquid water can be dissociated into oxygen and hydrogen gases through concurrent electrochemical half-reactions: hydrogen evolution reactions (HERs) and oxygen evolution reactions (OERs). When the electricity is stored in the form of hydrogen, the hydrogen loss, which is equivalent to the self-discharge in rechargeable batteries, is very small, enabling long-term high efficiency and high capacity energy storage. In addition, the hydrogen produced by electrolyzers can be transformed to valuable chemicals or transported economically through pipelines or tanker trucks.

For several decades, development has concentrated primarily on two types of electrolyzers: alkaline water electrolyzers (AWEs) [3] and proton exchange membrane water electrolyzers (PEMWEs) [4, 5]. AWEs

utilize liquid alkaline solutions with porous diaphragm separators as electrolytes while PEMWEs rely on proton exchanging membranes (PEMs) for the electrolyte function. Regarding the electrocatalysts' performance with OER and HER, AWEs operate at basic conditions (high pH) and can thus utilize non-noble metals, making them cost effective [6], whereas PEMWEs require expensive novel metals such as Pt and Ir to withstand their highly acidic environment. However, PEMWEs have other advantages, including higher H_2 purity, ability to operate at elevated pressures, and rapid startup/shutdown due to the use of solid electrolyte (PEM) with lower gas crossover and ohmic resistance [4, 5, 7, 8] compared to AWEs that have a porous diaphragm with a large gap between two electrodes [9].

Recent research has been done on another alternative technology, anion exchange membrane water electrolyzers (AEMWEs), in which hydroxide ion (OH^-) conducting polymer membranes are utilized [10-22]. AEMWEs are expected to combine the advantages of AWEs (non-noble metal electrocatalysts) and PEMWEs (high H_2 purity, pressurized operation, load variation, etc.). However, further research in both hydroxide ion conducting polymer membranes and electrocatalysts is still required to develop more durable and inexpensive systems. AEMWEs are conventionally fabricated by preparing porous electrodes composed of catalyst powder and ionomers/binders [10-18]. It should be noted that for various electrocatalysts, such as Co-based oxides [10, 11, 13, 15, 18], IrO_2 [12], Ni-Fe [14], and Ni/(CeO_2-La_2O_3)/C [17], high metal loading of a few mg/cm^2 is required in order to achieve reasonable performance. As they typically have a thickness of several micro-meters, conventional porous electrodes are not effective at reactant/product transport, resulting in low utilization of electrocatalysts.

In order to resolve the problems of conventional AEMWE electrodes, our team at KIST has developed and reported on a new technique to design particle-type electrodes where Ni particles are fabricated by electrodeposition on carbon paper (CP) [23]. The performance of our cell was 150 mA/cm^2 at 1.9 V, despite the extremely small amount of Ni nanoparticle catalyst present (8.51 μg_{Ni}/cm^2). The relatively high performance of our cell was probably due to minimized ohmic resistance, high catalyst utilization, and rapid transportation. It is worth noting that electrodeposition has its own merits as an electrode fabrication method because it involves a simple process with short processing time. However, the lack of active sites created from small loadings still limits cell performance and restricts the practical application of these cells. In order to increase the performance of particle-type electrodes, we demonstrate in the present study an electrochemical modification of the electrodeposited Ni nanoparticles through Ni displacement by Pt. While maintaining extremely small catalyst loadings and corresponding benefits, a simple displacement of the Ni surface with Pt is expected to significantly increase cell performance due to the intrinsically high HER activity of Pt in alkaline electrolytes [24]. The effects of changes in morphology and composition of the Pt-decorated Ni particles as well as the synergetic effect between Ni and Pt on HER activity are discussed below.

Ni/CP: Ni electrocatalysts electrodeposited on carbon papers (CP)

Particle-type electrodes were fabricated by Ni electrodeposition on CP. The number of Ni electrocatalysts and their morphologies could be varied by controlling the deposition potential and time. Considering the combined effect of electrodeposition potential on Ni deposition and water dissociation to produce H_2, this study determined the optimum condition to be -0.95 V deposition potential. At a fixed potential of -0.95 V, the Ni/CP electrodes were fabricated with controlled deposition time. Figure 1 shows the

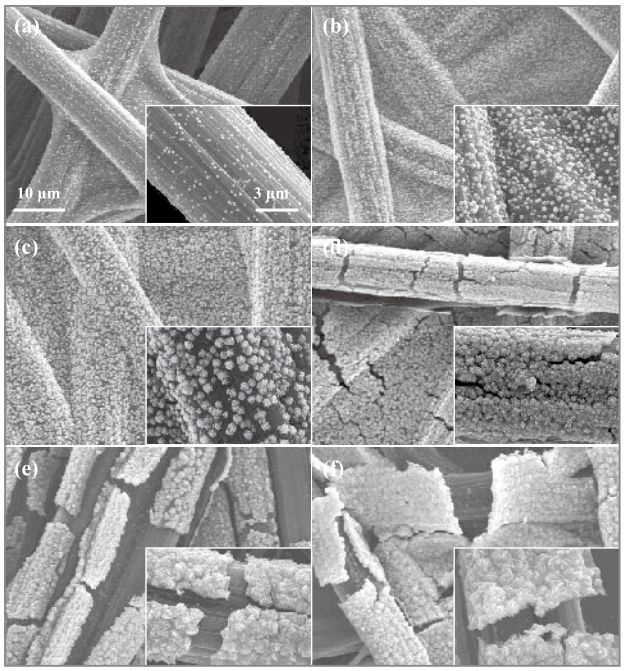

Figure 1. FESEM images of Ni/CPs at: (a) 5 s, (b) 20 s, (c) 50 s, (d) 60 s, (e) 180 s, and (f) 300 s. The deposition potential was fixed at -0.95 V.

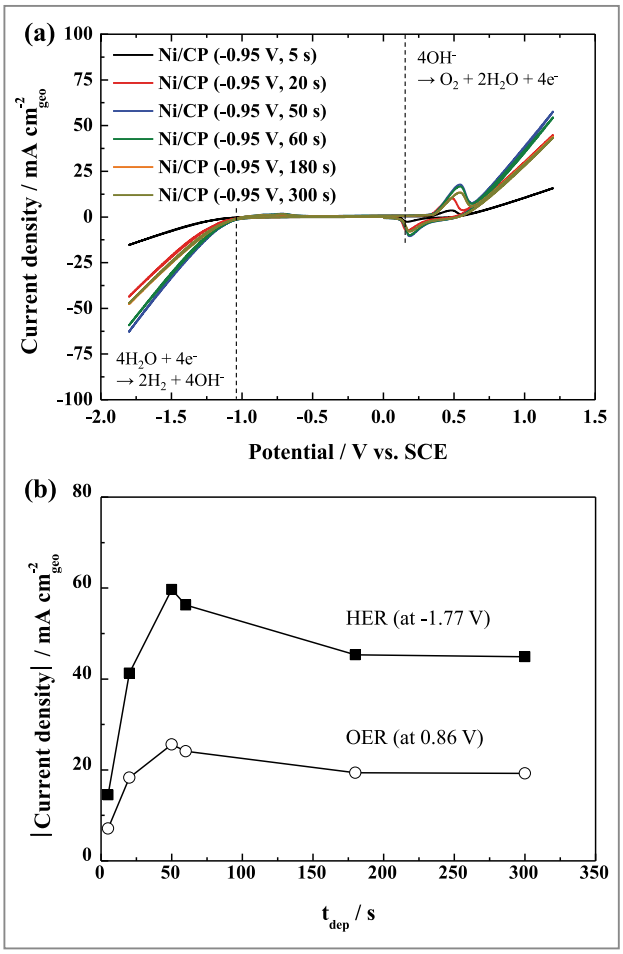

Figure 2. (a) CV curves for Ni/CPs (50 mV/s, 1.0 M KOH). (b) Current densities at an overpotential of 0.70 V for Ni/CPs with various deposition times.

morphology evolution with deposition time, while the Ni loading was varied from 1.0 μg/cm^2 (5 s) to 9.8 μg/cm^2 (60 s) and then further increased to 21.6 μg/cm^2 (300 s) with a time increase from 5 to 300 s. Under a short deposition time of 5 s, isolated Ni particles developed (Figure 1a) and gradually increased in size up to 50 s (Figures 1b and 1c). With further electrodeposition, cracks in electrodeposited Ni layers gradually developed (Figure 1d), resulting in peeling off (Figures 1e and 1f).

The electrocatalytic activities of prepared Ni/CP electrodes were analyzed by cyclic voltammetry (CV) in 1.0 M KOH solutions (Figure 2a), and the current densities at -1.77 V and 0.86 V, which represent the HER and OER activity, respectively, were plotted as a function of deposition time (Figure 2b). The HER and OER activities both increased with deposition time up to 50 s and then decreased with further deposition. This tendency correlated well with the actual surface area variation with deposition time, indicating that surface area is the dominant factor in particle-type Ni/CP electrodes.

Then the Ni/CP electrodes, which were prepared by electrodeposition at -0.95 V for 50 s, were assembled to make AEMWE single cells to evaluate AEMWE performance. At a cell voltage of 1.9 V, the current densities were 150 and 280 mA/cm^2 when the 1.0 M KOH feed was supplied to only cathode and both electrodes, respectively. It should be noted that the loading of Ni electrocatalysts was extremely low (8.51 μg/cm^2), but cell performance was comparable to previous reports [10-15, 18-22].

Pt-Ni/CP: Pt-decorated Ni electrocatalysts

Pt-decorated Ni electrocatalysts (Pt-Ni/CP) were fabricated by incorporating Pt atoms on Ni/CP electrodes (Figure 3a) through Ni displacement in 1 mM K_2PtCl_6 solution with varying HCl concentrations. Figures 3b-d show the SEM images of Pt-Ni/CP-1, Pt-Ni/CP-2, and Pt-Ni/CP-3, where the HCl concentrations are 10 mM, 50 mM, and 100 mM, respectively. Compositional changes of Pt-Ni/CP electrodes were analyzed by electron probe micro analyzer (EPMA) mapping, as shown in Figure 4. With increasing HCl concentration, a gradual increase of Pt content could be confirmed (bottom images), which was accompanied by a decrease of Ni content (top images). In the case of Pt-Ni/CP-3, which experienced the highest concentration of HCl, Ni particles were almost fully removed, which was in accordance with the field emission secondary electron microscopy (FESEM) images (Figure 3d). The Pt loading proportionally increased with the HCl concentration up to 3.88 μg/cm^2 as a result of the spontaneous displacement of Ni by Pt due to differences in the reduction potential of Ni^{2+}/Ni (-0.257 V_{SHE}) and $PtCl_6^{2-}$/Pt (0.744 V_{SHE}) [25]. The Pt weight ratio was estimated to gradually increase as

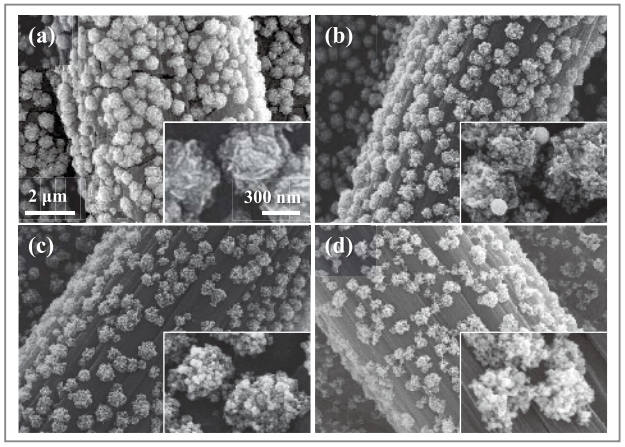

Figure 3. FESEM images of the (a) Ni/CP, (b) Pt-Ni/CP-1, (c) Pt-Ni/CP-2, and (d) Pt-Ni/CP-3 electrodes, together with the enlarged images in insets.

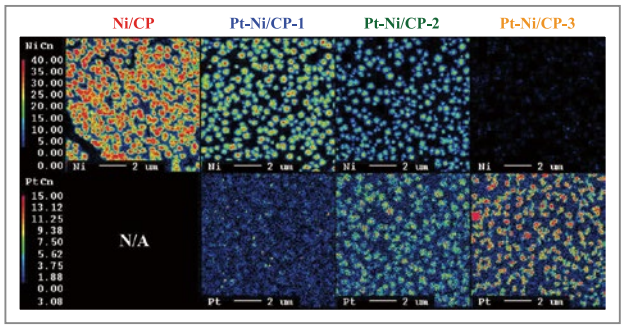

Figure 4. EPMA mapping for Ni (top) and Pt (bottom) atoms of the Ni/CP and Pt-Ni/CP electrodes.

follows: 6.8 % (Pt-Ni/CP-1) → 39.4 % (Pt-Ni/CP-2) → 89.6 % (Pt-Ni/CP-3).

$$3Ni/CP + PtCl_6^{2-} \rightarrow Pt{-}Ni/CP + 2Ni^{2+} + 6Cl^{-} \quad (1)$$

It is important to note that, as clearly shown in Pt-Ni/CP-2, the Pt and Ni signals are well matched, confirming the selective Pt decoration (Figure 4). The enlarged EPMA mapping for a particle (Figures 5a and 5b) also clearly indicates that the Pt signals were well matched with the boundary of Ni signals. The line profiles in Figure 5c prove that Ni particles were effectively

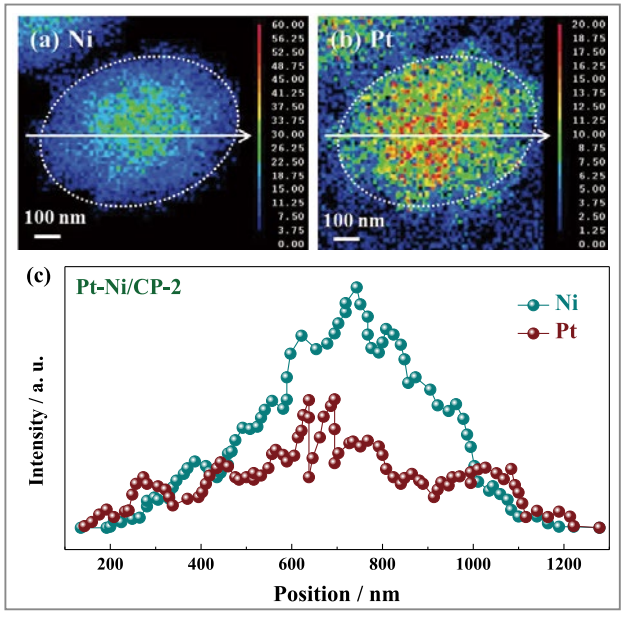

Figure 5. (a) Ni and (b) Pt mappings for a single Pt-Ni particle on the Pt-Ni/CP-2 electrode. (c) Elemental line scanning of Ni and Pt.

decorated by Pt atoms. Accordingly, with higher HCl concentration, the intensity of Ni $2p_{3/2}$ and Ni 3p decreased, whereas that of Pt 4f spectra largely increased. Quantitative analysis shows that the Pt molar ratio in XPS analysis, which is surface sensitive, is significantly larger than the bulk Pt content measured by ICPMS. For example, the Pt molar ratio of Pt-Ni/CP-2 was 63.6 % by XPS and 16.4 % by ICPMS. This result also supports selective Pt decoration on the Ni surface.

AEMWE half-cell and single cell performance of Pt-Ni/CP electrodes

Figure 6 shows the CV curves of Pt-Ni/CP electrodes in a 1.0 M KOH electrolyte solution. In the cases of Ni/CP (no Pt decoration) and Pt-Ni/CP-1, redox/oxidation peaks for surface Ni oxidation, β-$Ni(OH)_2 \leftrightarrow NiOOH$, clearly appeared at 1.25 V_{RHE} and 1.60 V_{RHE}, respectively [26]. However, such redox peaks were not observed for Pt-Ni/CP-2 and Pt-Ni/CP-3 as the Pt became the dominant component at the particle surface. In addition, it could be confirmed that the HER activity of Pt-Ni/CP-2 was enhanced to -73.7 mA/cm^2 at -0.70 V_{RHE}, while that of untreated Ni/CP was -59.4 mA/cm^2. This can be explained by the effect of synergic interaction between

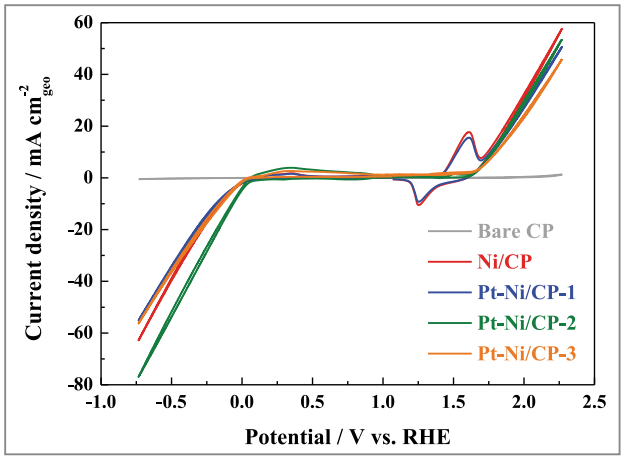

Figure 6. CV curves of the bare CP, Ni/CP, and Pt-Ni/CP electrodes (50 mV/s, 1.0 M KOH).

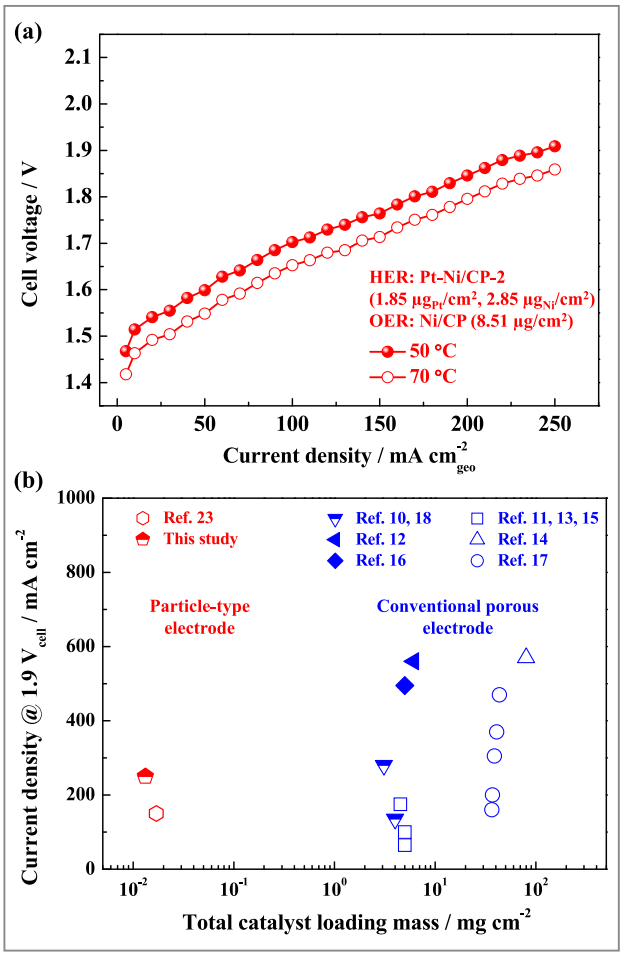

Figure 7. (a) AEMWE polarization curves of an MEA with Pt-Ni/CP-2 electrode at 50°C and 70°C. (b) Summary of AEMWE current densities at 1.9 V (open: non-noble metal only, half-open: non-noble + noble metals, solid: noble metal only).

neighboring Pt and Ni. Previously, Markovic et al. reported a similar effect for Pt surface with neighboring $Ni(OH)_2$ nanoclusters [27, 28]. It should be noted that significant HER enhancement was not observed for Pt-Ni/CP-1 (-52.1 mA/cm^2) and Pt-Ni/CP-3 (-53.4 mA/cm^2), indicating surface composition dependency.

Figure 7a shows the polarization curves for an MEA with Pt-Ni/CP-2 in the cathode at 50 and 70°C. At an AEMWE cell voltage of 1.9 V, the current density for Pt-Ni/CP-2 (250 mA/cm^2) was significantly higher than that for Ni/CP (150 mA/cm^2) (50°C), even though the added Pt amount was only 1.85 μg/cm^2. Further enhancement

in AEMWE performance could be made at increased cell temperature (70°C).

In Figure 7b, the AEMWE performance of the Pt-Ni/CP-2 electrode, as reflected by the current density at a cell voltage of 1.9 V, is compared with previously reported data [10-18, 23]. It is clearly apparent that the single cell performance in this study was comparable to previous reports in which catalyst loading was more than 100 times higher. On the other hand, several previous studies showed higher current density in AEMWE operation, but their catalyst loading measurements were very high: 43 ~ 80 mg/cm^2 (blue circle, open) [14, 17] and 5.0 or 6.1 mg/cm^2 (blue solids) [12, 16]. Therefore, it can be concluded that the Pt-Ni/CP electrodes, which are newly developed particle-type electrodes, have significant advantages in terms of electrocatalyst material cost for AEMWE applications. This superior performance with the ultra-low loading of electrocatalysts likely stems from the easy removal of generated hydrogen and oxygen bubbles, and more performance increase is expected through further optimization [23, 29, 30].

Conclusions

Ni/CP electrodes fabricated by electrodeposition processing show very good AEMWE performance even though metal loading is very low (17.0 μg/cm^2). Thin electrodes with open structures seem to be beneficial in gas generating reactions. Our team looked for a way to further enhance electrocatalytic activity by partially displacing the electrodeposited Ni with Pt to make Pt-decorated Ni electrocatalysts. When the HCl concentration was varied, the Pt-Ni/CP-2 electrode, which had ultra-low Pt loading of 1.85 μg/cm^2, showed the highest catalytic activity in respect to HER. This activity enhancement was considered to originate from the development of Pt and Ni neighboring sites, which are active sites for water dissociation. In the AEMWE single cell test, the MEA with a Pt-Ni/CP-2 electrode in the cathode delivered 250 mA/cm^2 at 50°C, a 70% performance enhancement compared to untreated Ni/CP electrodes.

Note

This article and images are drawn from "Development of a membrane electrode assembly for alkaline water electrolysis by direct electrodeposition of nickel on carbon papers" in *Appl. Catal. B* (2014), Vol. 154-155, pp. 197-205, and "Anion exchange membrane water electrolyzer with an ultra-low loading of Pt-decorated Ni electrocatalyst" in *Appl. Catal. B* (2016), Vol. 180, pp. 674-679.

References

[1] Holladay JD, Hu J, King DL, Wang Y. *Catal. Today* 2009; 139: 244-260.

[2] Christopher K, Dimitrios R. *Energy Environ. Sci.* 2012; 5: 6640.

[3] Schiller G, Henne R, Mohr P, Peinecke V. *Int. J. Hydrogen Energy* 1998; 23: 761-765.

[4] Goñi-Urtiaga A, Presvytes D, Scott K. Int. *J. Hydrogen Energy* 2012; 37: 3358-3372.

[5] Aricò AS, Siracusano S, Briguglio N, Baglio V, Di Blasi A, Antonucci V. *J. Appl. Electrochem.* 2012; 43: 107-118.

[6] Zeng K, Zhang D. *Prog. Energy Combust. Sci.* 2010; 36: 307-326.

[7] Grigoriev S, Porembsky V, Fateev V. *Int. J. Hydrogen Energy* 2006; 31: 171-175.

[8] Ito H, Maeda T, Nakano A, Takenaka H. *Int. J. Hydrogen Energy* 2011; 36: 10527-10540.

[9] Marini S, Salvi P, Nelli P, Pesenti R, Villa M, Berrettoni M, Zangari G, Kiros Y. *Electrochim. Acta* 2012; 82: 384-391.

[10] Wu X, Scott K. *J. Mater. Chem.* 2011; 21: 12344.

[11] Cao Y-C, Wu X, Scott K. *Int. J. Hydrogen Energy* 2012; 37: 9524-9528.
[12] Leng Y, Chen G, Mendoza AJ, Tighe TB, Hickner MA, Wang CY. *J. Am. Chem. Soc.* 2012; 134: 9054-9057.
[13] Wu X, Scott K. *J. Power Sources* 2012; 214: 124-129.
[14] Xiao L, Zhang S, Pan J, Yang C, He M, Zhuang L, Lu J. *Energy Environ. Sci.* 2012; 5: 7869.
[15] Wu X, Scott K. *Int. J. Hydrogen Energy* 2013; 38: 3123-3129.
[16] Parrondo J, Arges CG, Niedzwiecki M, Anderson EB, Ayers KE, Ramani V. *RSC Adv.* 2014; 4: 9875.
[17] Pavel CC, Cecconi F, Emiliani C, Santiccioli S, Scaffidi A, Catanorchi S, Comotti M. *Angew. Chem. Int. Ed. Engl.* 2014; 53: 1378-1381.
[18] Wu X, Scott K, Xie F, Alford N. *J. Power Sources* 2014; 246: 225-231.
[19] Salvi P, Nelli P, Villa M, Kiros Y, Zangari G, Bruni G, Marini A, Milanese C. *Int. J. Hydrogen Energy* 2011; 36: 7816-7821.
[20] Hnát J, Paidar M, Schauer J, Žitka J, Bouzek K. *J. Appl. Electrochem.* 2012; 42: 545-554.
[21] Wu X, Scott K. J. *Power Sources* 2012; 206: 14-19.
[22] Aili D, Hansen MK, Renzaho RF, Li Q, Christensen E, Jensen JO, Bjerrum NJ. *J. Membr. Sci.* 2013; 447: 424-432.
[23] Ahn SH, Lee B-S, Choi I, Yoo SJ, Kim H-J, Cho E, Henkensmeier D, Nam SW, Kim S-K, Jang JH. *Appl. Catal. B* 2014; 154-155: 197-205.
[24] Sheng W, Myint M, Chen JG, Yan Y. *Energy Environ. Sci.* 2013; 6: 1509.
[25] Papadimitriou S, Tegou A, Pavlidou E, Armyanov S, Valova E, Kokkinidis G, Sotiropoulos S. *Electrochim. Acta* 2008; 53: 6559-6567.
[26] Oliva P, Leonardi J, Laurent JF. *J. Power Sources* 1982; 8: 229-255.
[27] Subbaraman R, Tripkovic D, Strmcnik D, Chang KC, Uchimura M, Paulikas AP, Stamenkovic V, Markovic NM. *Sci.* 2011; 334: 1256-1260.
[28] Subbaraman R, Tripkovic D, Chang KC, Strmcnik D, Paulikas AP, Hirunsit P, Chan M, Greeley J, Stamenkovic V, Markovic NM. *Nat. Mater.* 2012; 11: 550-557.
[29] Zhang D, Zeng K. *Ind. Eng. Chem. Prod. Res.* 2012; 51: 13825-13832.
[30] Arbabi F, Kalantarian A, Abouatallah R, Wang R, Wallace JS, Bazylak A. *J. Power Sources* 2014; 258: 142-149.

Multiplexed detection of epigenetic markers using quantum dot (QD)-encoded hydrogel microparticles

Analytical Chemistry
2016; 88: 4259–4268

Sang Yun YEOM, Choong Hyun SON, Byung Sun KIM, Sung Hyun TAG, Eun Joo NAM, Hyo Geun SHIN, So Hyun KIM, Hae Min GANG, Hyun Joo J. LEE, Jung Kyu CHOI, Heh In IM(him@kist.re.kr), Il Joo CHO(ijcho@kist.re.kr), and Nak Won CHOI(nakwon.choi@kist.re.kr)

Epigenetic alterations in gene expression are influenced by experiences and environment, resulting in significant variation of epigenetic markers from individual to individual. Therefore, it is imperative to measure various epigenetic markers simultaneously from samples of individual subjects to accurately analyze the epigenetic markers in biological samples. Moreover, the individualized genome-wide analysis has become a critical technology for recent trends in clinical applications such as early diagnosis and personalized medicine screening of numerous diseases. The array-based detection of modified histones, conventionally used for multiplexed analysis of epigenetic changes, requires pooling of samples from many subjects to analyze populationwise differences in the expression of histone markers and does not permit individualized analysis. Here, we report multiplexed detection of genome-wide changes in various histone modifications at a single-residue resolution using quantum dot (QD)-encoded polyethylene glycol diacrylate (PEGDA) hydrogel microparticles. To demonstrate the potential of our methodology, we present the simultaneous detection of (1) acetylation of lysine 9 of histone 3 (Ac−H3K9), (2) dimethylation of H3K9 (2Me-H3K9), and (3) trimethylation of H3K9 (3Me-H3K9) from three distinct regions in the brain [nucleus accumbens (NAc), dorsal striatum (DSt), and cerebellum (Cbl)] of cocaine-exposed mice. Our hydrogel-based epigenetic assay enabled relative quantification of the three histone variants from only 10 μL of each brain lysate (protein content = ~ 1 μg/μL) per mouse. We verified that the exposure to cocaine induced a significant increase of acetylation while a notable decrease in methylation in NAc.

Targeting prion-like protein doppel selectively suppresses tumor angiogenesis

The Journal of Clinical Investigation
2016; 126(4): 1251–1266

Taslim A. Al-HILAL, Seung Woo CHUNG, Jeong Uk CHOI, Farzana ALAM, Joo Ho PARK, Seong Who KIM, Sang Yoon KIM, Fakhrul AHSAN, In San KIM(iskim14@kist.re.kr), and Young Ro BYUN

Controlled and site-specific regulation of growth factor signaling remains a major challenge for current antiangiogenic therapies, as these antiangiogenic agents target normal vasculature as well tumor vasculature. In this article, we identified the prion-like protein doppel as a potential therapeutic target for tumor angiogenesis. We investigated the interactions between doppel and VEGFR2 and evaluated whether blocking the doppel/VEGFR2 axis suppresses the process of angiogenesis. We discovered that tumor endothelial cells (TECs), but not normal ECs, express doppel; tumors from patients and mouse xenografts expressed doppel in their vasculatures. Induced doppel overexpression in ECs enhanced vascularization, whereas doppel constitutively colocalized and complexed with VEGFR2 in TECs. Doppel inhibition depleted VEGFR2 from the cell membrane, subsequently inducing the internalization and degradation of VEGFR2 and thereby attenuating VEGFR2 signaling. We also synthesized an orally active glycosaminoglycan (LHbisD4) that specifically binds with doppel. We determined that LHbisD4 concentrates over the tumor site and that genetic loss of doppel in TECs decreases LHbisD4 binding and targeting both in vitro and in vivo. Moreover, LHbisD4 eliminated VEGFR2 from the cell membrane, prevented VEGF binding in TECs, and suppressed tumor growth. Together, our results demonstrate that blocking doppel can control VEGF signaling in TECs and selectively inhibit tumor angiogenesis.

Diffraction effects incorporated design of a parallax barrier for a high-density multi-view autostereoscopic 3D display

OPTICS EXPRESS
2016; Vol. 24, No. 4: 4057

Ki Hyuk YOON, Heong Kyu JU, Hyun Kyung KWON, In Kyu PARK, and Sung Kyu KIM(kkk@kist.re.kr)

We present optical characteristics of view image provided by a high-density multi-view autostereoscopic 3D display (HD-MVA3D) with a parallax barrier (PB). Diffraction effects that become of great importance in such a display system that uses a PB, are considered in a one-dimensional model of the 3D display, in which the numerical simulation of light from the display panel pixels through PB slits to viewing zone is performed. The simulation results are then compared to the corresponding experimental measurements with discussion. We demonstrate that, as a main parameter for view image quality evaluation, the Fresnel number can be used to determine the PB slit aperture for the best performance of the display system.

It is revealed that a set of the display parameters, which gives the Fresnel number of ~ 0.7, offers maximized brightness of the view images while that corresponding to the Fresnel number of 0.4 ~ 0.5 offers minimized image crosstalk. The compromise between the brightness and crosstalk enables optimization of the relative magnitude of the brightness to the crosstalk and leads to the choice of display parameter set for the HD-MVA3D with a PB, which satisfies the condition where the Fresnel number lies between 0.4 and 0.7.

Effects of the functionalized graphene oxide on the oxygen barrier and mechanical properties of layer-by-layer assembled films

Composites Part B
2016; 92: 307–314

Seon Guk KIM, Nam Ho YOU, Won Ki LEE, Jun Yeon HWANG, Myung Jong KIM, David HUI, Bon Cheol KU(cnt@kist.re.kr), Joong Hee LEE

An effective method to fabricate high-performance oxygen gas barrier films by alternately stacking negatively charged graphene oxide (GO) and positively charged aminno-ethyl-functionalized GO (AEGO) on PET substrates was suggested. The GO was prepared by the Hummer's method using natural graphite powder and the AEGO was synthesized by a carbodiimide reaction of the GO. High resolution transmission electron microscopy (HRTEM) and X-ray photoelectron spectroscopy (XPS) were used to characterize the introduction of functional groups of GO and AEGO. GO/AEGO/GO layers on a PET film were formed through spray coating method. The gas barrier and mechanical properties of the film were examined. One layer of GO/AEGO/GO stacked film coated on a PET substrate showed an oxygen permeability of 0.01 cc/m2 day atm, which is 103 times lower than that of pure PET. The results corresponding to tensile strength and modulus of the film revealed an increase of approximately 61 and 41% compared to those of pure PET, respectively.

Novel electrostatic precipitator using unipolar soft X-ray charger forremoving fine particles: application to a dry de-NOXprocess

Journal of Hazardous Materials
2016; 303: 48–54

Jeong An CHOI, Hak Joon KIM, Yong Jin KIM, Sang Soo KIM, Jae Hee JUNG(jaehee@kist.re.kr)

The novel electrostatic precipitator (ESP), consisting of a soft X-ray charger and a collection part, was demonstrated and applied to a dry de-NOXprocess to evaluate its performance in by-product particle removal. NOXgas was oxidized by ozone (O3) and neutralized by ammonia (NH3) sequentially, and finally converted to an ammonium nitrate (NH4NO3) aerosol with ~100-nm peak particle diameter. The unipolarsoft X-ray charger was introduced for charging the by-product particles in this dry de-NOXprocess. For the highest particle collection efficiency, the optimal operating conditions of the soft X-ray charger and collection part were investigated by adjusting the applied voltage of each device. The results showed that ~99% of NOXwas removed when the O3/NOX ratio was increased to 2 (i.e., the maximum production conditions of the NH4NO3 by-product particles by the gas-to-particle conversion process). The highest removal efficiency of particle (~90%) was observed with operating conditions of positive polarity and an applied voltage of ~2–3 kV in the charger chamber. The unipolar soft X-ray charger has potential for particle removal systems in industrial settings because of its compact size, ease of operation, and non-interruptive charging mechanism.

Evaluating integrated strategies for robust treatment of high saline piggery wastewater

Water Research
2016; 89: 222–231

Hyun Chul KIM, Wook Jin CHOI, A Na CHAE, Joon Hong PARK, Hyung Joo KIM, Kyung Guen SONG(kgsong@kist.re.kr)

In this study, we integrated physicochemical and biological strategies for the robust treatment of piggery effluent in which high levels of organic constituents, inorganic nutrients, color, and salts remained. Piggery effluent that was stabilized in an anaerobic digester was sequentially coagulated, micro-filtered, and air-stripped prior to biological treatment with mixotrophic algal species that showed tolerance to high salinity (up to 4.8% as Cl^-). The algae treatment was conducted with continuous O_2 supplementation instead of using the combination of high lighting and CO_2 injection. The microalga Scenedesmus quadricauda employed as a bio-agent was capable of assimilating both nitrogen (222 mg N g cell^{-1} d^{-1}) and phosphorus (9.3 mg P g cell^{-1} d^{-1}) and utilizing dissolved organics (2053 mg COD g cell^{-1} d^{-1}) as a carbon source in a single treatment process under the heterotrophic growth conditions. The heterotrophic growth of S. quadricauda proceeded rapidly by directly incorporating organic substrate in the oxidative assimilation process, which coincided with the high productivity of algal biomass, accounting for 2.4 g cell L^{-1} d^{-1}. The algae-treated wastewater was subsequently ozonated to comply with discharge permits that limit color in the effluent, which also resulted in improved biodegradability of residual organics. The integrated treatment scheme proposed in this study also achieved 89% removal of COD, 88% removal of TN, and 60% removal of TP. The advantage of using the hybrid configuration suggests that this would be a promising strategy in full-scale treatment facilities for piggery effluent.

Head mounted display apparatus and contents display method

US 9250443 (2016-02-02) KR 1609183 (2016-03-30)

Ji Hyung PARK / jhpark@kist.re.kr

Disclosed are a head-mounted display apparatus and a contents display method. The head-mounted display apparatus includes: a mobile device tracing information processing unit for receiving position information or orientation information of a mobile device and generating tracing information of the mobile device based on the received position information or orientation information of the mobile device; a gesture processing unit for receiving input information of the mobile device and generating gesture information to change an output format of contents by using the received input information; a rendering unit for generating a predetermined virtually augmented contents image based on the tracing information of the mobile device and the gesture information; and a display unit for displaying the generated virtually augmented contents image.

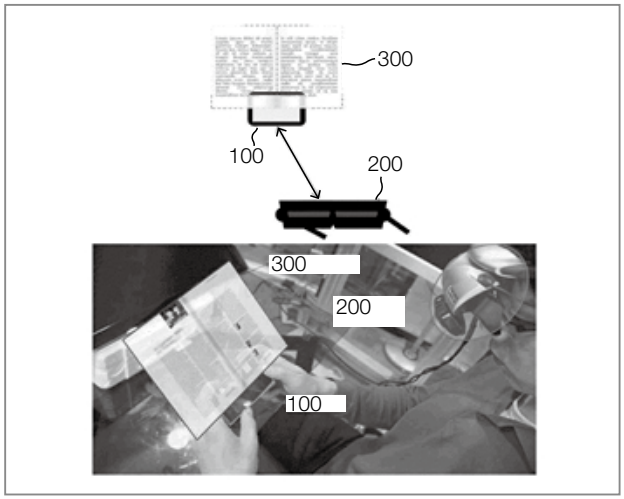

Fiber-optic surface plasmon resonance sensor and sensing method using the same

US 9285534 (2016-03-15) KR 1613091 (2016-04-11)

Kyeong Seok LEE / kslee21@kist.re.kr

A fiber-optic surface plasmon resonance sensor may include an optical fiber and a surface plasmon excitation layer. The optical fiber may include a core, a cladding surrounding the core, and a depression. The surface plasmon excitation layer may include a first excitation layer, a second excitation layer and an optical waveguide layer between the first excitation layer and the second excitation layer. Incident light incident through the core may be coupled to the surface plasmon excitation layer at a specific angle of incidence and wavelength satisfying the surface plasmon resonance condition. Depending on the polarizing direction of the incident light, an s-polarized component may be coupled to the guided-wave mode in the optical waveguide layer constituting the surface plasmon excitation layer.

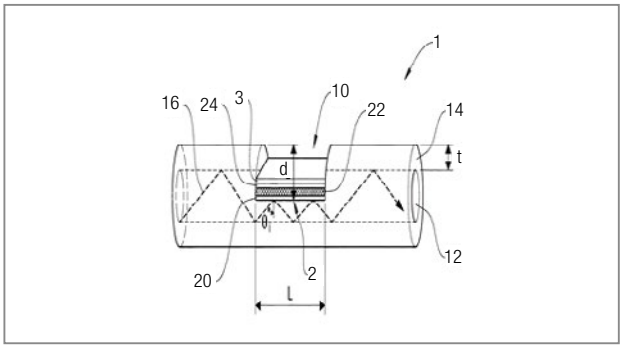

Apparatus and method for generating wave functional pulsatile microflows by applying Fourier cosine series and hydraulic head difference

US 9291172 (2016-03-22) KR 1614019 (2016-04-14)
Myung Suk CHUN / mschun@kist.re.kr

An apparatus for generating pulsatile flows includes a liquid vessel capable of containing a liquid, a plurality of revolving mechanisms associated with each other, and a microchannel supplied with a liquid from the liquid vessel. As the plurality of revolving mechanisms rotate, a periodically changing pressure difference occurs between the liquid vessel and the microchannel, thereby implementing a pulsatile flow having a wave functional form in the microchannel. By applying the hydraulic head difference and controlling revolution of the revolving mechanisms based on Fourier cosine series, a minute and precise pulsatile flow of a wave functional form may be implemented by means of simple configuration and fabrication, which may not easily obtained by a conventional pump.

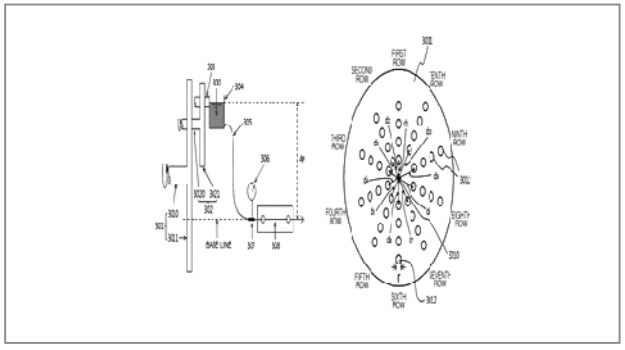

Biocompatible pressure sensor and manufacturing method thereof

US 9341530 (2016-05-17) KR 1308104 (2013-09-06)
Soo Hyun LEE / shleekist@kist.re.kr

Provided are a biocompatible pressure sensor which can be implanted into a body to wirelessly measure an internal pressure of the body outside the body, and a method of manufacturing the biocompatible pressure sensor. The biocompatible pressure sensor includes a coil inductor, a capacitor electrically connected with the coil inductor to constitute an LC resonant circuit together with the coil inductor, a flexible membrane disposed while being spaced apart from the coil inductor with an internal space interposed therebetween and surrounded by a housing, and a pressure displacement member fixed to one surface of the flexible membrane facing the coil inductor. The flexible membrane is transformed by external pressure to change a distance between the coil inductor and the pressure displacement member.

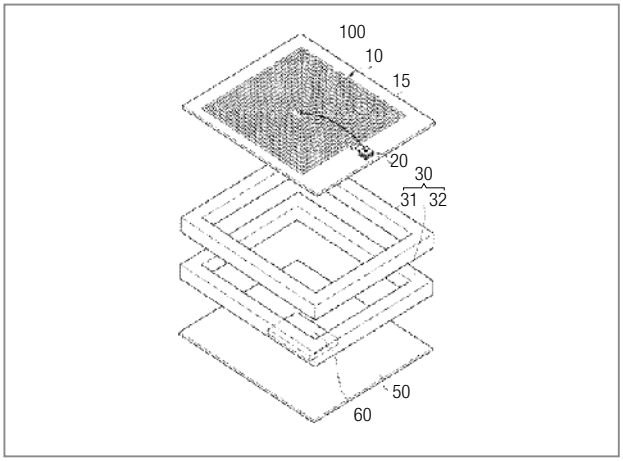

Apparatus and method for detecting backlash and slip

US 9329144 (2016-05-03) KR 1312276 (2013-09-16)

Man Ho KIM / man-hokim@kist.re.kr

The detecting apparatus comprises: a monochromator, for Bragg-diffracting the incident beam; an analyzer, on which the beam diffracted by the monochromator is incident, an analyzer Bragg-diffracting the incident beam; a controller, for controlling the driver connected to the monochromator and the analyzer, so as to rotate the analyzer or the monochromator in a first direction and in a second direction opposite to the first direction; and a detector, for detecting the beam diffracted by the analyzer or transmitted through the analyzer while the analyzer or the monochromator is rotating and measuring a backlash and/or a slip of the driver by using the detected beam. The backlash detecting apparatus can measure a backlash and/or a slip in the unit of sub-arcsecond or sub-nanometer by using the radiation beam such as a neutron beam, an X-ray beam or the like.

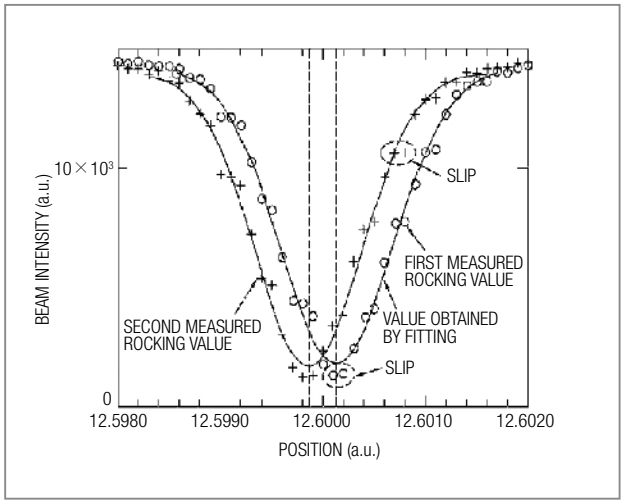

Oil-free turbocharger assembly

US 9322294 (2016-04-26) KR 1614880 (2016-04-18)

Yong Bok LEE / lyb@kist.re.kr

The present invention relates to an oil-free turbocharger assembly using an airfoil bearing that may be useful in high speed conditions. The assembly can be cooled easily. A heat-proof coating can also be easily applied to the turbo charger's rotating shaft. In one embodiment, an oil-free turbocharger assembly has a constant distance between a journal portion and a rotating shaft so that the mass of the rotating body can be minimized and the rotating body assembly can have a small moment of inertia. The turbocharger in some embodiments of the invention may be cooled by a refrigerant which improves cooling efficiency. Each part of the rotating body assembly in some embodiments may be individually treated with a heat-proof process so that productivity can be improved.

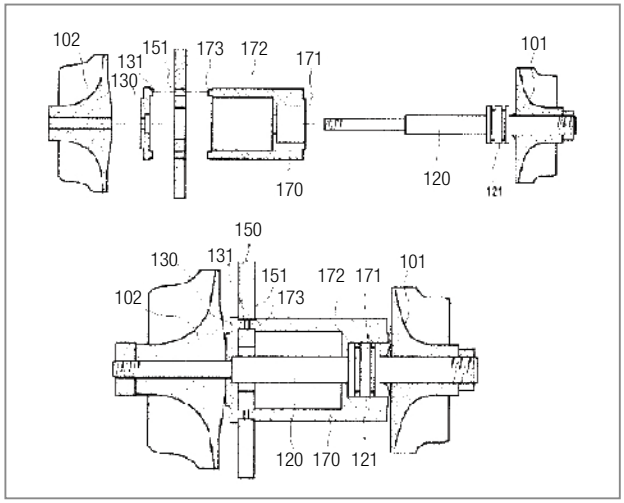

1. Dr. C. Justin LEE Wins Kyung Ahm Arts and Academy Prize for 2016

November 4, 2016

The Kyung Ahm Education & Culture Foundation first began handing out awards in 2004 as a way of supporting scholars and artists by giving them the recognition they deserve. It is a public utility foundation originally established by Geum Jo SONG, president of the Taeyang Corporation. One of this year's recipients is Dr. C. Justin LEE, a widely-recognized brain specialist who has been working at KIST since 2004.

Dr. Lee graduated from the University of Chicago and received his doctorate from Columbia University. His winning of the prize resulted from studies done on signal transmission mechanisms and other newly discovered functions of glia cells (non-neuronal cells). His work has provided great insight into various aspects of cerebropathia, especially as it relates to dementia and memory loss. Dr. Lee's contributions have subsequently been used as a benchmark by brain scientists working to develop a new drug for combating cerebropathia.

Furthermore, in his role as scientific researcher and head of KIST's Laboratory for Glia-Neuron Interaction, he helped develop a new 3D brain imaging technique in collaboration with the KIST Brain Science Institute. This technique has led to joint research projects with Yale, Duke and Oxford Universities, as well as MIT.

Other examples of Dr. Lee's studies can be found in leading journals such as *Nature* and *Cell* where they are having a great impact on the brain science field. For example, Dr. Lee's discovery that caffeine suppresses cancer cell propagation has altered people's attitudes toward caffeine by causing them to regard it as a possible ally in the fight against brain cancer.

2. KIST's Brain Science Institute Participates in the BRAIN Initiative of the NIH

September 26, 2016

On September 26th, KIST announced that Drs. Bradley Baker and Lawrence Cohen of the Center for Functional Connectomics at KIST's Brain Science Institute had been named as researchers for the Brain Research through Advancing Innovative Neurotechnologies® (BRAIN) Initiative managed and supported by the U.S.'s National Institutes of Health.

Drs. Baker and Cohen have successfully developed fluorescent protein sensors that use light to measure brain activity for the purpose of mapping human brain functions. These sensors, developed at KIST, reflect their Korean origins in their names: Bongwoori (mountaintop) and Pado (wave), which describe their functional characteristics.

In addition to the KIST-based scientists, research teams from Yale University and Montana State University will collaborate in the project Optimization of Transformative Technologies for Large Scale Recording and Modulation in the Nervous System (U01). This joint project will be conducted over a 3-year period with funding of 3 million USD.

This initiative corresponds well with the Korean government's recently announced strategy to develop the country's expertise in brain science. The government policy aims to secure core brain technologies, including the mapping of the brain, and comes at a time when other

advanced nations, such as the U.S., many EU countries and Japan are carrying out large-scale national brain research projects.

KIST's president, Dr. Byung Gwon LEE, highlighted the importance of the intiative by stating, "KIST's participation in the BRAIN Initiative is significant in that Korea's brain research capability has now become globally recognized. This project will enhance the status and visibility of domestic brain researchers and encourage more Korean participation in international research programs by expanding exchanges with foreign organizations."

3. SNU Professor Uh Taek OH Named Director of KIST Brain Science Institute

September 26, 2016

The appointment of Professor Uh Taek OH as the next director of the KIST Brain Science Institute was announced on September 26th. Dr. Oh is a faculty member at the College of Pharmacy at Seoul National University and will succeed the Brain Science Institute's current director, Dennis W. CHOI, when his term expires at the end of 2016.

Dr. Oh obtained a doctorate at the University of Oklahoma's medical school and completed a post-doctoral program at the University of Texas. He is a world-renowned authority in neuroscience and was presented the Korea Premium Science and Technology Award in 2010. Recently, he identified the Tentonin 3 gene that detects changes in muscle length, a finding that could potentially lead to important new discoveries. In addition, he has served as chairman of the Brain Research Promotion Framework Execution Committee as well as the Korean Society for Brain and Neural Science. He is currently the chairman of the board of directors at the Korea Pasteur Institute and chairman of the Korean Brain Society.

In line with the government's national strategy for brain science development, KIST is actively working to enhance expertise in brain research. Professor Oh's appointment is part of this effort. In his role as chairman of the KIST Brain Science Institute Advisory Committee, he is already familiar with the institute's researchers and their projects. Furthermore, his own in-depth research is expected to contribute to the convergence brain research that KIST is actively promoting.

In the words of KIST's president, Dr. Byung Gwon LEE, "To strengthen KIST's role as a platform for opening and convergence, we invited Professor Oh to be the next director of the KIST Brain Science Institute. The Brain Science Institute, which has been leading the domestic brain research field since early 2000, will be in capable hands under Professor Oh's leadership."

The new director's term in office begins January 1, 2017. The current director, Dennis Choi, will stay on as an advisor.

4. Dr. Ik Chan KWON and Dr. Kwang Myeong KIM Again Named Among the World's Most Influential Scientific Minds

September 21, 2016

On September 21st, KIST announced that Director Ik Chan KWON of the Biomedical Research Institute and Dr. Kwang Myeong KIM had been named by the Thomson

Reuters news organization among the world's most influential scientific minds. This is the third year in a row Drs. Kwon and Kim have received this recognition.

Thomson Reuters analyzed 128,887 research papers from the Web of Science database in 21 different fields published between 2004 and 2014 to determine 3,200 most highly cited researchers. Only those researchers whose achievements are recognized as among the world's top 1% are named highly cited researchers. Drs. Kwon and Kim received their distinctions in the field of pharmacology and toxicology. Out of 26 domestic researchers listed in 2016, only 13 have been named for three years running, and from among those 13, only Dr. Kwon and Dr. Kim come from national research institutes. The researchers appearing on the Thomson Reuters list are recognized as possible candidates for the Nobel Prize.

5. New Green Technology Developed for Low-Cost Recycling of Carbon Fiber

August 23, 2016

Dr. Moon Ju Ko's team at KIST Jeonbuk (Institute of Advanced Composite Materials) has developed a new technology for using water to recycle carbon fiber, a high-priced material, from carbon fiber reinforced plastics (CFRP). A technology transfer presentation for carbon fiber-related companies was held on August 25th at KIST Jeonbuk.

CFRP is a carbon fiber-based compound material that is 25% lighter and 10 times stronger than steel. It is widely used in various industries such as the aerospace, automotive, ship-building and sports equipment industries. The global CFRP market is expected to reach 21 trillion KRW in 2015 and 42 trillion KRW in 2020. However, CFRP is expensive to produce, and few technologies are available to dispose of or recycle the material without negative environmental consequences.

The CFRP recycling technology developed by the KIST team is a chemical method using water as a solvent with a low-cost additive. It is an innovative technology that requires little energy use. If the compound material is recycled using this technology, more than 95% of the carbon fiber is recovered, while its material property is maintained. This is a highly advantageous, green, and economically viable technology.

Applying this recycling technology to the domestic market, KIST manufactured and operated a pilot plant that was designed to recycle one ton of CFRP per year. The plant successfully demonstrated its potential for mass production and economic feasibility. It represents the lowest-costing CFRP recycling technology in the world

Dr. Ko explained the advantage of the KIST-developed technology by saying, "I decided to explore an innovative way to recycle carbon fiber. Our method is economic and environmentally friendly. It can be applied to the industry promptly. Eventually, our team plans to export this technology overseas where the compound material-trading market is big, such as in China, the U.S. and Europe."

KIST plans to transfer the technology to any domestic company that wants to commercialize it.

Pilot plant

6. Six KIST R&D Projects Land in Top 100 List

July 14, 2016

Six research projects carried out by KIST were named among 2016's "Top 100 National R&D Results," as compiled by the Ministry of Science, ICT and Future Planning—more projects than from any other Korean university or research institute, even ones that are state-funded.

The R&D fields covered by the six projects were: convergence technology (2 projects), information technology (1 project), clean energy (2 projects) and electronics (1 project). The corresponding research topics were as follows:

• Technology to Predict Intended Behaviors Using Bio Signals

• Long-term Clinical Study and Multiscale Analysis of In Vivo Biodegradation Mechanism of Mg Alloy

• Development of the Next Generation SPIN Electronic Device without Signal Loss

• Development of Structural Catalyst for Sloshing GTL, Multi-concentric MTFBR and GTL-FPSO Process for Manufacturing Clean Fuel

• Development of Material Technology for the Secondary Battery which Shows High Performance by Mitigating Stress from the Shape Change by the Electrode Material

• Development of Smart Bearing and Sealing Technology Which Allows Driving in Severe Circumstances

Since 2006, the Ministry of Science, ICT and Future Planning has selected its Top 100 projects as a way of boosting morale among S&T researchers as well as promoting outstanding national R&D achievements.

Developing a 3D Montage System

The earliest attempts to develop a 3D montage system date back six years when the limitations of conventional 2D montage systems prompted the National Police Agency to push for more modern montage technologies. As a result, the Ministry of Knowledge Economy determined that the development of a 3D montage system should be a national R&D project. KIST took on the responsibility for developing this system, and research began in earnest in June 2011. The core R&D activities were conducted over three years, out of which a more sophisticated and effective montage system emerged.

The term montage refers to the photographic image of a face, produced by composing data on facial features (eye, nose, mouth, etc.) based on descriptions provided by a crime victim or witness who has seen a suspect. The first montages were drawn as sketches, similar to a rough portrait. After that, a method for projecting a composite photograph on a screen was sometimes used. In 1996, the Korean National Police Agency adopted the system of a U.S.-based company, INFOTECH, which used computers to draw montages for the first time. It was difficult, however, to accurately draw Korean faces with this system, and so in 1999, a montage system specific to Korea was developed and adopted. Since then, numerous corrections have been made to the Korean system, but technological changes have occurred so rapidly over the past ten years that even this modified montage system is now outdated.

The montage of a suspect's face is based on a witness's statement, which may be the only clue in a crime scene, but inaccuracies can occur for a variety of reasons. For example, the witness may not be objective or may not have been able to see a face clearly if the suspect was wearing a hat or mask or lighting conditions were poor. With a conventional 2D montage system, it is only possible to describe the front side of the face. Other shortcomings include an inability to simulate the same lighting conditions that existed at the crime scene or accurately fill in the parts of a scene which a witness can't remember clearly. It is important to consider that more CCTVs are in use today and often provide the most important clues in crime investigations, but there are still a vast number of crimes that occur in dead angle areas out of the range of CCTVs, as well as indoors, so the demand for preparing montages remains high.

Once the development of a more modern montage system became a national R&D project, research began at KIST under the leadership of Professor Ik Jae KIM. Professor Kim tried to understand the complexities of crime scenes by frequently visiting the science investigation center of the National Police Agency. At first, cooperation with the National Police Agency was impeded by a lack of trust and certain barriers imposed by the privacy protection act that had taken effect in September 2011. Construction of the database necessary for drawing a montage became extremely difficult, delaying the development process. However, as the work proceeded and it became clear that this project would be unlike projects of the past and would correct existing problems, a relationship of trust was gradually established with the police department. This provided the opportunity to take a more proactive and effective approach to the problems of the field. [Photograph 1]

By adopting and developing graphics technologies such as image processing, 3D modeling, rendering and simulation technologies, it was possible to overcome the limitations of the existing montage system. Of particular importance was a holistic

Photograph 1. Professional Montage Agents Seminar held at KIST. September 5, 2013

composite method that could sharpen a witness's memory by helping to stimulate a holistic impression of the suspect so that a montage could be made even when the witness had an unclear memory of the suspect. This method is based on research which shows that people tend to remember an overall impression of a person more than individual characteristics of the face. This is in contrast to the existing montage system which composes a face by combining specific facial features like the eyes, nose, and mouth. The newly developed montage system applies an interactive evolutional computing method in which generic faces representing various facial forms are provided to the witness who can then select the ones which best match his/her overall impression of the suspect's face. As the system performs iterations through various stages, the montage gradually resembles a specific face built upon the many impressions remembered by the witness.

A new technology being designed for the montage system is still in its early development stages, but has the potential to bring significant benefits to investigative police work. With this advance, it will soon be possible to compare a montage against photographs in the criminal database to more easily identify the faces of suspects.

Another aspect of montage technology with significant potential relates to advanced age recognition technology. Researchers began by gathering considerable information about the aging process from photos and montages. By comparing and analyzing this information, it was possible to apply a method for extracting specific age features and incorporating them within the existing age recognition algorithm to to develop a more accurate, age-appropriate montage. This

Photograph 2. (Left image) A poster advertising a special photographic exhibit entitled "Last Wish" commemorating the 70th anniversary of independence. The exhibit opened August 15, 2016. (Right image) Dr. Ik Jae KIM, researcher in charge of KIST's project to modernize montage technology.

Photograph 3. An example of age conversion technology prepared for "Last Wish," a special photographic exhibition of separated families in commemoration of the 70th anniversary of independence. August 15, 2016

age recognition technology was designed to verify whether or not the age information obtained through a witness is well reflected in the montage. The ability to manipulate the age of a suspect in a montage is highly desirable for crimes that have remained unsolved for a long period of time. It can also be helpful in the search for missing children by predicting their appearance after many years. The National Center for Missing & Exploited Children in the United States ((NCMEC)/missingkids.com) has an age progression program that generates the images of what missing children would look like currently, many years after their disappearance. This imaging system has contributed significantly to the success rate in finding these children. This program generates the face of the missing child at a certain age, converted by Photoshop, using photographs of the child, the child's parents, sisters, brothers and other relatives. However, since this program is not automated and must be operated by a trained expert, results may differ widely, depending on the personal experience and training of the technician. This system has an additional drawback in the context of the Korean experience because it depends on a database built primarily on Americans. As a result, there was a clear need to develop an automated age conversion system better suited to Koreans while developing an overall 3D montage system.

Photograph 4. The age conversion montage technology selected and exhibited as one of the top ten technologies developed at government-invested institutions. January 28, 2016

Although not all its upgrades are yet in place, the montage system developed at KIST is being applied by the National Police Agency nationwide to arrest criminal suspects. Interestingly, however, the system has performed even more effectively as a means of predicting the current appearance of missing persons. As a case in point, in early 2015, Cheil Worldwide Inc. contacted KIST to ask for help in giving a meaningful gift to separated families in commemoration of the 70th anniversary of the liberation of Korea. Such a request was unexpected and not part of the original vision behind the development of the montage system; the request also came at a time when the montage researchers were very busy with other tasks. However, KIST decided to provide technical support to the commemoration project in hopes that the technology would help an important cause. The Korean National Red Cross collected photographs from separated families and selected 23 of those families for participation in the project. The data was then delivered to KIST where the age conversion technology developed as part of the montage system was used to generate images of family members as they would appear after 70 years. The special commemoration event, held in the Chosun Exhibition Hall on August 15, 2015, was a success, and the words of gratitude expressed by the families for the opportunity to reunite with their relatives, albeit by photographs, made Dr. Kim's team realize that their work meant a great deal---a truly satisfying reward for their intense research efforts.

The National Research Council of Science & Technology Development honored the 3D montage system by selecting it as one of the top ten technologies created at government-invested institutions. The selected technologies were exhibited to the public, and the age conversion technology was considered one of the most interesting technologies honored that year. [Photograph 4]

The new montage system was officially adopted by the National Police Agency in December 2015. It is now operating at the main office of the agency, as well as its offices in Seoul, Gyeonggi, and Busan. In the spring of 2015, officers in charge of montages throughout the country were trained in the new system, and soon after, the mother of a child who had been missing for 38 years requested that she be able to see the face of her son one last time before her death. An officer responsible for montages at the National Police Agency used the KIST montage system to generate an image representing the current

face of the missing child based on photographs from 38 years ago. The image was made public, and miraculously, the missing child---now grown---was located. [Photograph 6]

Every year about twenty thousand people are reported missing in Korea. Of those that are children, many return home, but a significant number remain missing. On May 25th, this year's Day of Missing Children, a special event was held where photographs of the faces of the missing children as they would appear today, prepared using the National Center for Missing Children's KIST-developed montage age conversion technology, were delivered to the families of those children. [Photograph 5]

In addition to missing children, there are many unsolved cases involving criminal suspects. Many of the long term cases become the subjects of TV news documentary programs for which KIST provides montage-related technical support when requested. An example of this assistance related to a program on the Hwaseong Serial Murder case which has remained unsolved for 30 years. KIST predicted the likely current appearance of the suspect by applying its age conversion technology to the initial montage of the suspect. It is hoped that making the image public will lead to a breakthrough in the case. [Photograph 7]

More requests are expected to come from the National Police Agency and broadcasting stations regarding missing children and unsolved cases. Often when providing support for such requests, however, limits in the current technology become clear. Whenever such

Photograph 5. The National Police Agency distributing a predicted current montage of a missing child at the 10th Day of Missing Children ceremony.

Photograph 6. Broadcasted scenes from a family reunion after a child missing for 38 years was located thanks to montage technology. June 21, 2016

Photograph 7. Broadcasted scene from the documentary of the Hwaseong Serial Murderer case that occurred 30 years ago. JTBC, MBC, September 5, 2016

situations arise, the KIST team strives to improve the technology so that some degree of assistance can be provided. They continue to study methods to increase the precision of age conversion technology and are planning to develop a technology in association with the montage system that can clarify the face of a criminal suspect so that identification is possible even with a CCTV image of poor quality. A particular challenge relates to capturing changes to facial appearance that occur over time; sometimes results are not precise enough when a simple image is based on statistical characteristics alone. The KIST team is currently developing a technology that could make a more precise age conversion by reflecting external environmental conditions as well as genetic effects. These improvements would allow for more precise imaging, which we hope will resolve more unsolved cases and return more children to their loving families.

Interview

Dr. Ik Chan KWON

Director of the Biomedical Engineering Research Center, included among the world's top 1% of researchers for three consecutive years.

"It is not easy to pioneer a new area of science. Sometimes things do not go as planned. However, since new ideas are generated by accepting new challenges and having lively discussions, nothing is impossible. We will continue to develop good ideas and share them with other researchers."

This past October we met with Ik Chan KWON, head of the Medical Engineering Research Center, for a discussion of his work at KIST that has earned him a place in the top 1% of the world's researchers for the third year running. Analyzing information from the Web of Science database, Thompson Reuters named him to the select group of 3,200 researchers whose work is most cited on a global scale. These researchers are all considered potential candidates for the Nobel Prize. Another KIST scientist, Professor Gwang Myeong KIM, was also included on this list for a third year in a row.

Dr. Kwon noted that his selection by Thompson Reuters was the result of his work in theragnosis (therapy + diagnosis), a field which was first established in 2006. Theragnosis is a medical technology that allows doctors to conduct early diagnosis of diseases while also administering the appropriate treatment. This technology allows one to see with the naked eye the effects of medicine on a particular patient and whether

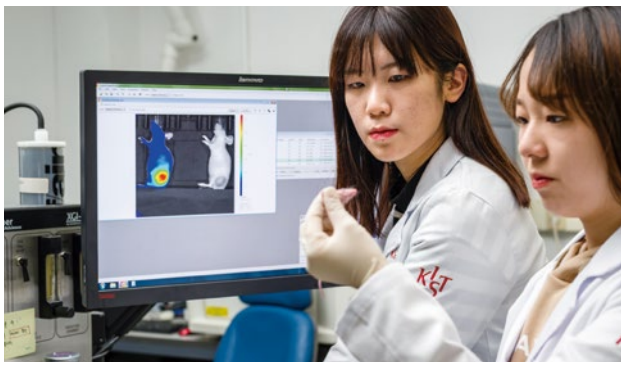

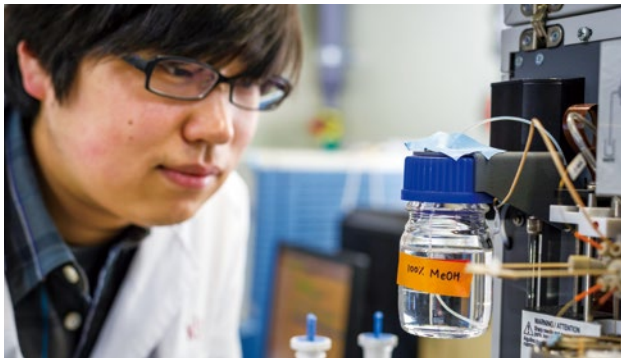

or not the treatment is proceeding well, thus enabling the simultaneous diagnosis and customized treatment of diseases like cancer and rheumatics. Dr. Kwon launched the Theragnosis Research Group in 2009 to conduct proactive research in the field, and since then, the scale of his research has dramatically increased.

The mission of KIST's Medical Engineering Research Center is to find ways to help humans live long, healthy lives. The Bionics Research Group, Biomaterial Research Group, and Theragnosis Research Center are all distinct groups within the Medical Engineering Research Center whose overall mission is to develop mental and physical rehabilitation techniques to improve the quality of life for the elderly and the disabled. The center also works to develop devices that could replace human tissues and organs, functional material, and high-tech medical techniques for simultaneous disease diagnosis and treatment.

Dr. Kwon started studying theragnosis in 2003 after coming across molecular imaging, a technique for imaging biological processes in the human body. At the time, he had been searching for ways to selectively treat specific cells, since drugs used in chemotherapy often kill normal cells in addition to cancerous ones, resulting in adverse side effects. Although KIST's Biomedical Engineering Research Center was already considering research into discovering a new kind of food source, a decision was made to devote resources to study molecular imaging instead, and Dr. Kwon was given the leading role.

In 2006, Dr. Kwon produced his first important paper in the field of molecular imaging—a field that Korea entered 10 years later than the U.S. As he explained, "After conducting some research, we created the concept of combining treatment application with molecular imaging. No other group in the world had tried combining the two."

He added, "If we could use video imaging to determine which parts of the body needed treatment, we could then effectively target that exact area. X-rays could

highlight the spread of cancer in a certain area, but with theragnosis we could administer treatment and see in real time what kind of medicine is more effective and how much the cancer is being reduced."

"Good research results require a certain amount of luck. Even with good results, the research can die out if the time is not right. Just because I pioneered theragnosis doesn't mean I will always be the leader in this field. I always keep in mind that brilliant new ideas can result from constructive discussions."

Last year, Dr. Kwon used a specific protein to develop a cancer-fighting drug with significantly reduced toxicity. This was done via joint research with a team led by Professor Sang Yoon KIM of Ulsan Medical University and Seoul Asan Hospital. According to Dr. Kwon, "Once this drug is injected and radiation applied, we can destroy cancer cells without destroying normal cells and causing negative side effects."

In the past, the fields of molecular imaging and nano-medicine were divided, but nowadays there are no boundaries among the various areas of medicine. According to Dr. Kwon, "It is not easy to pioneer a new area of science. Sometimes things do not go as planned. However, since new ideas are generated by accepting new challenges and having lively discussions, nothing is impossible. We will continue to develop good ideas and share them with other researchers."

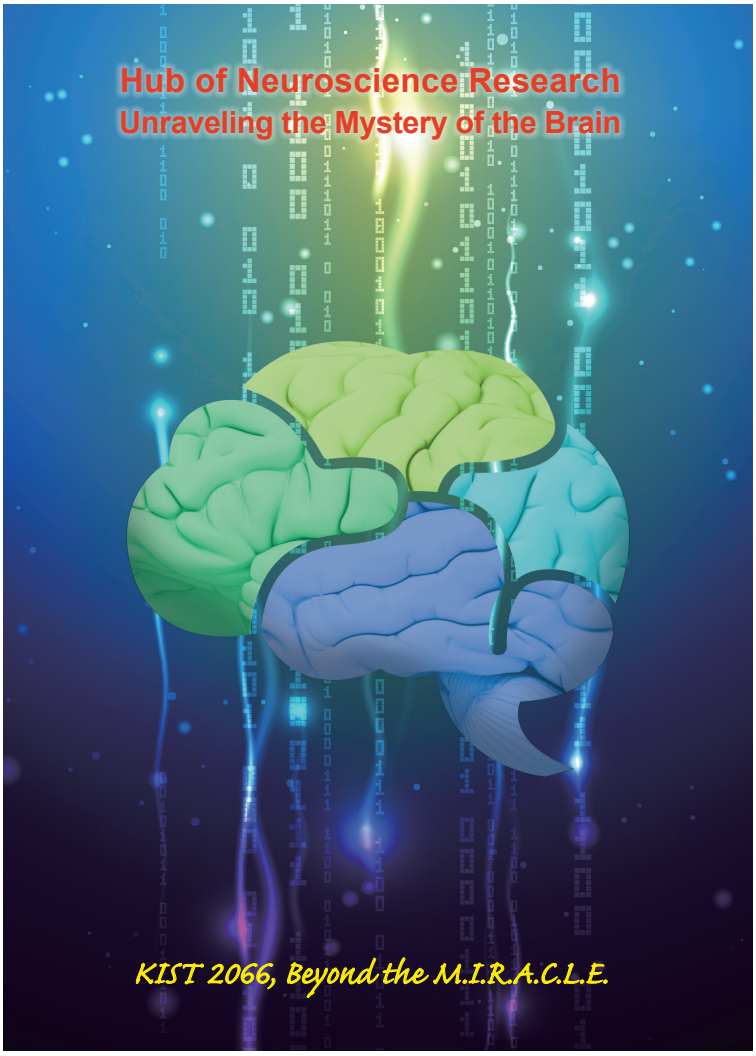

Cover image :

Hub of neuroscience research unraveling the mystery of the brain

The human brain is a highly complex system often dubbed a miniature universe.
Its many mysteries have yet to be unveiled. The Brain Science Institute specializes in convergence research that includes neuroscience, nanoengineering, medicine, and genetics through which it aims to understand the neural mechanism responsible for controlling human behavior and to discover clues to overcoming brain dysfunctions. The goal of the Brain Science Institute is to unravel the mysteries of the brain and ultimately becoming the hub of the world's brain science research.

Editorial Information

Editor-in-Chief
Tae Hoon LIM

Editorial Board Members
Il Joo CHO
Bradley BAKER
Hyun Kwang SEOK
Joon yeon CHANG
Jong Ho LEE
Seok Won HONG
Young Soon UM
Eui Seong KIM
Gi Hong YEUM

Managing Editor
Jin Soo KIM
jinsoojs.kim@kist.re.kr
+82-2-958-6155
Web Address
www.kist.re.kr/en

English Advisory Services
Anne Charlton
The Final Word Editing Services
the_final_word@live.com

Korea Institute of Science and Technology

5 Hwarang-ro 14–gil Seongbuk-gu Seoul 02792
Republic of Korea
Tel +82–2–958–6039 www.kist.re.kr/en
E–mail sarachang@kist.re.kr

NATIONAL AGENDA RESEARCH DIVISION

Solution Provider to National/Global Agenda

The National Agenda Research Division is established to provide solutions to national/global agenda by developing core competencies in the areas of renewable energy, carbon cycle and convergence of systems. These core competencies are believed to play a critical role not only to expedite the adaption to the new energy and environmental paradigm but also to create green industry. The division consists of four research centers: Fuel Cell Research Center, Clean Energy Research Center, Sensor System Research Center, and Photoelectronic Hybrid Research Center.

KIST
Korea Institute of Science and Technology